UNIVERSITY OF OKLAHOMA

GRADUATE COLLEGE

THE EFFECTS OF TERRAIN ON AN IDEALIZED TORNADO USING A

LARGE-EDDY SIMULATION

A THESIS

SUBMITTED TO THE GRADUATE FACULTY

in partial fulfillment of the requirements for the

Degree of

MASTER OF SCIENCE IN METEOROLOGY

By

MARTIN SATRIO
Norman, Oklahoma
2019

THE EFFECTS OF TERRAIN ON AN IDEALIZED TORNADO USING A
LARGE-EDDY SIMULATION

A THESIS APPROVED FOR THE
SCHOOL OF METEOROLOGY

BY

Dr. Robert Palmer, Chair

Dr. David Bodine, Co-Chair

Dr. Anthony Reinhart, Co-Chair

Dr. Alan Shapiro

Dr. Scott Salesky

Acknowledgments

Firstly, I would like to thank both of my advisors, Dr. David Bodine and Dr. Anthony Reinhart, for giving me support and mentoring throughout the entire Master's project. Ever since I was a little kid, I have dreamed of one day becoming a tornado researcher and I am forever grateful for the opportunity to pursue this dream. Not only have they kept me focused and motivated me, but through the research I have been able to expand my meteorological knowledge through involvement in field experiments, travel to conferences, and more. The guidance you have given me has been invaluable, and you have been great role models for the scientist I want to become in the future. I would also like to thank my committee members, Dr. Robert Palmer, Dr. Alan Shapiro, and Dr. Scott Salesky for taking time out of their busy schedules to provide feedback on this work. Furthermore, I would like to thank Professor Maruyama at Kyoto University for providing support and guidance to conduct these simulations. I would also like to thank Professor Takanori Uchida at Kyushu University for providing the RIAM-COMPACT software and allowing its use for this research project.

I would like to thank my close friends, with whom I will always cherish the good times, and for always providing good laughs through stressful times. I would especially like to thank my wife, Clarice Satrio, for agreeing to marry me during our graduate school journey and who has by my side not only through my graduate career, but through my undergraduate and high school career. You have always kept my spirits high throughout the entire process, and this work would not have been possible without the support and strength that you have given me.

Finally, I am grateful for both of my siblings; my brother, for always sharing all the hilarious moments with me and my sister, for being an amazing role model and showing me the value of hard work. I am extremely thankful both of my parents, Rubianto and Lidwina Satrio, who have always taken care of me and always supported my dream of being a meteorologist. From getting me my first weather station to buying many weather books, you have always encouraged me to do what I love. You have molded me into the person I am today, and I could not ask for better parents.

Table of Contents

List Of Tables

List Of Figures

Abstract

Tornado structure is known to be sensitive to the characteristics of near-surface inflow, which in turn is affected by inhomogeneities in surface features. Many observational studies such as VORTEX-SE have identified potential influences of terrain on tornado dynamics, particularly in areas of complex terrain such as the southeast United States. However, investigating terrain effects observationally poses a number of challenges, including temporal and spatial limitations. While past studies have resorted to damage analysis and numerical simulations to examine such effects, a comprehensive sensitivity study on the effects of various types of terrain on tornadoes has yet to be done. Examining the behavior of tornadoes that traverse terrain features may aid in understanding patterns of tornado strengthening / weakening and give insight on damage patterns left behind from complex near-surface flow structure in areas of complex surface terrain. In the present study, a large-eddy simulation (LES) model is utilized to simulate a tornado-like vortex moving at a fixed translational velocity over varying surface terrain. An immersed boundary method modifies the Navier-Stokes equations at the terrain feature such that all components of the ground-relative components of the flow are forced to zero. Different simulations are grouped into one of four categories depending on terrain type - 3D hills, 2D sinusoidal hills, valleys, and ridges - and within each of these categories slight modifications to the characteristics of the terrain or the vortex are implemented to examine the vortex's response to certain changes.

The study finds that as the vortex traverses the different terrain features, the vortex becomes unsteady and asymmetric, especially at levels nearest to the surface where friction

plays the largest role. For 2D sinusoidal and 3D hill simulations, enhanced 10-m horizontal wind speeds occur in two distinct areas: 1) in between adjacent hills as a result of flow channeling and 2) on the upslope portion of the hill which is a product of short-lived but robust secondary vortices. The secondary vortices are hypothesized to form as a result of stretching of pre-existing vertical vorticity, associated with terrain-induced enhanced convergence. Analysis of the pressure field at 10 m show that the addition of terrain into the LES model does produce predictable path deviations that repeat with respect to the terrain, with a southern (northern) preference on the downslope (upslope) side of the hill. Additionally, composite analyses reveal that the near-surface core radius is widest (most narrow) as the vortex ascends (descends) the terrain. The valley simulations have the largest horizontal wind speed and the ridge simulations have the highest vertical wind speeds overall. For hill and sinusoid cases, the region between adjacent hills have the fastest horizontal winds and the uphill side has the largest vertical winds. Statistical calculations also show overall horizontal and vertical wind speeds as well as turbulent kinetic energy values are a function of the overall characteristics of surface terrain such as the slope and size.

Chapter 1

Introduction

By total count, tornadoes are more common in the United States than in any other country NOAA National Centers for Environmental Information (2010), and they can have both devastating economic and societal impacts. In 2018, the economic loss from natural catastrophes in the United States totaled $52.3 billion, $14.1 billion of which fell under the category of severe thunderstorms, including tornadoes (Property Claim Services 2019). Property Claim Services (2019) also calculated that from 1997 to 2016, severe thunderstorms and tornadoes accounted for 40% of all insured catastrophe losses, and a single severe weather outbreak can cause upwards of $7 billion in insured losses. In addition to the financial cost of tornadoes, in the 20-year period from 1999-2018, there were a total of 1,521 fatalities, an average of 76 fatalities annually (SPC 2016). 553 of those fatalities occurred in 2011 alone.

The two most common areas for tornadoes in the United States is over the southern Great Plains region and central Florida, with > 7 tornadoes annually per 10,000 square miles (Figure 1.1). Although the terrain over both central Florida and the southern Great Plains region is relatively flat, tornadoes still occur relatively often in areas where the terrain is more complex. Areas just east of the Rocky Mountains are characterized by complex terrain with a relatively high annual number of tornadoes, for example in northeast Colorado / southwest Nebraska with 5-7 tornadoes per 10,000 square miles annually. Over the

AVERAGE ANNUAL FREQUENCY OF TORNADOES IN THE UNITED STATES

United States Tornado Occurrence per 10,000 square miles

0 0.5 1 3 5 7

Annual Average (1950 - 1995)
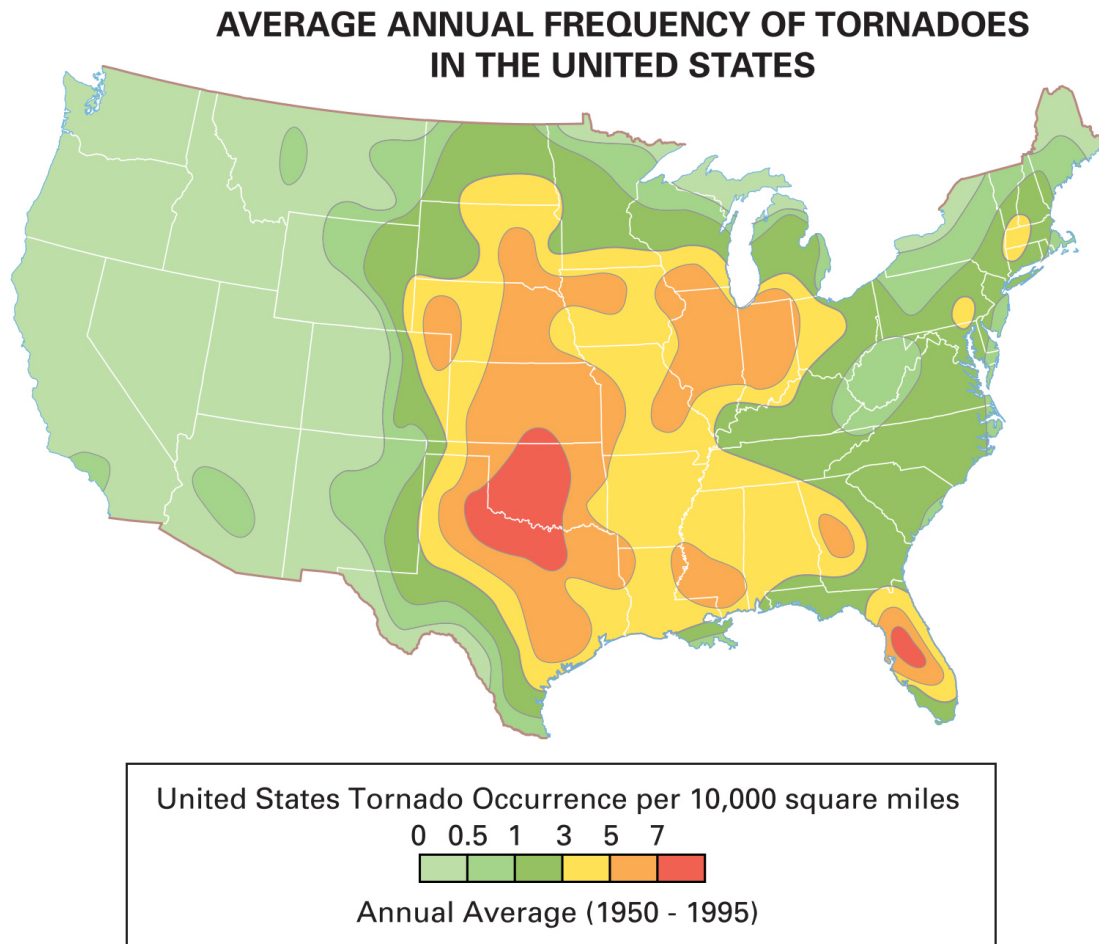
Figure 1.1: The average occurrence of tornadoes in the United States per year (Snow 2019).

Figure 1.2: Topographic map of the United States.

southeast United States - Tennessee, northern Alabama, and northern Georgia, especially - complex terrain influenced by the nearby Appalachian Mountains also occurs in conjunction with relatively high number of annual tornadoes with 3-5 tornadoes per 10,000 square miles (Figure 1.2). Even in areas far from large mountain ranges, such as the northeast United States, subtle terrain features have been noted to influence tornado formation and dynamics (Bosart et al. 2006; Tang et al. 2016). Lastly, even in Oklahoma, subtle terrain features that are comparable to the simulations studied herein can be found.

While the understanding of tornado formation and behavior has improved over the last few decades, the effects of terrain on tornado dynamics remains relatively unknown. One of the main points of emphasis for the VORTEX-SE project in the southeast United States was to target observations in complex terrain. However, obtaining a comprehensive radar

data set of a tornado traversing a significant terrain feature presents difficult challenges. Not only does beam tilt and earth curvature prevent data collection at levels closest to the surface, but a significant terrain feature would likely produce beam blockage problems. The data must be of high temporal resolution as terrain features (slope, height, etc.) would change rapidly with respect to tornado location. Additionally, acquiring true wind measurements of the tornado would require precise positioning of multiple radars while the tornado traverses the terrain. Thus, the number of studies relating how different types of terrain features affect the overall tornado wind field is somewhat limited.

Several past studies have investigated cases of tornadoes traversing terrain. Schneider (2009) analyzed three different tornado events that occurred over the Great Tennessee Valley. The study noted multiple effects from surface terrain that led to an increased likelihood of tornadogenesis, including low-level convergence, upslope flow resulting in updraft and mesocyclone strengthening, pooling of low-level moisture creating localized baroclinic vorticity, backing of surface wind through valley channeling resulting in larger storm-relative helicity values, and forced stretching of vertical vorticity when moving from higher to lower terrain. Bosart et al. (2006) also analyzed a tornadic supercell over Great Barrington, Massachusetts and noted that the mesocyclone showed patterns of weakening / strengthening aligning with complex terrain, and hypothesized that flow channeling from topographic configurations enhanced tornadogenesis likelihood. Similarly, Tang et al. (2016) noted that flow channeling associated with the Mohawk Valley in New York led to a maximum in moisture flux convergence and a subsequent rapid strengthening of the supercell as it moved into the valley. In a numerical simulation of a supercell, Markowski and Dotzek (2011) compared thermodynamic environments between simulations with and

without terrain. Simulations with terrain showed heterogeneities in storm environments, including areas of more favorable thermodynamic environments which were directly attributed to effects of airflow forced over or around terrain features.

Damage surveys have also been utilized in analyzing terrain effects on tornadic wind distributions. Fujita (1989) analyzed the damage swath the Teton-Yellowstone EF-4 tornado of 21 July 1987 and found a weakening of the tornado as it ascended a 3000-m plateau. Before ascent, Fujita (1989) hypothesized that microbursts far from the tornado supplied high angular momentum air which was key in its maintenance and strengthening. During ascent, microbursts were forced closer to the tornado, disrupting angular momentum balance and weakening the tornado. More recently, Karstens et al. (2013) analyzed tree-fall patterns associated with both the 2011 May 22 Joplin, MO EF-5 tornado and the 2011 April 27 EF-4 Tuscaloosa-Birmingham, AL tornado. The study noted enhanced tree-fall swaths to the left of the tornado far from the center and parallel to valley channels, suggesting that flow channeling associated with terrain features was enough to induce tree-fall where it would otherwise not occur. However, a shortcoming in studying terrain effects through damage surveys is that damage indicators in sparse areas can produce difficulties in comparing results between regions, i.e. regions on a tall hill / slope are likely to be less populated than in a valley or plateau.

Lewellen (2012) (hereafter, L12) presented a preliminary study on terrain effects on an idealized tornado using large-eddy simulation (LES). The tornado was subjected to various terrain features including two adjacent hills, a valley oriented perpendicular to the translation of the tornado, a double ridge, a gapped ridge, and a slanted ridge. L12 noted that the terrain induced vortex tilt, path deviations, and overall variations in structure and strength

of the vortex. L12 found as the vortex ascended (descended) the ridge, the lower end of the vortex accelerated (decelerated) and tilted forward (backward) such that the central axis of the lower portion of the tornado was perpendicular to the terrain surface. Additionally, L12 noted a deflection of the tornado to the left (right) relative to tornado motion as the tornado ascends (descends) the ridge and vice versa as the tornado interacts with the valley.

The present study aims to expand upon results presented in L12, as well as make further generalizations on the effects of terrain on tornadoes. The goal is to address questions about terrain effects that remain unclear, including 1) what, if any, terrain effects can be generalized, 2) whether effects over different types of terrain can be generalized, 3) what magnitude of terrain changes are necessary to affect tornadoes, and 4) what overall variability in near-surface wind speeds and damage potential result from terrain effects. The spectrum of terrain features in this study is broad, yet carefully chosen so that the above questions can be addressed. Thus, both the effects of different types of terrain (e.g., hill versus valley) and effects of subtle changes to the same type of terrain (e.g., small vs large hill) on tornadoes can be quantified. To accomplish this, an LES model with high spatiotemporal resolution is utilized, similar to L12. Outer and upper boundary conditions are such that a tornado-like vortex is created while terrain features are implemented through an Immersed Boundary Method (Saiki and Biringen 1996), which forces all components of the flow at the terrain points to match the surface translation velocity. The tornado is translated over the terrain and variations to the resultant model output (e.g., wind, pressure) are analyzed to understand what effects, if any, the terrain has on the tornado.

Chapter 2 starts with an overview of tornadoes and details each region within a tornado. This is followed by a discussion on past studies of tornadoes, both observational and numerical. Chapter 3 then describes specifications of the LES model used in the present study, detailing both boundary conditions of the model and the method for implementing terrain into the domain. In Chapter 4, specific simulations which are grouped by terrain type, are highlighted in great detail to analyze how the tornado reacts to the terrain throughout the entire simulation and how tornado behavior changes with small variations in the terrain. This is accomplished by analyzing both maximum horizontal and vertical winds along the track of the tornado and time-height plots of axisymmetric variables. Chapter 5 provides higher-level analysis to generalize results across all simulations to answer generalized questions posed in the paragraph above. Data in this chapter are presented in statistical calculations organized by both terrain type and tornado position relative to the terrain. Lastly, Chapter 6 presents conclusions and recommendations for future work.

Chapter 2

Tornadoes

2.1 Overview

The Glossary of Meteorology defines a tornado as a "rotating column of air, in contact with the surface, pendant from a cumuliform cloud, and often visible as a funnel cloud and/or circulating debris/dust at the ground" (Glickman 2000). Whether the condensation funnel reaches the surface is dependent on whether the pressure deficit is large enough such that a parcel of air reaches its saturation point as it is drawn inwards. While some tornadoes last longer than 1 hr with a diameter of more than 2 km, the majority of tornadoes last less than 10 minutes and are smaller than 200 m in diameter. The weakest tornadoes last less than a minute and are just tens of meters wide.

Tornadoes can be divided into two types, type-I and type-II (Davies-Jones and Kessler 1974; Davies-Jones et al. 2001). A type-I tornado is associated with a low-level rotating updraft, typically a mesocyclone, whose diameter can range from a few kilometers to about 10 km. The upper region of the tornado and the lower region of the parent mesocyclone are connected. Long-track, violent tornadoes are almost always type-I tornadoes whose associated mesocyclone is part of a parent supercell. A supercell is defined as a convective storm that has a persistent, quasi-steady rotating updraft which persists for a long period of time (>1 hr) and is associated with numerous severe weather hazards (Davies-Jones et al.

2001). Every supercell falls into one of three distinct classifications: low-precipitation (LP), classic, and high-precipitation (HP) (Lemon and Doswell 1979). The names are self-explanatory: LP supercells contain little precipitation and rain-cooled air, although they are still capable of producing large hail. HP supercells produce copious amounts of precipitation and rain-cooled air and as a result, the mesocyclone can become completely wrapped in precipitation. The most common are classic supercells, which are intermediate between HP and LP supercells. All three types of supercells are capable of producing tornadoes of varying strengths. Although supercells always have a mid-level mesocyclone associated with them, only about 25% of all supercells produce a tornado (Trapp et al. 2005) and an even smaller percentage produce violent tornadoes.

Type-II tornadoes are not associated with a parent circulation and are generally weaker and shorter-lived than the average type-I tornado, commonly referred to as "landspouts" or "waterspouts". Type-II tornadoes generally form along a windshift line associated with enhanced near-surface vertical vorticity (Golden 1974b; Wilson 1986; Wakimoto and Wilson 1989). When an updraft becomes collocated with a vorticity maximum, the vorticity is enhanced by stretching until a type-II tornado forms. Common places for type-II tornadoes include off of the Florida coast owing to the land/sea-breeze interaction, whose characteristics have been extensively studied (Golden 1971, 1973, 1974a,b; Leverson et al. 1977; Simpson et al. 1991; Wakimoto and Lew 1993). As a result, the state of Florida sees the third-most tornadoes annually. A land equivalent is the Denver Convergence Zone (Szoke et al. 1984; Wilczak et al. 1992; Wakimoto and Martner 1992; Roberts and Wilson 1995), or the DCZ, where landspouts are a common occurrence. Gustnadoes are also classified as type-II tornadoes and form along the gust front of a supercell or line of thunderstorms. They

9

are short-lived and most often seen as quick dust whirls on the surface. For type-II torna-does, the lack of a strong parent mesocyclone along with the absence of a strong, sustained updraft causes most to be weak and short-lived. Of course, there are a handful of cases in which type-II tornadoes are long-lived and visually impressive. More recently, there has been a proposed re-classification of tornadoes to three taxonomic classes (Agee and Jones 2009) which includes the two presented here with an addition of a third taxonomic class - tornadoes associated with quasi-linear convective systems.

Based on data from 1985 - 2014 (SPC 2016), the annual average of tornadoes in the United States is 1141. The central U.S. constitutes a geographical area well-known as "Tornado Alley". During the spring months in Tornado Alley (peak climatology being late May), a westerly jet stream is positioned over the Rockies and the southern Great Plains, producing enough vertical wind shear to support supercellular storm modes. As the air descends over the Rockies, a lee trough forms due to cyclogenesis from stretching of the air as it descends the slope. This lee trough then creates cyclonic flow around it, leading to south or southeasterly low-level flow in the Great Plains region. This low-level flow not only advects very warm, moist air from the Gulf of Mexico into the Great Plains, but also leads to veering winds with height, a necessary condition for supercell organization. The dryline, where the moist Gulf air meets the very warm, dry air descending from high terrain in CO and NM, is a main point of interest for storm initiation (Rhea 1966; Sun 1987; Bluestein and Crawford 1997; Ziegler et al. 1997; Hane et al. 2002; Demoz et al. 2006; Buban et al. 2007; Wakimoto and Murphey 2009). Dry, warm air is also advected off the Rockies and produces an elevated mixed layer, creating a stable layer just above the warm, moist air in the warm sector. For this reason, the most common time for supercell

thunderstorms and tornadoes to form is during the late afternoon and into the evening when surface temperatures have had sufficient time to warm and overcome convective inhibition.

Based on the same 30-year average, the annual number of fatalities from tornadoes in the United States is 73. By EF-rating (Table 2.1), although violent tornadoes (EF-4+) only accounted for 0.65% of all tornado occurrences, they accounted for 51.7% of all fatalities. Strong tornadoes (EF-2+) accounted for 11.9% of all tornado occurrences and accounted for 94.5% of fatalities. EF-0 tornadoes accounted for 59.2% of tornadoes from 1985-2014. EF-5 tornadoes are so rare that during that 30-year period, there was a total of 20 EF-5 tornadoes in 12 different states; only 12 years out of the 30 year period saw an EF-5 tornado. Between 2000 and 2006, there were no EF-5 tornadoes, though this may result more from the absence of adequate damage indicators rather than an absence of tornadoes producing EF-5 winds.

Table 2.1: EF-Rating along with the associated 3-s wind gust.

EF-Rating	3-s Wind Gust (mph)
EF-0	65-85
EF-1	86-110
EF-2	111-135
EF-3	136-165
EF-4	166-200
EF-5	> 200

Because of the current inability to measure a tornado's near-surface wind speed accurately and consistently, the EF-scale is not reliant on measured wind speeds but rather by the damage it inflicts on surrounding structures (e.g, trees, houses, buildings) using the underlying assumption that damage increases with wind speed. The Fujita scale, or the F-scale, was introduced by Ted Fujita after studying an extensive amount of tornado damage

surveys (Fujita 1971). In 2007, a team of meteorologists and engineers revised the Fujita scale and implemented the Enhanced Fujita Scale (McDonald et al. 2004; WSEC 2006), or the EF-scale. The revision was necessary to better estimate wind speeds based on damage assessment from a wider range of damage indicators and is significantly more detailed on the degrees of damage. The EF-scale also takes into account construction quality of a particular structure. The degree of damage is then used to estimate the wind speeds in the tornado.

2.2   Tornado Structure

Even tornadoes that have a laminar appearance are inherently turbulent and asymmetric, especially near the surface. However, it is helpful to envision an idealized, axisymmetric vortex split into 5 main regions (Figure 2.1). Region Ib is the outer flow region located at a radius greater than the core radius (radius of maximum tangential velocity) and above the boundary layer. Region Ia is the core region also located above the boundary layer whose radius extends from the center to the core radius. Region II is the boundary layer, where the flow is impacted by surface friction. Region III is the corner flow region, where the flow rotating inwards turns sharply upwards. As will be discussed later, the corner flow region is crucial as this is where the most violent winds occur and where the potential for debris lofting is highest. Lastly, Region IV is the upper flow region where the upper region of the tornado and the lower region of the parent mesocyclone connect. After details of each region is discussed, an example from the LES model is shown to aid in the visualization of tornado regions.

2.2.1 Core and Outer Flow Region

The core region extends from $R = 0$ to $R = R_c$ (core radius) at a height where frictional effects become negligible. The outer flow region starts at $R = R_c$ and extends outwards at least 1 km from R_c. Flow in the outer flow region has a small radial component inwards and conserves angular momentum, M. Therefore, as the flow rotates inwards towards the core, its tangential velocity increases. The flow within the core region varies depending on R_c. Narrow core regions tend to be in solid body rotation (constant angular velocity) while angular velocity in wider cores increase from the center as R tends to R_c (Davies-Jones et al. 2001). Depending on the tornado flow characteristics such as the swirl ratio (Church et al. 1979), a measure of the tangential velocity to the vertical velocity, the inner core region may consist of positive (updraft) or negative (downdraft) vertical velocities. Though the core and outer flow region are adjacent to each other, the inertial stability of the core region dictates that the air in the core region must come from below or even above, i.e. there is very little entrainment from the outer flow region into the core region.

2.2.2 Boundary Layer

Region II is the tornado boundary layer, characterized by the region in which surface friction can no longer be neglected. Even for smoother surfaces, it is generally accepted that the Reynolds number in this region is large and therefore, the flow is dominated by turbulence. The depth of the tornado boundary layer does increase with surface roughness, but typically does not extend up more than 100 m AGL in contrast to the atmospheric boundary layer which is typically $\sim$1 km in depth. Flow in this region is such that the horizontal
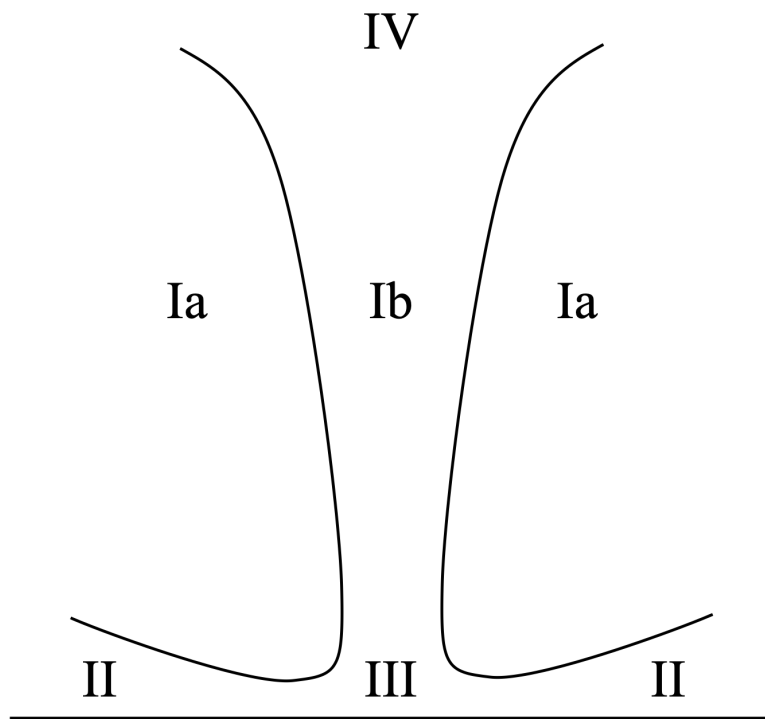
Figure 2.1: Flow regions of a tornado. Region Ia is the outer flow region, Ib is the core region, region II is the boundary layer, region III is the corner flow region, and region IV is the upper flow region. Adapted from Lewellen (1976); Davies-Jones et al. (2001).

component dominates over the vertical component. Additionally, frictional effects disrupt cyclostrophic balance between the pressure gradient force (PGF) and the centrifugal force. Since the centrifugal force is dependent on tangential velocity which is reduced from frictional effects, the PGF outweighs that of the centrifugal force, leading to a strong radial component of the flow. The angular momentum equation, $M = vR$ (where v is tangential velocity), dictates that this increase of radial inflow in the boundary layer can result in extreme wind speeds with larger values here compared to aloft. Though M is frictionally-depleted in the boundary layer, if the decrease in R from strong radial inflow outweighs the depletion of M, the mathematical result is that v must increase to balance the equation. Unfortunately, as a result of beam tilt, low-level beam blockage, and earth curvature, it is most often the case that radar observations of tornadoes miss or under-sample this region. Therefore, much of what is known about the boundary layer has been studied through physical and numerical simulations of vortices.

2.2.3 Corner Flow Region

As the flow from the boundary layer rotates inwards, the flow must eventually turn sharply upwards due to mass continuity. The region where this occurs is the corner flow region. This region is arguably the most important region as it is where the highest wind speeds occur, the most damage is inflicted, and is the reason debris can get lofted far up into the storm. The vertical PGF is much larger in the corner flow region than in the boundary layer. The upper-half of this region is where the largest tangential velocities are found; the flow penetrates much closer to the central axis compared to the upper flow region, but the effect of friction is not large enough such that the angular momentum depletion outweighs the

decrease in radius. The dynamics of the corner flow region are also responsible for vortex breakdown, including if subvortices exist, and if so, how many there are.

There are many different categorizations of tornado structure (Lee and Wurman 2005; Kosiba and Wurman 2010; Wurman et al. 2013), one categorization being whether or not the tornado has undergone vortex breakdown with secondary vortices. Whether or not vortex breakdown occurs is dependent on the swirl ratio, a ratio of the tornado's swirl velocity and the its vertical velocity given by

$$S = \frac{r_0 M}{2Q} \tag{2.1}$$

where $Q = \int_0^r w r' dr'$. $2\pi M$ is a measure of the circulation at the edge of the updraft while $2\pi Q$ represents the volume flow rate of the updraft, with representative values chosen away from the boundary layer. Theoretically, vortex breakdown occurs after the swirl ratio, S, is greater than unity (Church et al. 1979). Under very small S, the flow in the boundary layer is unable to penetrate all the way to the center and flow goes around the corner flow region, resulting in an updraft aloft and no tornado at the surface (Figure 2.2a). At slightly higher S, the flow penetrates closer to the center resulting in a one-cell vortex (Figure 2.2b). Further increase in S introduces an axial downdraft aloft and thus, the vortex jumps to a two-cell vortex aloft where the downdraft splits the updraft into an annulus (Figure 2.2c-d). Eventually for large enough S, the downdraft impinges to the surface, i.e. a two-celled vortex throughout the depth of the tornado (Figure 2.2e). Lastly, for large S, the tornado breaks down into a larger number of subvortices (Figure 2.2f). While in actuality other factors such as surface friction and terrain play a role in tornado structure Uchida and Ohya

16
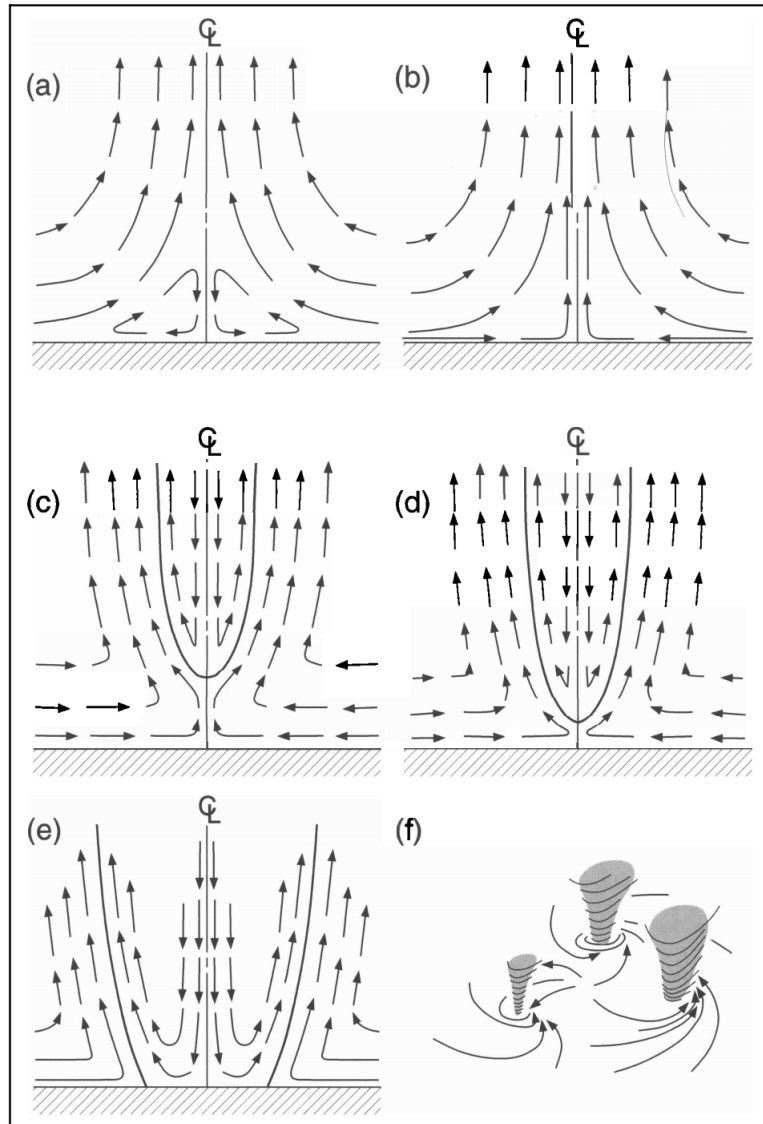
Figure 2.2: An illustration of vortex structure as a function of swirl ratio. a) Very weak *S* - the flow coming inwards towards the axis of rotation is forced around the corner flow and therefore, no tornado forms. b) Low *S* - flow coming inwards penetrates to the center of rotation then turns upwards, resulting in a one-celled vortex. c) Moderate *S* - Flow in the boundary layer penetrates towards the center resulting in a smooth end-wall vortex that abruptly jumps to a two-celled vortex aloft as a result of an axial downdraft. d) Moderate-high *S* - axial downdraft close to impinging to surface, illustrating a transition to a two-celled vortex. e) Large *S* - axial downdraft now clearly impinges on the ground and results in a two-celled vortex at the surface. f) Larger *S* - tornado breaks down further into multiple vortices. Adapted from (Davies-Jones 1986)

.

(2003); Lewellen (2012), Figure 2.2 illustrates the significant changes that occur in the corner flow region as swirl ratio is modified.

As a testament to the importance of the corner flow region, Lewellen et al. (2000) defined a new corner flow swirl ratio. The corner flow swirl ratio characterizes the surface-layer core flow that is embedded within the larger scale flow, described by S. While the corner flow swirl ratio does not redefine S, it is used to describe flow in the corner flow region and is best used in conjunction with S for a complete analysis. Lewellen et al. (2000) uses S_c to quantify effects that modify the surface inflow layer and thus the corner flow region, but do not necessarily modify the overall flow structure, such as surface roughness or translation speed. Mathematically, it is defined as

$$S_c = \frac{r_c M_\infty^2}{\Upsilon} \tag{2.2}$$

where

$$\Upsilon = 2\pi \int_0^{r_2} <w(r,z_2)\Gamma_d(r,z_2)> r dr \tag{2.3}$$

and

$$\Gamma_d = \Gamma_\infty - \Gamma \tag{2.4}$$

In Equations 2.2 - 2.4, M_∞ is a representative value of M safely outside the the upper core region at r_2 and z_2 is a height just above the corner flow region. Υ is the depleted M flux in the corner flow region and Γ_d is depleted angular momentum. The brackets "$<>$" indicate time-averaged and axisymmetric values. S_c highlights the importance of low-angular momentum fluid which flows inward towards the center and becomes the upper core flow.

Lewellen et al. (2000) concludes that while S_c does vary directly with the more general swirl ratio, S, S_c is also dependent on other variables such translation speed and surface roughness or terrain. Increasing inflow of low M fluid at low-levels (e.g., by increasing surface roughness) leads to a reduction in S_c. On the other hand, S_c is increased by parameters that increase the radius of the upper-core without changing surface layer inflow (e.g., addition of an axial downdraft). Holding S constant while decreasing S_c leads to a maximization of low-level vortex strength at a critical S_c value. A vortex breakdown state is considered to be near this critical value (Fiedler and Rotunno 1986). Further decrease in S_c from the critical point produces a vortex with very little low-level intensification.

2.2.4 Upper Flow Region

Due to the location of the upper flow region embedded within the parent mesocyclone, this region is difficult to study observationally. The upper limit of the upper flow region is dependent on the strength of the tornado. For small to moderate tornadoes, the tornado's circulation may only reach a few kilometers up in the atmosphere. For these cases, the circulation may become inertially unstable and turbulent eddies transport parcels outwards from the center of rotation (Mulen and Maxworthy 1977; Lewellen et al. 1993). The warm, buoyant air parcels then act as a cap to prevent the low-pressure core from being filled in with air from above (Fiedler 1995). For larger, more violent tornadoes, the circulation and upward motion may reach past the equilibrium level, resulting in an overshooting top. The buildup of air in the overshooting top creates a relative high pressure and similarly, parcels are transported outwards by the PGF.
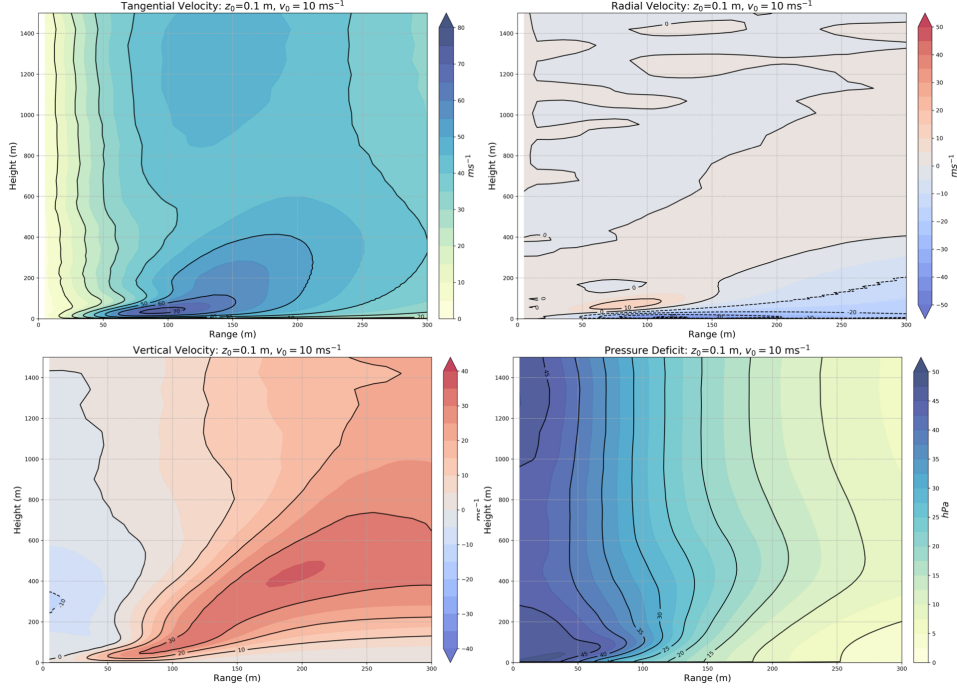
Figure 2.3: Time-averaged axisymmetric results from the LES simulation using a surface roughness of $z_0 = 0.1$ m and a translational velocity of 10 m s^{-1}. Variables shown are tangential velocity (top left), radial velocity (top right), vertical velocity (bottom left), and pressure deficit (bottom right).

2.2.5   LES Example

It is helpful to visualize the regions of the tornado using an example from the LES model (Figure 2.3). The tornado has a translational velocity of 10 m s^{-1} and a surface roughness length of $z_0 = 0.1$ m with a total analysis time of ~400s. Above 100 m frictional effects are negligible, resulting in constant tangential velocity with height and weak radial velocities. Additionally, pressure deficit decreases linearly with R. The core radius lies at $R \approx 150$ m, so the upper core region (outer flow region) is found inside (outside) this radius. Inside the upper core region, the axial downdraft impinges close to the surface with a minimum w of < -10 m s^{-1}.

Below 100 m AGL, frictional effects play a large role in the characteristics of the flow. The boundary region exhibits a shallow but strong layer of radial inflow $> 40\,\mathrm{m\,s^{-1}}$. Tangential velocities in the boundary layer are stronger than in the upper core / outer flow region for a given R, as frictional depletion of M is unable to counteract the decrease in r. As a result of the of the lack of a strong vertical PGF, vertical velocities in the boundary layer are weak, in general $< 10\,\mathrm{m\,s^{-1}}$ (Figure 2.3).

The corner flow region is marked by a maximum in the tangential velocity $> 70\,\mathrm{m\,s^{-1}}$ at $R \approx 100$ m and $Z \approx 50$ m. The radial inflow penetrates closest to the central axis here, producing the maximum in tangential velocity. The tangential velocity maximum is collocated with a region of strong radial inflow $> 40\,\mathrm{m\,s^{-1}}$ just above the surface and an area of strong radial outflow $> 10\,\mathrm{m\,s^{-1}}$ just above the inflow. Strong $w > 30\,\mathrm{m\,s^{-1}}$ also exists in this region resulting in an "in-up-out" motion, and larger pressure deficits from the center bulge outwards.

The tornado in this case has a moderate swirl ratio, and its structure resembles that found in Figure 2.1. The downdraft impinges very close to the surface, representing a near-surface vortex breakdown case and creating an end-wall vortex near the surface that becomes a two-celled vortex aloft. Note that it is not possible to discern the upper flow region in this case as the top of the domain is at $Z = 2$ km and all motions at that level are governed by upper boundary conditions.

2.3   Past Studies

The violent and unpredictable nature of tornadoes have made them an interesting target of research. However, the same characteristics that make them interesting also have made them notoriously difficult to study. Approaches to investigating tornadoes include both observational and numerical methods, each with their own set of advantages and disadvantages to understanding tornado behavior. Past studies have attempted to understand multiple phenomena associated with tornadoes such as tornadogenesis mechanisms, tornado dissipation, tornado structure, etc. While the main focus of the present study is on the effects of terrain on tornadoes, a brief summary of past experiments that have been key in developing current understanding are discussed in this section.

2.3.1   Observational Field Studies

Perhaps the most straightforward way to observationally study tornadoes is through radar data. The use of weather radars was discovered during World War II when radar operators discovered that hydrometeors were disrupting their ability to observe enemy planes. Soon after, radars were developed to specifically target weather phenomenon. The first network of national radars were the WSR-57 radars, which gave low resolution radar images and no velocity data. This made it nearly impossible to accurately predict and monitor tornadoes; however, this first network of weather radars allowed for initial research and observations of supercell storms and the associated hook echo. The national network was upgraded to WSR-88D radars (Crum and Alberty 1993) in the 1990s, which not only gave much higher resolution but Doppler velocity data as well. Experiments with a prototype Doppler radar

by the National Severe Storms Laboratory revealed the tornado vortex signature (TVS), highlighted by adjacent strong outbound and inbound velocities (Brown et al. 1978; Brown and Wood 1997). Once Doppler capability was added to the nationwide network, considerable improvements in tornado warning capabilities resulted (Mitchell et al. 1998). The network was nationally upgraded to dual-polarization capabilities in 2013, allowing for both horizontal and vertical polarization pulses, which provides the ability to distinguish hydrometeor characteristics such as size, shape, and orientation. This also led to the discovery of a tornado debris signature (TDS), identified by a velocity couplet, high reflectivity, low correlation coefficient, and low differential reflectivity (Ryzhkov et al. 2005).

Even with the upgrade to a dual-polarization WSR-88D network, studying tornado-scale phenomena still posed a number of challenges. The spatial resolution of super-resolution level II data from the WSR-88Ds is 0.5°in azimuth and 250 m in range (Torres and Curtis 2007) while tornado scale phenomena, especially those associated with small tornadoes, are on the order of tens of meters. Even with close positioning of the radar relative to the tornado, tornado wind structure is only marginally resolved (sometimes only "gate-to-gate"). While tornado scale phenomena can occur on the order of seconds, temporal resolution of WSR-88D radars is up to $\sim$ 2.5 min using Supplemental Adaptive Intra-Volume Low-Level Scan (SAILS) scanning strategy. Therefore, the entire life cycle of a short-lived tornado (formation, maturation, and dissipation) can occur between two subsequent radar scans. Lastly, due to beam tilt and curvature of the Earth, the beam itself may scan the mesocyclone rather than the tornado, since the tornado typically occurs in the lowest 1 km of the atmosphere.

In order to combat the deficiencies of fixed radars, mobile Doppler radars are built with the intention of capturing storms at a higher temporal and spatial resolution. Mobility of the radars eliminates the chance game of waiting for a tornado to pass close to the radar. One mobile radar example is RaXPoL (Pazmany et al. 2013; Snyder and Bluestein 2014; Houser et al. 2015), a rapid-scanning dual-polarization X-band radar that can complete a full volume scan of 10 elevations in 20 s, i.e. the radar can complete a single-elevation PPI in 2 seconds. Other mobile radars capable of capturing high-resolution data include the Atmospheric Imaging Radar (Isom et al. 2013; Kurdzo et al. 2017; Mahre et al. 2018; Griffin et al. 2019) and the PX-1000 (Kurdzo et al. 2015).

Numerous field experiments such as Verification of the Origins of Rotation in Tornadoes Experiment (VORTEX) (Bluestein et al. 1997; Ziegler et al. 2001), VORTEX2 (Wakimoto et al. 2011, 2012; Wurman et al. 2012) and VORTEX-SE have utilized mobile radar to study severe thunderstorms and tornadoes. The main advantage of using radar observations to study tornadoes is that the data are real. However, even with rapid-scanning mobile radar, there are severe limitations in studying tornado behavior using radar, including the inability to retrieve all thermodynamic, microphysical, and dynamic parameters of interest three-dimensionally. Though the data are not "real", numerical simulations allow for both analysis of three-dimensional parameters and more control over variables that may impact tornado behavior, e.g., swirl ratio, surface roughness, etc.

2.3.2 Laboratory Simulations of Tornadoes

Though laboratory simulations are not widely used today, these setups were key in identifying important features in tornado structure. Though technically observational, laboratory

24

experiments idealized in the sense that the user can exercise control over variables. For example, the Purdue Ward Chamber (Ward 1972; Davies-Jones 1973; Church et al. 1977; Davies-Jones 1986; Maxworthy 1982; Church and Snow 1993) was useful in modeling a plethora of tornadic characteristics including pressure distribution and different types of tornadic vortices. The Ward Chamber allowed for initially nonrotating fluid to enter the core from below with dimensions proportional to typical tornado / mesocyclone structure. More specifically, the aspect ratio $a = H/r_0$, where H is the height between the top of the inflow region and the updraft r_0 is the radius of the updraft hole, is approximately 1, a typical value from tornado observations. There was a rotating screen at $r = r_s$ where $M = 2\pi\Gamma_s$, Γ_s representing the circulation at radius r_s (Figure 2.4). The fluid was of constant density and dynamic viscosity of ρ and μ, respectively, giving a constant kinematic viscosity of $\nu = \mu/\rho$. The updraft is driven by an exhaust fan at the top producing a volume flow rate of $2\pi Q$ through an opening of radius r_0 while air flows in through the bottom of the model. The vortex is terminated at the top by a honeycomb baffle. The flow structure was found to be mostly dependent on the swirl ratio given by $S = \frac{r_0\Gamma_s}{2Q}$, similar to results in Section 2.2.

Though the Ward Chamber was useful in studying some characteristics of vortex structure, there were significant limitations in drawing the results to observed tornadoes. Firstly, the flow is all dynamically driven and there is no thermodynamics involved, e.g., no warming (cooling) when air descends (ascends). Secondly, though the swirl ratio in the simulator can be adjusted, the updraft at the top is held fixed not allowing for any variations with the parent mesocyclone, as would most likely occur in an observed case. A largest issue, however, is with the honeycomb baffle; the baffle can result in significant changes in the pressure and wind fields which in turn affects vortex behavior (Smith 1987). Lastly,
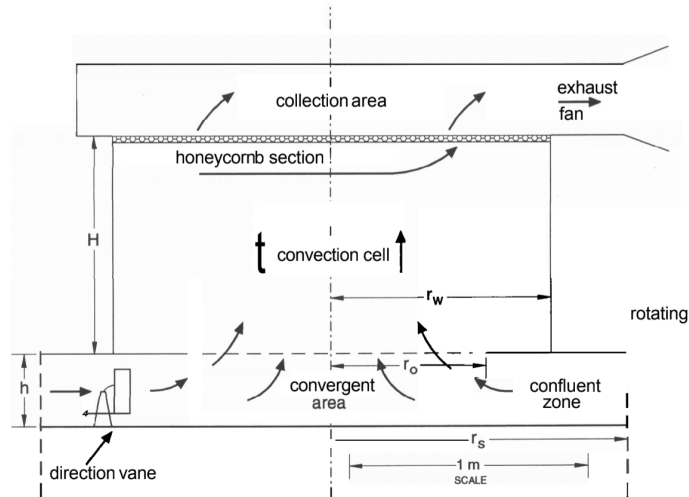
Figure 2.4: Design of the Ward Chamber which had the ability to produce a wide range of tornado-like vortices.

when comparing flow in the Ward Chamber to an observed case, the flow in the chamber is too laminar. Other laboratory experiments have the same limitations, thus most idealized studies associated with tornadoes is approached numerically.

2.3.3   Numerical Simulations of Tornadoes

Much of what is known about vortex flow structure originates from numerical simulations. Numerical simulations allow for the control of variables as well as the ability to read data such as pressure, wind, temperature, etc. at every grid point, giving them an advantage over laboratory simulations or radar observations. The first numerical simulations of a tornado were based off of laboratory experiments such as the Ward chamber. Rotunno (1979) at NCAR was the first to do this with open side boundaries specifying inflow / outflow conditions. Fiedler (1994) (hereafter, F94) improved the model by introducing closed side boundaries, eliminating the issue of unknown flow beyond the open boundaries.

In Fiedler's model, the model contained the entire rotating updraft, prescribed by a buoyancy force $b(r,z)$, with the top boundary representing the tropopause. Variables are restricted to realistic values found within supercells. F94 finds that the solution to the flow again depends on two non-dimensional variables: 1) swirl ratio defined by $\Omega = \frac{\omega h}{W}$ where ω is the ambient angular velocity and W is the vertical velocity scale given by $W = \sqrt{2 \int_0^h b(0,z) dz}$ and 2) Reynolds number defined as $R_{eF} = \frac{Wh}{\nu}$ where ν is the kinematic viscosity. Similar to the Ward Chamber, experiments different values of Ω for the Fielder chamber have been tested yielding similar results (Fiedler 1998; Nolan and Farrell 1999; Nolan 2005).

Lewellen et al. (1997) (hereafter, LL97) most closely resembles the simulation presented herein. The LES model in LL97 is dynamically driven, with side boundary conditions closely resembling the flow field surrounding a tornado and an updraft at the top boundary to drive flow inward. The LES model is capable of replicating the different vortex flows found in the Ward experiments for varying swirl ratios. LL97 also identifies variables that affect surface layer inflow such as surface roughness length and translational velocity which modify vortex structure. Results from F94 and LL97 are discussed in more detail below.

2.3.3.1 Results from the Fiedler Chamber

As stated previously, the model in F94 consists of closed boundaries with a no-slip lower boundary and the tropopause located at height h. All variables are nondimensionalized with the lower boundary is at $z = 0$ and the upper boundary is at $z = 1$. The outer wall

is set at $r_0 = 2$. The flow is governed by nondimensional, constant density, incompress-ible, axisymmetric Naiver-Stokes equations and the continuity equation. The updraft is thermodynamically forced and is driven by the buoyancy force given by

$$b(r,z) = \begin{cases} .5[1 + cos(2\pi r_b)] & r_b = [r^2 + (z - 0.5)^2]^{1/2} \leq 0.5 \\ \\ 0 & \textit{otherwise} \end{cases} \tag{2.5}$$

giving a nondimensional velocity scale of $W = \sqrt{2\int_0^h b(0,z)dz} = \sqrt{2*0.5} = 1$. Note that $\int_0^h b(0,z)dz = 0.5$ represents the convective available potential energy (CAPE) at the central axis, i.e. a lifted from $z = 0$ would reach accelerate to $w = 1$ at $z = 1$. The Reynolds number is given by $R_{e_F} = 10,000$ near the surface which decreases in the upper half of the domain. The model in F94 verifies results of the Ward Chamber relating to changes in vortex structure with increasing swirl ratio.

F94 runs three separate simulations, increasing from $\Omega = 0.01$ to $\Omega = 0.025$ and finally to $\Omega = 0.08$. For $\Omega = 0.01$, radial velocity is negligible away from the top boundary where flow accumulates and is forced outward by the PGF. The highest tangential and vertical velocities are found far above the surface at $z \approx 0.5$, collocated with a region of lower pressure. Thus, air flows around the boundary region yielding no vortex at the ground, only a central updraft away from the surface similar to Figure 2.2a. For $\Omega = 0.025$, the region of strongest inflow is located just above the surface near the central axis. However, the strongest tangential velocities, vertical velocities, and pressure deficit are still displaced far above the surface far above the region of strong inflow at $z \approx 0.25$. Nevertheless, the magnitude of maximum tangential velocity, vertical velocity, and minimum pressure are
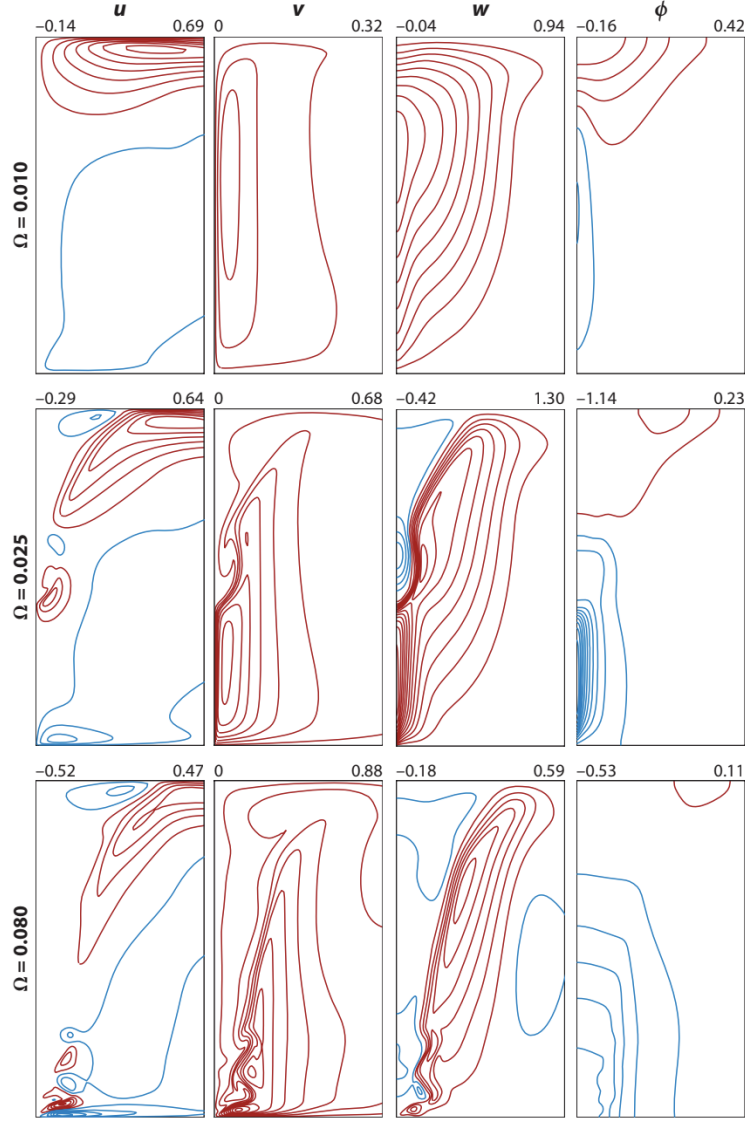
Figure 2.5: Solutions of *u* (radial), *v* (tangential), *w* (vertical), and φ (pressure perturbation) from the Fielder experiments for a swirl ratio of $\Omega = 0.010$ (top row), $\Omega = 0.025$ (middle row), and $\Omega = 0.080$ (bottom row). The contours start at ± 0.05 and are contoured every 0.10 with red contours being positive values and blue contours negative. The domain shown is from $0 \leq r \leq 0.5$ and $0 \leq z \leq 1$. Model specifications are detailed in Fiedler (1994) with image adapted from Rotunno (2013).

larger compared to $\Omega = 0.01$. Additionally, a central downdraft impinges down to $z = 0.5$. The flow structure mirrors Figure 2.2c with strong radial velocities near the surface and strong vertical velocities and the presence of an axial downdraft aloft. The largest swirl ratio, $\Omega = 0.080$, results in a well-defined corner flow region characterized by strong radial inflow near the surface coupled with strong radial coupled just above the inflow. This is collocated with a region of maximum tangential velocities and strong vertical velocities. The central downdraft impinges down to the surface resulting in a two-celled vortex, resembling the vortex in Figure 2.2d-e.

When frictional effects are removed in the F94 model by allowing the lower boundary to be free slip, the structure of the vortex changes (Figure 2.6). Even for large swirl ratios, radial inflow is near-zero close to the surface. The core radius is nearly constant with height and increases with increasing Ω. The region of maximum updraft located in the upper half of the domain. There is relatively low pressure in the lower half of the domain for all and relatively high pressure from forced convergence at the top boundary for all Ω. As expected, the existence of a corner flow region and a strong axial downdraft for larger swirl ratios is dependent on frictional effects and the existence of a boundary layer.

2.3.3.2 Results from the Lewellen LES model

LL97 simulated a vortex using an LES model, focusing on the interaction with the surface by varying surface roughness and translational velocity. Therefore, grid spacing must be sufficient to resolve turbulent eddies that dominate close to the surface. More specifically, the LES grid is stretched with the highest horizontal and vertical resolution is found near the central axis close to the surface, approximately 2.5 m and 1.5 m, respectively. The

30
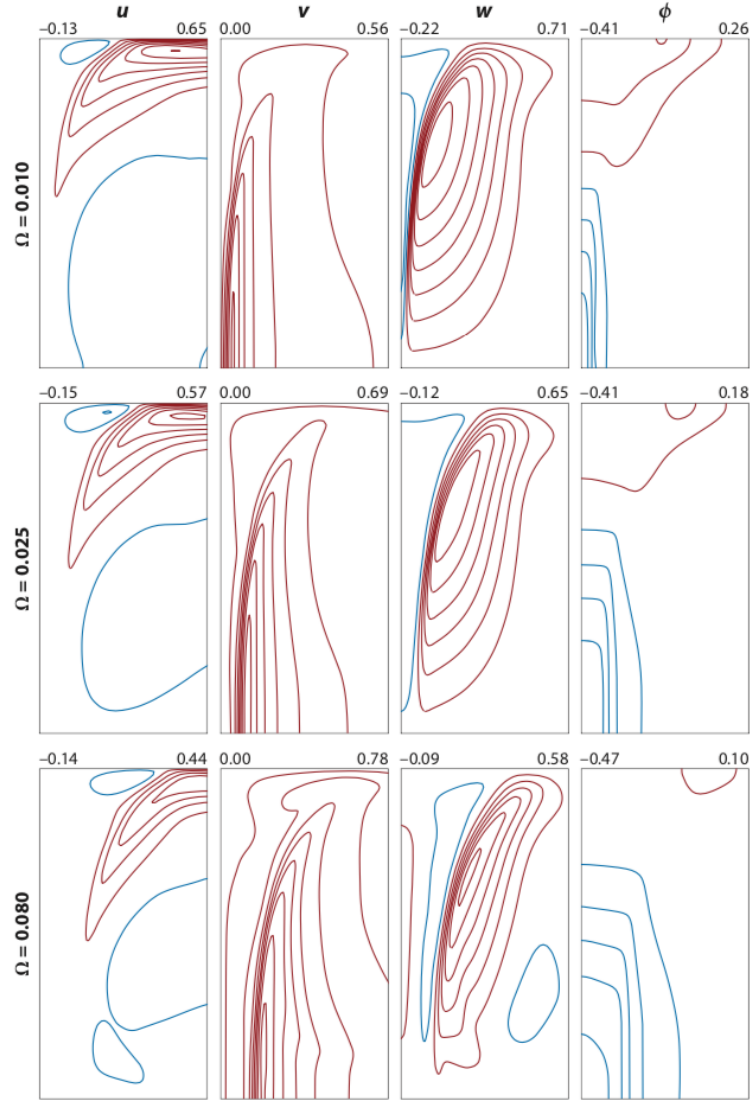
Figure 2.6: Similar to Figure 2.5 but for free slip conditions on the lower boundary. Model from Fiedler (1994), image from Rotunno (2013).

coarsest horizontal and vertical resolution is 50 m and 100 m, found closest to the side and top boundaries. The size of the domain is 1 km × 1 km × 2 km.

Because the domain is not large enough to capture the parent thunderstorm, the boundary conditions emulate the environment of a parent thunderstorm around the tornado. Therefore, the objective of LL97 is not to address tornadogenesis, but rather how larger-scale features defined by the boundary conditions affect the structure and dynamics of the tornado, especially pertaining to low-level flow. From the top of the surface layer (200 m) up to 1 km, the horizontal boundary conditions are characterized by a constant circulation $2\pi\Gamma = 2\pi vr$ with $\Gamma = 10^4$ m^2 s^{-2} and a constant radial inflow $2\pi Q = 2\pi ur$ where $Q = 8/3 \times 10^3$ m^2 s^{-1}. Above 1 km, the radial component of flow is set to zero. The swirl ratio $S = \frac{\Gamma r_0}{2Qh} = 0.94$, a moderate value. The lower boundary translates at -15 m s^{-1} to simulate the tornado moving forward, i.e. everything is conducted within the tornado's frame of reference. In the surface layer (0 to 200 m AGL), the tangential velocity varies proportional to $ln(z/z_0)$, where z_0 is the surface roughness length, equal to 0.2 m in LL97. Frictional effects increase for a larger z_0 (Stull 1988), with Table 2.2 giving physical terrain examples for given z_0 values. The radial velocity profile follows a modified logarithmic distribution with maximum inflow occurring at 30 m AGL. On the top boundary, a disk with a diameter of 1 km of positive vertical velocities (updraft) of 21.9 m s^{-1} is enforced. Although observed flow are unlikely to be axisymmetric, the boundary conditions represent reasonable values for an observed mesocyclone

The largest time-averaged pressure deficit in LL97 is found at $\sim$30 m AGL, 75% lower than the pressure found in the upper core region. There is an axial downdraft from the surface up to 1 km AGL, with a minimum vertical velocity of -30 m s^{-1}. The axial downdraft

Table 2.2: Varying values of surface roughness length and corresponding representative terrain features.

Roughness Length, z_0 (m)	Terrain Description
0.001	Very smooth, e.g., calm ocean
0.01	Rough pasture
0.1	Field with sparse trees
1.0	Suburb / Forest

forces the strongest updrafts in an annulus shape, whose radius remains quasi-constant through the upper core region, where flow is in cyclostrophic balance. The maximum tangential velocity in the upper core region is $\sim$55 m s^{-1}, which occurs at a core radius of 150 m.

Closer to the surface, frictional effects cause a disruption in cyclostrophic balance and a decrease of the core radius. Maximum tangential velocities are stronger, $\sim$85 m s^{-1} compared to 55 m s^{-1} in the upper core region, located at $R \approx 50$ m and $Z \approx 30$ m. Surface interactions and balances in angular momentum discussed previously lead to tangential velocities that well exceed that of the thermodynamic speed limit (Fiedler and Rotunno 1986; Fiedler 1994), calculated to be 67 m s^{-1} in LL97. The structure of the corner flow and boundary layer region is asymmetric, with higher (lower) tangential velocities on the right (left) side of the tornado with respect to the direction of translation. LL97 also notes a tilting and twisting of the vortex at lower levels, attributed to effects from forward movement.

The vortex in LL97 also has relatively high values of $TKE = \sqrt{\frac{2}{3}(u'^2 + v'^2 + w'^2)}$ where the prime denotes departure from time-averaged values. High values of TKE, especially in the corner flow region, indicate that the instantaneous flow structure of the tornado differs greatly from the time-averaged structure. LL97 finds there are smaller updrafts rotating

around the central axis, a product of secondary vortices located at the interface between the main updraft and downdraft regions of the vortex. These secondary vortices are revealed to be quite complex in structure, twisting significantly with height. The behavior of the subvortices are erratic, constantly disappearing and reforming as they rotate about the center.

LL97 repeats the simulation, changing the translational velocity to $0 \ \mathrm{m\,s^{-1}}$. The structure of the upper core region remains relatively unaltered when translational velocity is set to $0 \ \mathrm{m\,s^{-1}}$, which is expected since surface interactions in the upper core region are small. Closer to the surface, the strongest velocities in the corner flow region are reduced, with mean maximum velocity decreasing by $\sim 5 \ \mathrm{m\,s^{-1}}$. LL97 hypothesizes that for the non-translating tornado, horizontal vorticity generated by forward translation of the tornado is no longer plays a role, resulting in reduced generation of vertical vorticity by tilting. Additionally, the average maximum pressure deficit decreases by 30% and maximum *TKE* values decrease by 25%.

Chapter 3

Methodology

3.1   LES Model Specifications

The LES model utilized in this study is based on the model developed at the Research Institute for Applied Mechanics Computational Prediction of Airflow over Complex Terrain (RIAM-COMPACT) (Uchida and Ohya 2003; Maruyama 2011) at Kyushu University. The background vortex in the LES is of a moderate swirl ratio. The model domain is on a stretched mesh grid with specifications given in Table 3.1. Model output is every 1.2 s.

Table 3.1: Specifications of the LES model including domain size, number of grid points, and minimum and maximum resolution

Direction	x	y	z
Domain Size (km)	1	1	2
Grid Points	156	156	140
Minimum Spacing (m)	3.6	3.6	2.5
Maximum Spacing (m)	17.3	17.3	75.2

The flow within the LES is split into a grid-scale (GS) and subgrid-scale (SGS) through a filtering technique. The filtered continuity and Navier-Stokes equations on the GS (Maruyama 2011) are given by

$$\frac{\partial \bar{u}_i}{\partial x_i} = 0, \quad i = 1,2,3 \tag{3.1}$$

$$\frac{\partial \bar{u}_i}{\partial t} + \frac{\partial \bar{u}_i \bar{u}_j}{\partial x_j} = -\frac{1}{\rho}\frac{\partial \bar{p}}{\partial x_i} + \frac{\partial 2\nu_e \bar{S}_{ij}}{\partial x_j} + F_i, \quad i,j = 1,2,3 \tag{3.2}$$

where x_1, x_2, and x_3 are the x, y, and z directions and u_1, u_2, and u_3 are the filtered wind components in the respective directions. The F_i term appended onto the end represents the feedback force from the immersed boundary method discussed in Section 3.2 which forces ground-relative flow at the boundary to zero. Additionally, ρ is air density, $\bar{p}$ is filtered pressure, and $\bar{S}_{ij}$ is the filtered deformation term or strain rate tensor given by

$$\bar{S}_{ij} = \frac{1}{2}\left(\frac{\partial u_i}{\partial x_j} + \frac{\partial u_j}{\partial x_i}\right) \tag{3.3}$$

The unresolved SGS in Equation 3.2 appears in the eddy viscosity term, ν_e, which is the summation of the viscosity on the GS and the SGS viscosity given by

$$\nu_{SGS} = |\bar{S}|(C_S L)^2 \tag{3.4}$$

where based on the Smagorinsky turbulence model (Smagorinsky 1963), $C_S = 0.1$ except near the lateral boundaries where C_S is multiplied by an exponential wall-damping function. In equation 3.4,

$$|\bar{S}| = \sqrt{2\bar{S}_{ij}\bar{S}_{ij}} \tag{3.5}$$

$$\Delta = (\Delta x_1 \Delta x_2 \Delta x_3)^{1/3} \tag{3.6}$$

where Δ is also known as the filter width. The governing equations are approximated by a finite difference method. Spatial derivatives are approximated using a second-order centered difference scheme and an Adams-Bashforth scheme is implemented to advance temporally. Numerical integration calculations for mass flux and pressure coupling are handled using the fractional step method.

The simulations are split into two parts: the spin-up period and the analysis period. The spin-up period allows the vortex to reach a quasi-steady state before introducing terrain and lasts 915 s. During the spin-up period, the LES imposes a wall log model (Bodine et al. 2016) with a surface roughness of $z_0 = 0.001$ m, with surface stress on the first grid point given by

$$\tau = \rho u_*^2 \tag{3.7}$$

where u_* is the friction velocity given by

$$u_* = \frac{V_H(z_1)\kappa}{log(\frac{z_1}{z_0})} \tag{3.8}$$

with V_H being the horizontal wind speed and κ being the Kármán constant. During the analysis period lasting 510 s, terrain is introduced and the lower and lateral boundaries are free-slip, though friction is implicitly defined when forcing flow at the terrain boundary to zero through the immersed boundary method.

The LES simulations impose a translational velocity of the vortex by moving the bottom boundary in the negative x direction at a specified speed, 10 m s^{-1} for most simulations. On the lateral boundaries, from the surface up to an inflow depth of $h_{inf} = 200$ m, the flow is axisymmetric with a constant mass flux inward and constant angular momentum. Above h_{inf}, the radial velocities are fixed at 0 m s^{-1} and angular momentum is also held constant. The upper boundary condition induces vertical velocities which vary as a function of range,

$$w(r) = \begin{cases} 44.8\frac{r}{0.4l_{dom}} - 20 & r \leq 0.4l_{dom} \\ 24.8 & r > 0.4l_{dom} \end{cases} \tag{3.9}$$

3.2 Implementation of Terrain

To implement terrain into the LES model, an immersed boundary method (IBM) was used which was developed and tested by Goldstein et al. (1993); Saiki and Biringen (1996). The IBM modifies the Navier-Stokes equations such that all velocity components at the specified terrain height is forced to equal the translation velocity by imposing a boundary force term. Both the IBM and the respective equations each type of introduced terrain are discussed more below in Sections 3.2.1 and 3.2.2. It is important to note that the terrain features implemented into the model for this study are relatively subtle, and could be found in flat regions such as Oklahoma.

3.2.1 Immersed Boundary Methods

The IBM introduces a feedback function appended to the momentum equations (Equation 3.2) along the terrain grid points that bring the fluid velocity equal to zero in a ground-relative sense. Additionally, a "terrain grid" is defined with a higher resolution than the LES grid (1000×1000 grid points) such that possible sharp changes in the terrain feature can be adequately represented and transitions as the terrain translates across the model domain are smooth. The feedback force imposed on the terrain grid points, $\mathbf{x}_s$, can be represented mathematically as

$$F_i(\mathbf{x}_s, t) = \alpha \int_0^t (U_i(\mathbf{x}_s, t) - v_i(\mathbf{x}_s, t)) \, dt + \beta (U_i(\mathbf{x}_s, t) - v_i(\mathbf{x}_s, t)) \qquad (3.10)$$

where **U** is the fluid velocity and **v** is the velocity of the boundary itself, equal to the negative of the tornado translational velocity. The coefficients α and β are dampening coefficients. The values of α and β suppress the numerical oscillations produced by the addition of the feedback function observed in the Chebyshev spectral method in Goldstein et al. (1993). In Saiki and Biringen (1996), α is chosen to be -4000 and β is chosen to be -60. After a range of larger and smaller values were tested, it was found that the best convergence and stability occurred for similar values, thus these same values are used in the present study. Fluid velocities computed on the LES grid must be interpolated to the terrain grid and then the boundary force calculated on the terrain grid must be interpolated back to the LES grid. The former is represented by the equation

$$\mathbf{U}(\mathbf{x}_s) = \sum_{i,j}^{i+1,j+1} D_{i,j}(\mathbf{x}_s)\mathbf{U}_{i,j} \qquad (3.11)$$

while the latter is represented mathematically by

$$\mathbf{F}_{i,j} = \frac{1}{N_b} \sum_{n=1}^{N_b} D_{i,j}(\mathbf{x}_s)\,\mathbf{F}_n(\mathbf{x}_s) \qquad (3.12)$$

where N_b is the number of terrain grid points that affect the (i,j)th LES grid point. In Equations 3.11 and 3.12,

$$D_{i,j} = d(x_s - x_i)d(y_s - y_i) \qquad (3.13)$$

where

$$d(x_s - x_i) = \begin{cases} (x_s - x_{i+1})/(x_i - x_{i+1}) & x_i < x_s \\ \\ (x_s - x_{i-1})/(x_i - x_{i-1}) & x_i > x_s \\ \\ 1 & x_i = x_s \end{cases} \qquad (3.14)$$

Though first order accuracy of Equations 3.11 and 3.12 cause the flow field in the very near vicinity of the boundary to contain inaccuracies, the larger-scale flow is sufficiently captured for the purposes of the LES model.

3.2.2 Terrain Equations

All simulations presented in this study can be split amongst four categories: a 3D hill (hereafter, hill), a 2D / sinusoidal hill (sinusoid), a valley, or a ridge (Table 3.2), with the 50 m base simulation terrain contours shown in Figure 3.2. For each simulation, the terrain enters from the right side of the domain. For each grid point x_{gp} and time, there is a check to see if that grid point has not passed an x value of one domain length (x $\approx$ 1000 m),

$$x_{gp} = x_t(i, j) + x_{pos} - X_0 \leq \lambda_x \qquad (3.15)$$

where $x_t(i, j)$ is the x-position of the grid point relative to the center of the domain, X_0 is the initial x-position of the left side of the domain at $t = 0$, λ_x is one domain's length, and x_{pos} is the x-position of the center of the domain relative to its starting point at $t = 0$ (i.e., the total distance translated) given by

$$x_{pos} = -v_{trans} * n_{STP} * \Delta t \qquad (3.16)$$

Table 3.2: All simulations that are used for analysis in this chapter sorted by terrain category. The second term "Xm" refers to the maximum height / depth of the hill or ridge / valley. The last term refers to any changes made from the base simulation of that particular terrain category. "Base" for the hill and sinusoid categories = repetition of the hill every 1 domain length. For the 3D hill the maximum height of each hill must also be located at y = 0 m. "Base" for the valley / ridge = maximum depth / height of the terrain being located at exactly y = 0 m. Variations to the base state are as follows: "vX" = tornado translation speed is changed to X m s^{-1}, "steepX" = hill is steeper in the x-direction, with "steep2" being steeper than "steep1", "offsetX" = center of hill is offset to the north at y = X m, "spread" = hill repeats every 2 domain lengths as opposed to 1, "snakeX" = valley or ridge oscillates in the direction of translation with a wavelength of 1 domain length and an amplitude of X m, "curve" = maximum depth of valley curves off out of the domain about halfway through the simulation.

Hill Set	Sinusoid Set	Valley Set	Ridge Set
hill_25m_base	sinusoid_10m_base	valley_50m_base	ridge_50m_base
50m_base	25m_base	100m_base	100m_base
100m_base	50m_base	50m_snake50	50m_snake100
150m_base	100m_base	50m_snake100	100m_snake100
200m_base	-	50m_snake200	-
50m_v5	-	100m_snake100	-
50m_v20	-	50m_curve	-
50m_steep1	-	100m_curve	-
50m_steep2	-	-	-
50m_offset100	-	-	-
50m_offset200	-	-	-
50m_spread	-	-	-
100m_spread	-	-	-
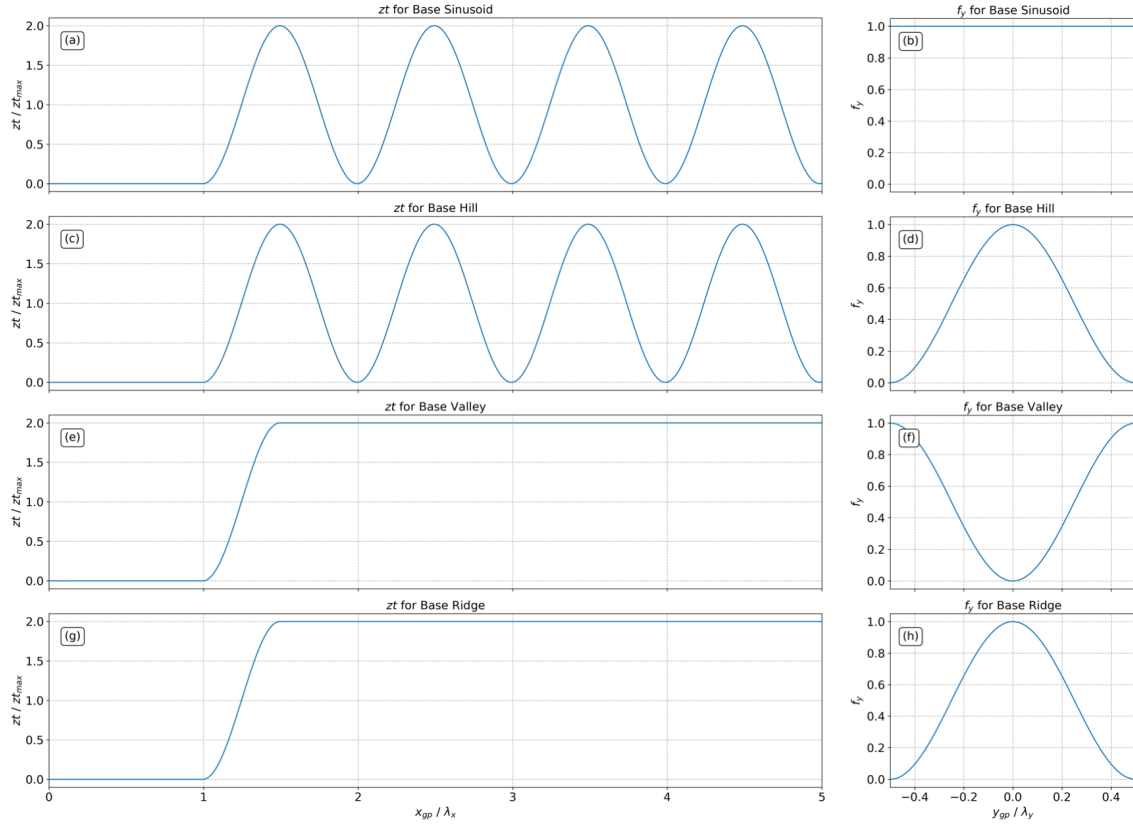
Figure 3.1: Functions of *zt* and f_y for base simulations of the sinusoid (a-b), hill (c-d), valley (e-f), and ridge (g-h) set.

In Equation 3.16, v_{trans} is the translational velocity in $m\,s^{-1}$, n_{STP} is the number time step of the model, and Δt is the model time step increment. If Equation 3.15 holds true, then the terrain height is set to 0 m.

Once x_{gp} exceeds one domain length, the terrain in each category is given by *zt*. For the base sinusoid simulations,

$$zt(i,j) = zt_{max} * sin(\frac{2\pi(xt(i.j) + x_{pos} - X_0)}{\lambda_x} - \frac{\pi}{2}) + zt_{max} \qquad (3.17)$$

where zt_{max} is added at the end of the function to prevent negative values of height, giving a maximum terrain height of $2 * zt_{max}$ (Figure 3.1a). The base hill also uses Equation 3.17
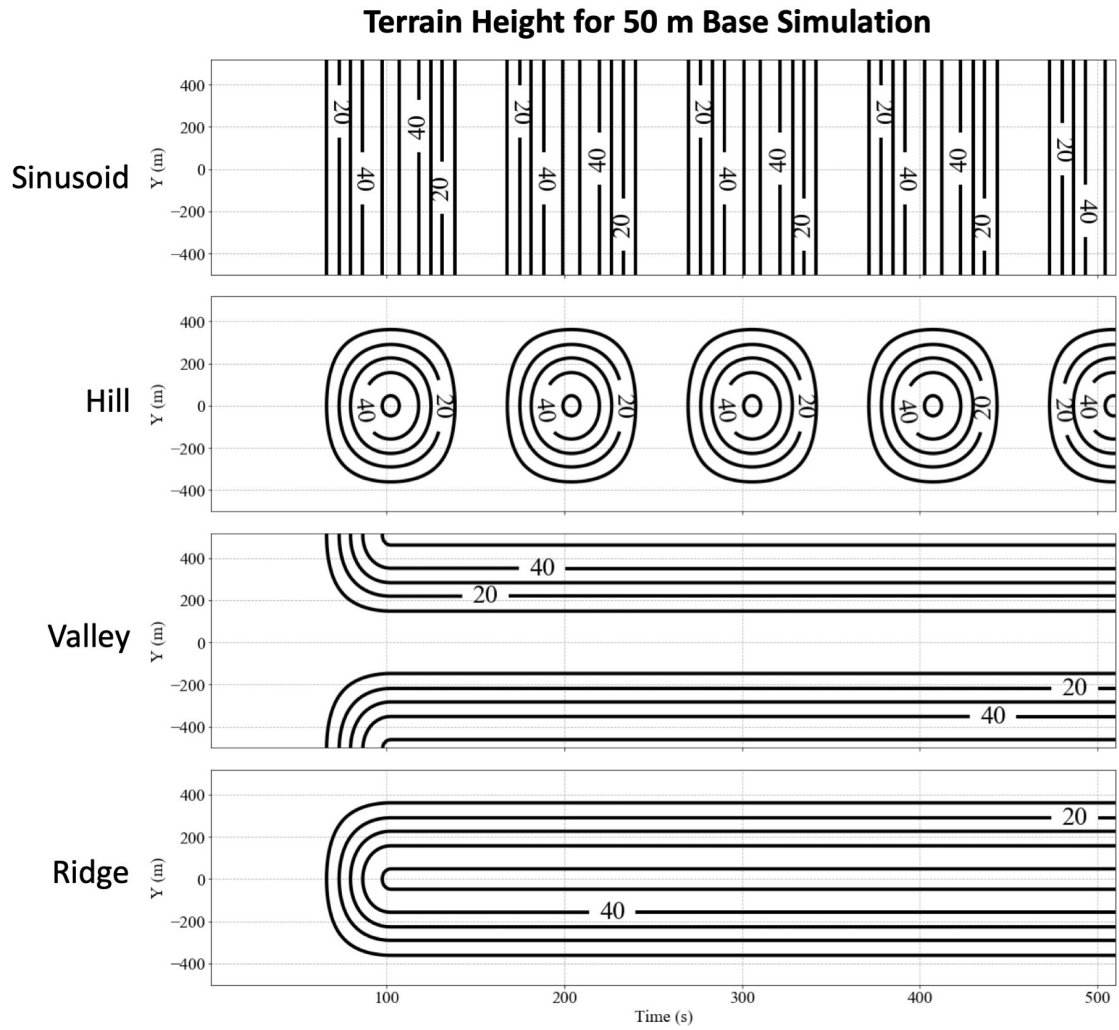
Figure 3.2: Terrain height for the 50 m base simulation along the path of the tornado for each of the four terrain categories.

(Figure 3.1c), multiplied by another function f_y which allows for terrain variation in the y-direction (Figure 3.1d):

$$f_y(i,j) = \frac{1}{2}sin(\frac{2\pi(yt(i,j))}{\lambda_y} + \frac{\pi}{2}) + \frac{1}{2} \tag{3.18}$$

where λ_y is the domain length in the y-direction (same as λ_x since the domain is square). For both valley and ridge sets (Figure 3.1), if $\lambda_x < x_{gp} \leq 1.5 * \lambda_x$, then the tornado ascends onto / enters into the ridge / valley with zt given by Equation 3.17. When $x_{gp} > 1.5 * \lambda_x$,

$$zt(i,j) = 2 * zt_{max} \tag{3.19}$$

so terrain no longer varies in the x-direction. For the valley set, zt is multiplied by

$$f_y(i,j) = \frac{1}{2}sin(\frac{2\pi(yt(i,j))}{\lambda_y} - \frac{\pi}{2}) + \frac{1}{2} \tag{3.20}$$

(Figure 3.1f; same as Equation 3.18 except for a sign flip before the last term in the sin function). For the ridge set, f_y is the same as Equation 3.18 (Figure 3.1h).

Modifications to the equations for non-base cases in Table 3.2 are discussed below. For hill_50m_steep1, which steepens the hill in the x-direction,

$$zt(i,j) = (zt_{max} * sin(\frac{2\pi(xt(i.j) + x_{pos} - X_0)}{\lambda_x} - \frac{\pi}{2}) + zt_{max})^2 * \frac{1}{20} \tag{3.21}$$

For hill_50m_steep2 which is even steeper, Equation 3.21 is cubed rather than squared and multiplied by $\frac{1}{400}$. For the offset hill case, a shift must be added into the function f_y so the

function is not centered at y = 0. A shift of X m in the positive y direction is represented mathematically by

$$f_y(i,j) = \frac{1}{2}sin(\frac{2\pi(yt(i,j) - X/1000)}{\lambda_y} - \frac{\pi}{2}) + \frac{1}{2} \qquad (3.22)$$

The last adjustment for the hill set is the spread cases, in which there is a large distance between adjacent hills. In this case, the equations alternate between $zt = 0$ and Equation 3.17, still multiplied by f_y given by Equation 3.18. This results in the removal of every other hill from the base hill simulations.

For the ridge and valley set, there are simulations in which the terrain feature oscillates (snakes) in the direction of translation, thus f_y must a function of both x and y. As with Equation 3.22, a shift to f_y is introduced except that X is replaced another function f_{shift}, which is a function of x. The magnitude of the "snaking" of the valley is given by the amplitude in f_{shift}. For an oscillation of amplitude X m (center of valley goes from -X m to X m) is given by

$$f_y(i,j) = \frac{1}{2}sin(\frac{2\pi(yt(i,j) - f_{shift}(i,j))}{\lambda_y} - \frac{\pi}{2}) + \frac{1}{2} \qquad (3.23)$$

where

$$f_{shift}(i,j) = \frac{X}{1000}sin(\frac{2\pi(xt(i,j) + x_{pos} - X_0)}{\lambda_x}) \qquad (3.24)$$

The last adjustment is a curved, which starts as a base valley that curves out of the domain about halfway into the simulation. The goal is to compare this simulation to the 13 April 2018a Mountainburg, AR tornado which tracked along a valley which then took a

northward curve, resulting in a $\sim$200-m elevation gain and subsequent weakening of the tornado. Before then curve at $x_{gp} < 2.5 * \lambda_x$, the equations remain the same as the base valley. The northward curve of the valley occurs at $2.5 * \lambda_x \leq x_{gp} < 4.5 * \lambda_x$, where f_y is given by Equation 3.23 with

$$f_{shift}(i,j) = 0.5 sin(\frac{2\pi(xt(i,j) + x_{pos} - X_0)}{\lambda_x} + \frac{\pi}{4}) + 0.5 \qquad (3.25)$$

Chapter 4

Case Studies

In this section, specific simulations from the hill, sinusoid, and valley set are chosen to convey detailed findings within each category. The chosen simulations are as follows:

- **Hill**: hill_25m_base (hereafter H25), hill_50m_base (H50), hill_100m_base (H100), hill_50m_v20 (H50V) and hill_50m_steep2 (H50S).

- **Sinusoid**: sinusoid_10m_base (S10), sinusoid_25m_base (S25), sinusoid_50m_base (S50), and sinusoid_100m_base (S100).

- **Valley**: valley_50m_base (V50), valley_100m_base (V100), valley_100m_snake100 (V100S), and valley_100m_curve (V100C).

The simulations from each set are chosen because the tornado displays notable behavior in each of the simulations. Differences between simulations in a terrain set give insight on how tornado behavior changes with slightly modified terrain.

4.1   Hill Set

The five simulations chosen to represent the hill set are H25, H50, H100, H50V, and H50S. Differences between H25, H50, and H100 provide insight on if increasing terrain height leads to a larger disruption of the vortex. H50V addresses if the speed at which a vortex translates over terrain leads to any significant changes and H50S will seek to address

47
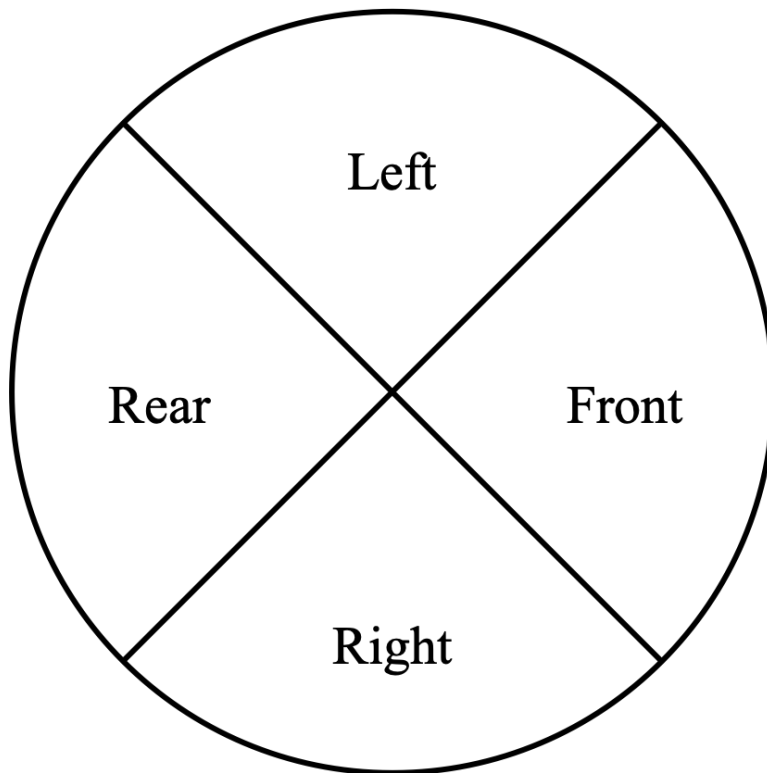
Figure 4.1: The locations of the right, left, front, and rear quadrant of the tornado.
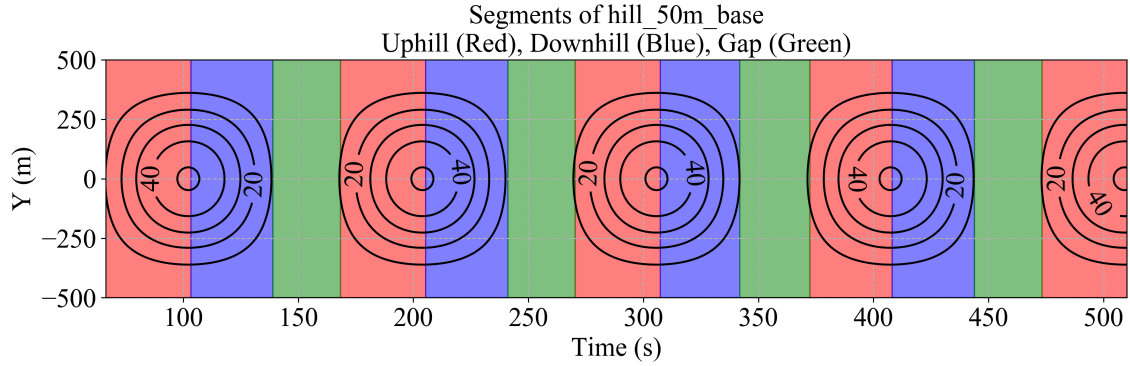
Figure 4.2: Example segmentation of the hill_50m_base simulation. The red represents the uphill segment, blue for the downhill segment, and green for the gap segment.

whether a steeper hill equates to increased terrain influence. In the analysis, the tornado is split into four quadrants: the right, left, front, and rear quadrant (Figure 4.1). Additionally, the terrain in each of the simulations is also split into three different segments dependent on the location of the tornado relative to the terrain: 1) the uphill segment where terrain height is increasing in the direction of translation and is greater than 10 m, 2) the downhill segment where terrain height is decreasing in the direction of translation and is greater than 10 m and 3) the gap segment located in between the downhill and uphill segments when the terrain height is less than 10 m (Figure 4.2). Each of the simulations encounters five total hills during the entirety of the simulation (510 s) except for H50V which encounters ten due to an increase of the translation speed by a factor of two. Lastly, horizontal wind is abbreviated as *uv* and vertical wind is *w*.
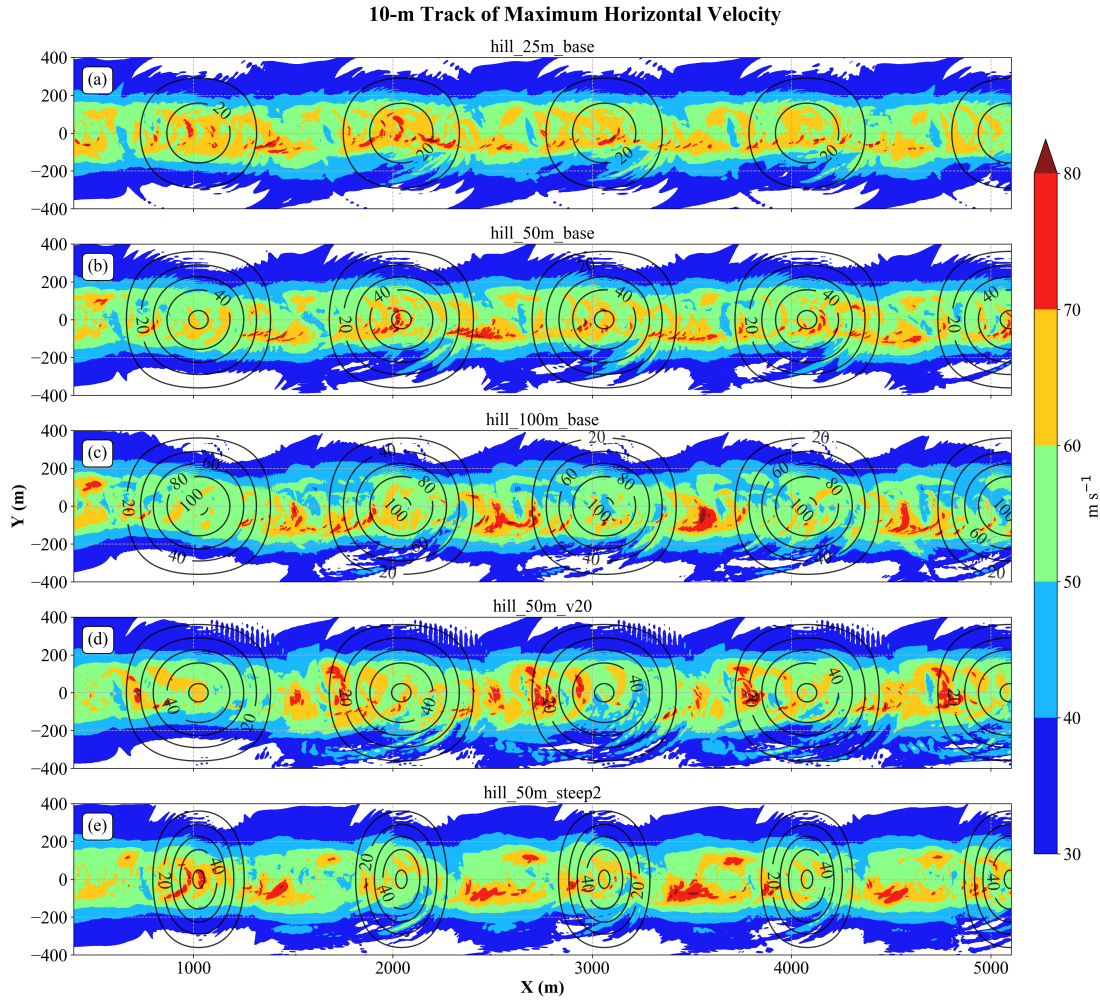
Figure 4.3: The maximum 10 m AGL horizontal winds through the entirety of the tornado track for a) H25, b) H50, c) H100, d) H50V, and e) H50S. The terrain height is contoured in black.
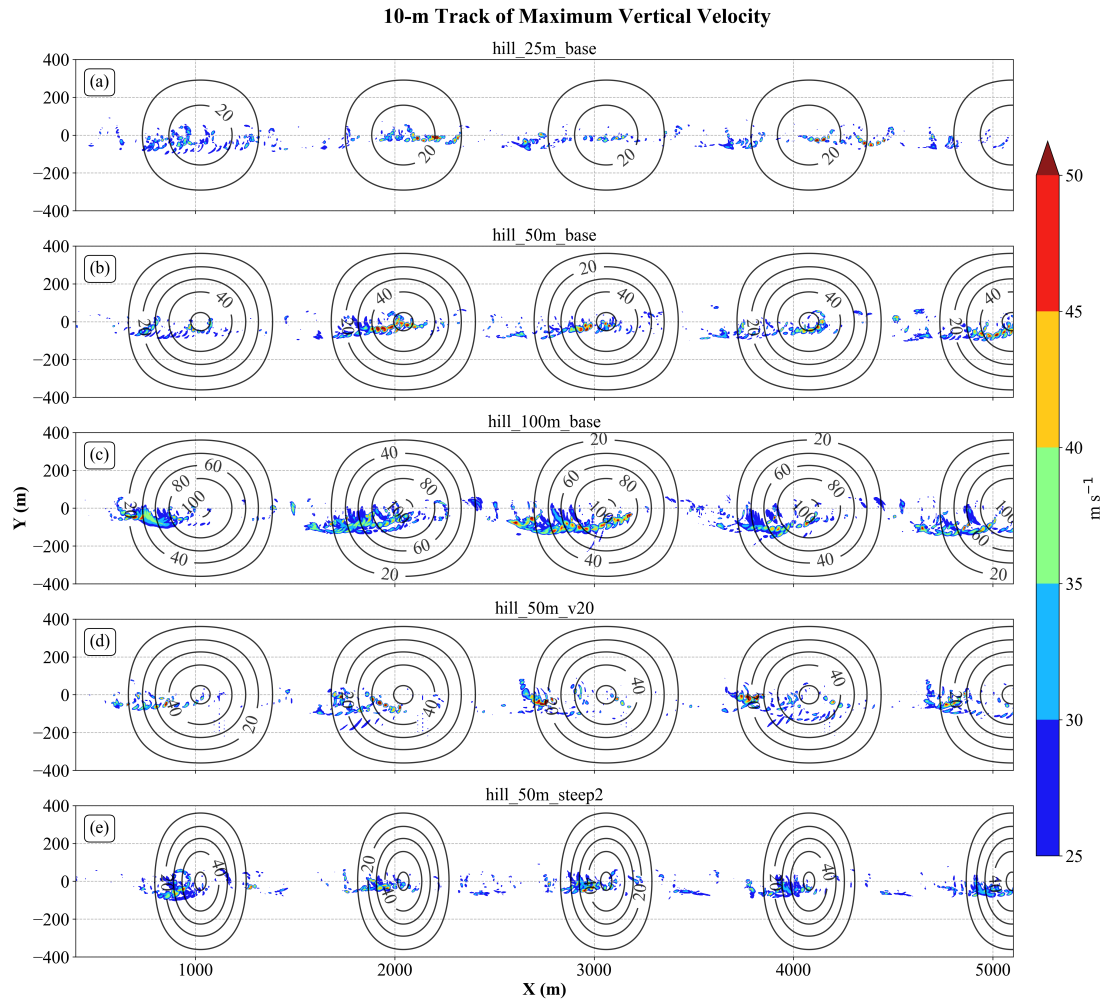
Figure 4.4: The maximum 10 m AGL vertical winds through the entirety of the tornado track for a) H25, b) H50, c) H100, d) H50V, and e) H50S. The terrain height is contoured in black.

4.1.1 10-m Track

The maximum horizontal and vertical wind speed for each grid point along the track for the entire simulation is plotted in Figures 4.3 and 4.4, hereafter maxUV and maxW, respectively. The first location where maxUV is enhanced for H50 (Figure 4.3) occurs at the end of the downhill and the first half of the gap segment. This area of enhanced maxUV is especially noticeable after the second hill and occurs where y < 0. Further analysis reveals that enhanced horizontal wind speeds in this area is the result of two distinct swaths of stronger winds. The first swath originates from enhanced downslope winds mostly in the right quadrant with consistent $uv > 70 \text{ m s}^{-1}$. The second swath is located in the front quadrant further and seems to be a result of convergence as flow from the south is constricted between the two hills (hereafter referred to as flow channeling). The winds from flow channeling is weaker than the enhanced downslope winds for H50.

The two swaths of enhanced uv are separated by a ribbon of weak uv that penetrates all the way to the in the center of the tornado. This ribbon is a defining feature in all hill simulations. When the tornado is on the downhill segment, flow in the left quadrant must battle upslope terrain and encounters enhanced friction and a larger depletion in M. Thus, as the parcels rotate around to the rear and right quadrant, the parcels tend to spiral inwards. This allows for the entrainment of air from the top of the hill whose uv has been slowed from maximized frictional effects. Additionally, the depth of the layer that has been frictionally modified is maximized when entraining air from the top of the hill, leading to the ribbon of reduced uv that appears on the downhill segment. Both swaths of enhanced uv and the entrainment of a ribbon of lower uv are illustrated in Figure 4.5.
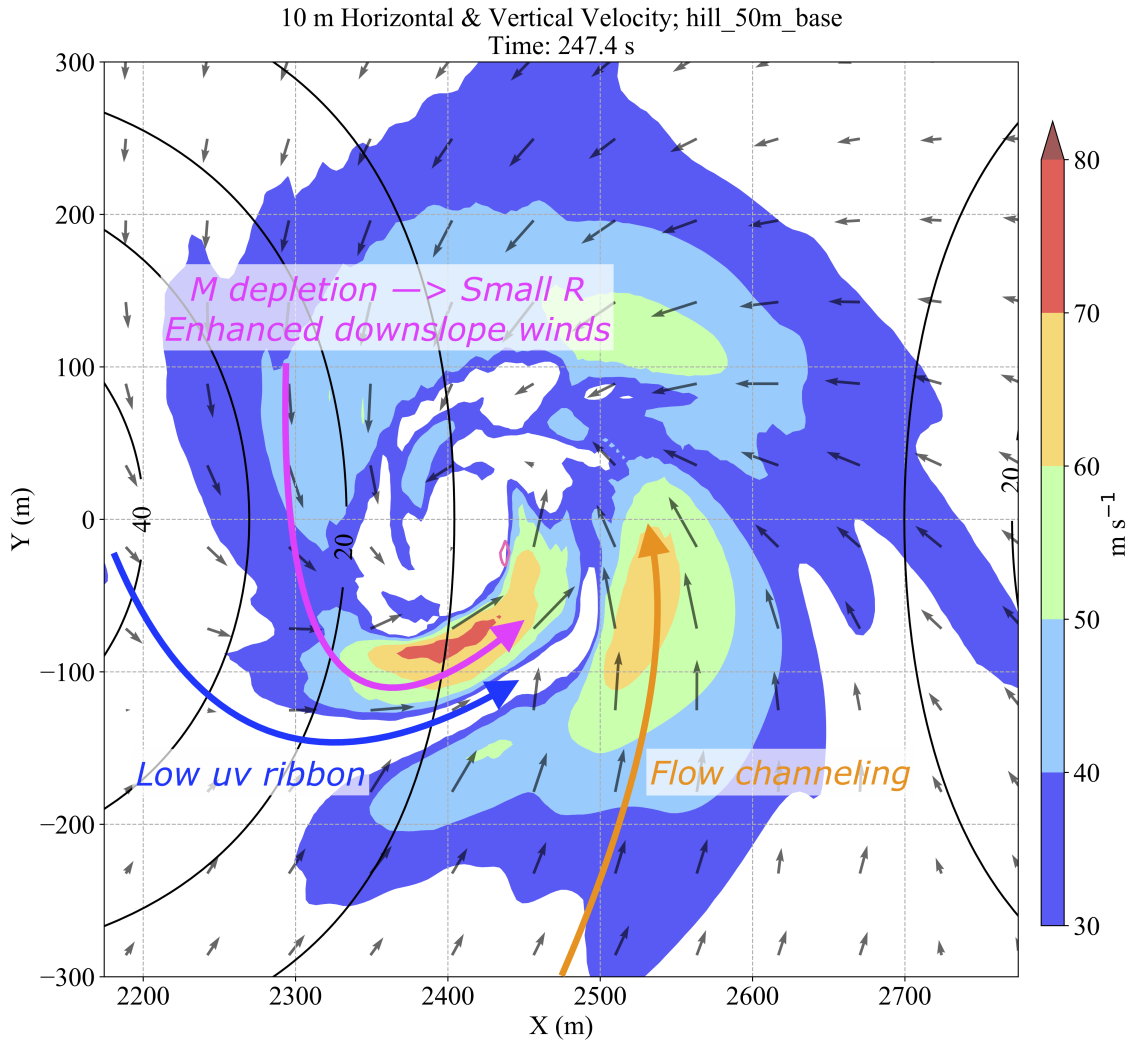
Figure 4.5: Snapshot of 10 m horizontal winds (arrows, shaded contour) as well as vertical velocity $> 20 \text{ m s}^{-1}$ (pink contour) at 247.4 s. The annotations highlight key features in the 10-m AGL winds: 1) enhanced horizontal winds from downslope and flow channeling and 2) enhanced friction on the upslope resulting in parcels rotating inward and allowing for the entrainment of low uv fluid from the top of the hill.

The second area of enhanced maxUV occurs on the uphill and is again most prominent on the second hill. This region of stronger maxUV appears discontinuous and occurs in conjunction with the strongest maxW (Figure 4.4b) and is the result of a series of strong, dominant subvortices develop and intensify as the tornado ascends the hill. These subvortices form in the rear and right quadrant of the tornado, and rapidly dissipate in the front quadrant. Some subvortices are extremely robust, with $uv > 80 \mathrm{\,m\,s^{-1}}$ and $w > 50 \mathrm{\,m\,s^{-1}}$ at 10 m AGL. It is worthwhile to note that while horizontal wind speeds of $> 80 \mathrm{\,m\,s^{-1}}$ correspond to higher-end EF-4, the relative size, quick translational speed, and short duration of the intense subvortices would result in 3-second wind gust to be much lower than the instantaneous wind speed.

The terrain in the hill set is clearly influencing subvortex behavior, with stronger subvortices on the uphill segment. A hypothesis for subvortex formation is presented. When the tornado is on the uphill segment, there is an enhancement of downslope winds in the left quadrant that meet northerly winds in the rear quadrant, leading to enhanced convergence in this area. From mass continuity, strong areas of convergence result in strong vertical velocities. Additionally, the strong w is collocated with strong radial shears of tangential velocity between the center of the tornado and the core radius, i.e. a region of enhanced pre-existing positive vertical vorticity (Figure 4.6a). Strong w stretches pre-existing vertical vorticity until a subvortex forms in the rear quadrant and translates cyclonically around the tornado (Figure 4.6b).

The dissipation of the subvortices as it crosses into the front quadrant is due to the failure of the subvortices remain in a favorable location. Because the subvortex must traverse up the terrain as it rotates around the rear and right quadrant, parcels encounter an enhanced

depletion of M. Thus, subvortices tend to rotate inwards, displacing themselves from areas of strongest radial shears of tangential velocity / enhanced vertical vorticity (Figure 4.6c). Without large gradients in tangential and vertical velocities to aid in maintanence, the subvortex terminates quickly (Figure 4.6d). In some instances, the dissipation is abrupt with uv within the subvortex decreasing from 90 m s^{-1} to about 60 m s^{-1} in 1.2 s (one time step). Subvortices that are able to maintain their initial radius have a longer duration and rotate around to the front and left quadrant without termination. Subvortices have a longer duration at the end of the uphill segment since upslope terrain no longer plays a role, evident by the increased northward extent of large maxUV (see the second, fourth, and fifth hills especially in Figure 4.3b).

When decreasing the hill size by a factor of two (H25), the two swaths of enhanced uv and the ribbon of low uv on the downhill are still evident. However, both enhanced uv swaths are weaker in H25 than in H50, especially the downslope swath. Additionally, the behavior of the subvortices in H25 differ compared to H50; although the most robust subvortices still occur in the right quadrant, the subvortices frequently rotate into the front / left quadrant without dissipating, even on the uphill (first and second hills, Figure 4.3a). The strongest maxW throughout H25 are associated with subvortices that occur on the downhill of the second and fourth hills (Figure 4.4a). The terrain in H25 is small enough that dynamically, there is lesser reason for the most robust subvortices to occur exclusively on the uphill segment; H25 has less downslope flow in the left quadrant on the uphill segment, leading to less convergence in the rear quadrant and reduced stretching of vertical vorticity. Additionally, less steep results in less depletion of M as subvortices traverse upslope, allowing subvortices to maintain their initial radius.
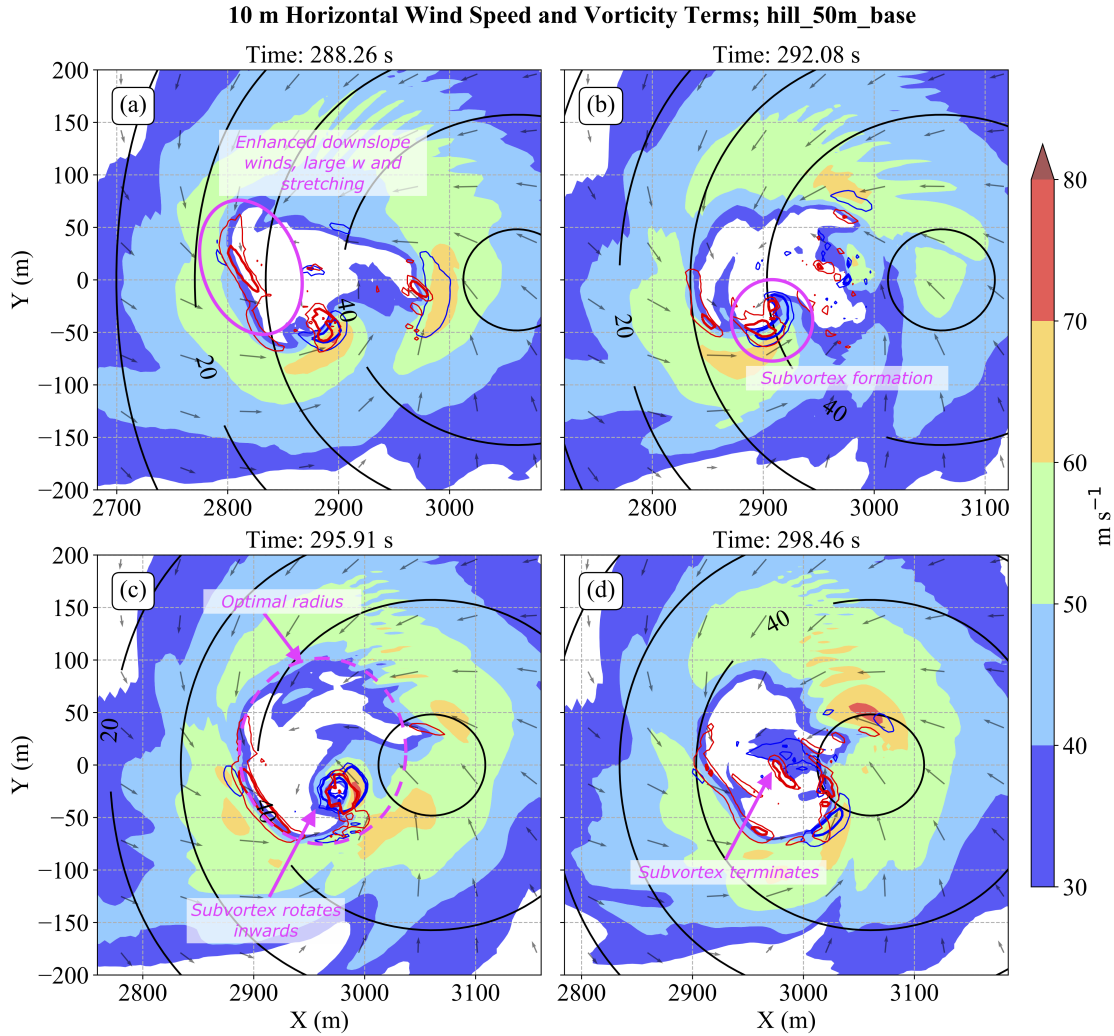
Figure 4.6: Annotated figure illustrating the hypothesis for subvortex formation due to stretching of vertical vorticity from convergence with downslope winds. The shaded contours are correspond to *uv* with arrows showing wind direction. Thin and thick red (blue) contours correspond to positive tendency of vertical vorticity from stretching (tilting) > 2 and $> 5 \text{ s}^{-2}$, respectively.

H100 has similar regions of enhanced maxUV as H50. The enhanced maxUV at the end of the downhill and in the gap segment is still resultant from strong downslope winds and flow channeling. However, decreasing spacing between hills leading to more constricted flow results in a more pronounced flow channeling in H100, with uv commonly $> 70\,\mathrm{m\,s^{-1}}$ and occasionally $> 80\,\mathrm{m\,s^{-1}}$. As a result, the areas of maxUV $> 70\,\mathrm{m\,s^{-1}}$ in H100 extend further north (Figure 4.3c) . Similar to H50, robust subvortices in H100 form in the rear quadrant on the uphill segment, strengthen, and dissipate in the front quadrant. These subvortices are apparent as broken enhanced regions of maxUV and maxW on the uphill segment (Figure 4.3c and 4.4c). The uphill segment also contains a larger, more consistent area of maxW $> 25\,\mathrm{m\,s^{-1}}$ originating in the rear quadrant. Thus, increasing terrain height results in larger w in the rear quadrant, which stems from increased downslope flow in the left quadrant on the uphill segment and an intensification of convergence in the rear quadrant.

Increasing the translation speed to $20\ \mathrm{m\,s^{-1}}$ (H50V) results in stark differences in maxUV and maxW. The most notable area of enhanced maxUV in H50V occurs in the first half of the uphill segment extending into the front and left quadrant with $uv > 70\,\mathrm{m\,s^{-1}}$ as far north as $y = 150$ m (Figure 4.3d). As the tornado approaches the uphill segment, increased translational velocity forces mass convergence in between the tornado and the hill resulting in increased uv. On the uphill segment, the core radius collapses with numerous areas of $w > 25\,\mathrm{m\,s^{-1}}$ (Figure 4.4d) before widening again. On the downhill segment, the main circulation lags behind to the southwest and a new circulation forms to the northeast of the original circulation. The new circulation becomes the main circulation by the time the tornado starts to ascend the next hill (Figure 4.7). During this transition, the influence

of the wind field drastically decreases in size. Lastly, though there are subvortices in H50V, the overall erratic behavior of the tornado makes it difficult to predict.

H50S demonstrates both the effects of a steeper approaching slope and an increased gap segment. The main area of maxUV occurs in the first half of the gap segment below $y = 0$ m (Figure 4.3e). Because the gap segment is much longer in H50 (around 600 m), flow channeling is unlikely the only cause of $uv > 80$ m s^{-1}. Streamlines from enhanced downslope winds converge with streamlines from the south leading to constricted flow and increased uv. This process also occurs place in the second half of the valley above y=0, with downslope streamlines converging with streamlines from the north. Subvortex formation from stretching of pre-existing vertical vorticity occurs in H50S as well. A steeper slope enhances downslope winds in the left quadrant resulting in an area of constant w > 20 m s^{-1} from which subvortices form. In fact, maxW > 25 m s^{-1} occur almost exclusively on the uphill segment (Figure 4.4e).

The center point of the tornado at 10 m AGL is tracked using the pressure deficit field for each simulation. The pressure deficit field is calculated by subtracting the maximum pressure in the upper core region (defined as $R < 250$ m and $750 < Z < 1250$ m) from the entire pressure field and multiplying by -1. To eliminate pressure deficits from sub-vortices, the field is averaged spatially using the nearest neighbor average. The location of maximum pressure deficit from the averaged field is the center of the tornado at 10 m AGL. Tracking the center point allows for the investigation of terrain influence on tornado position. Approaching the first uphill segment, the tornado in all five simulations drifts northward reaching y > 0 m at some point before the first hill (Figure 4.8). On the subsequent uphill / downhill segments, the tornado shifts south then moves north on the uphill.
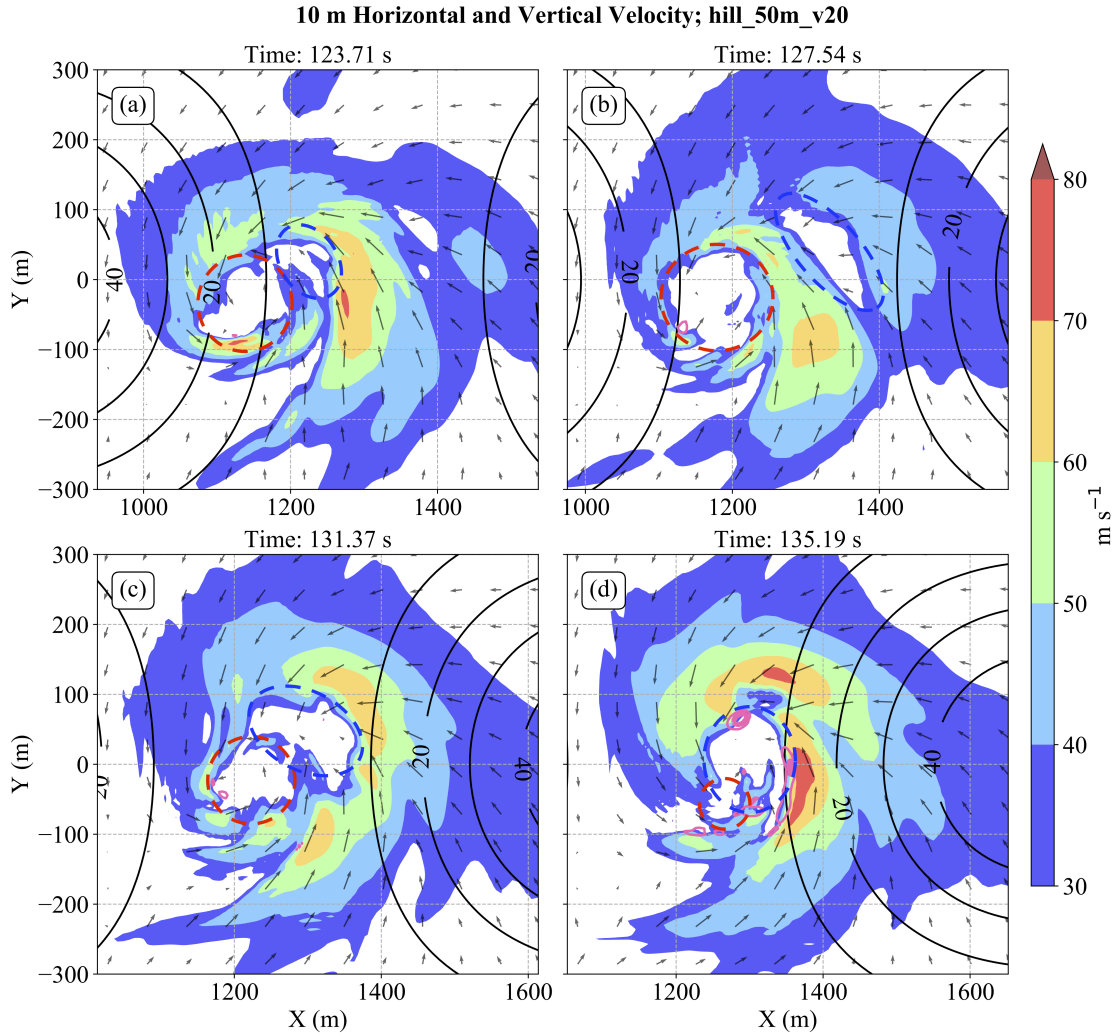
Figure 4.7: Sequence of images from hill_50m_v20 showing magnitude of 10 m horizontal velocity (shaded) with arrows showing horizontal wind direction. Thin and thick pink contours represent w > 20 m s^{-1} and 30 m s^{-1}, respectively. The dashed red circle denotes the old circulation and the dashed blue circle is the new circulation.
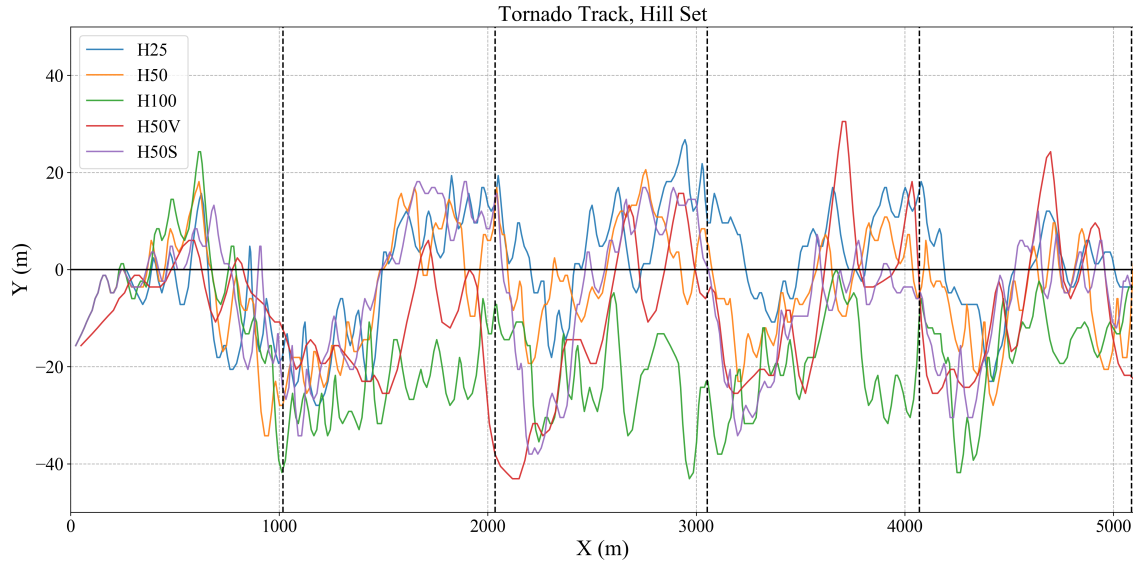
Figure 4.8: Time-series of 10 m center point calculated from averaging 10-m pressure deficit fields for the H25, H50, H100, H50V, and H50S. The vertical black dotted lines represent the top of the hill in each of the simulations.

This is followed by a sharp drop to the south once the tornado reaches the top of the second hill. Repeating behavior is then seen with a northward (southward) shift during the uphill (downhill) portion of the track. The main exception to this is H100 which stays below $y = 0$ m after the first hill. H50 also tends to stay further south than H25, evidence that larger terrain features lead to a more southward location of the tornado. The time-series of H50V has the largest variance, an indication that tornadoes with a higher forward speed have larger variability in their track (Figure 4.8. This variability in position in H50V is likely influenced by dissipation/formation of circulations. Lastly, out of all the simulations, H50S has the steepest southward drop in the downhill segment. Although an increase in steepness does not result in the tornado shifting a greater distance in the y-direction, a steeper hill causes the shift to occur more quickly.

4.1.2   Axisymmetric Time-Height Analysis

For axisymmetric variables (tangential, radial, and vertical velocities), the resolution of R bins from 50 to 200 m and Z bins from 0 to 75 m was 5 m. Everywhere else, R and Z bins were 10 m. The 5 m resolution area allows for a more detailed look at the corner flow region as well as the strongest inflow in the lowest 25 m. Axisymmetric calculations assume an origin at the center point given by the averaged 10-m AGL pressure deficit. Though using the same center point could be problematic when the tornado is tilted significantly, for most times / heights this assumption is sufficient. The time-height plots of axisymmetric variables give a different perspective than the 10-m track plots since 1) the plot gives a sense of the tornado structure in the vertical and 2) spatial averaging gives a mean representation of the tornado at a given time. For the discussion below on time-height plots, u_{min}, v_{max}, and w_{max} refer to minimum radial (maximum inflow), maximum tangential, and maximum vertical velocities, respectively.

From H25, H50, and H100, the last shows the most obvious influence of terrain on axisymmetric winds (Figure 4.9). The strongest v_{max} in H100 occurs on the downhill and in the gap segment, associated with the increased flow channeling and downslope winds (Figure 4.9c). Although the strongest v_{max} occurs in the layer between 25 and 50 m AGL, strengthening and weakening of v_{max} occurs through the lowest 200 m. There are instances where the weakening aloft lags that of below (e.g., after the first and second hills) and vice versa (e.g., first and fourth hill). The areas of strongest u_{min} coincide with areas of enhanced v_{max} (Figure 4.10c). Areas of strong u_{min} are found in a layer 0 to 25 m AGL (commonly > 40 m s^{-1}) and are found on the downhill. Conversely, the weakest u_{min} occurs at the
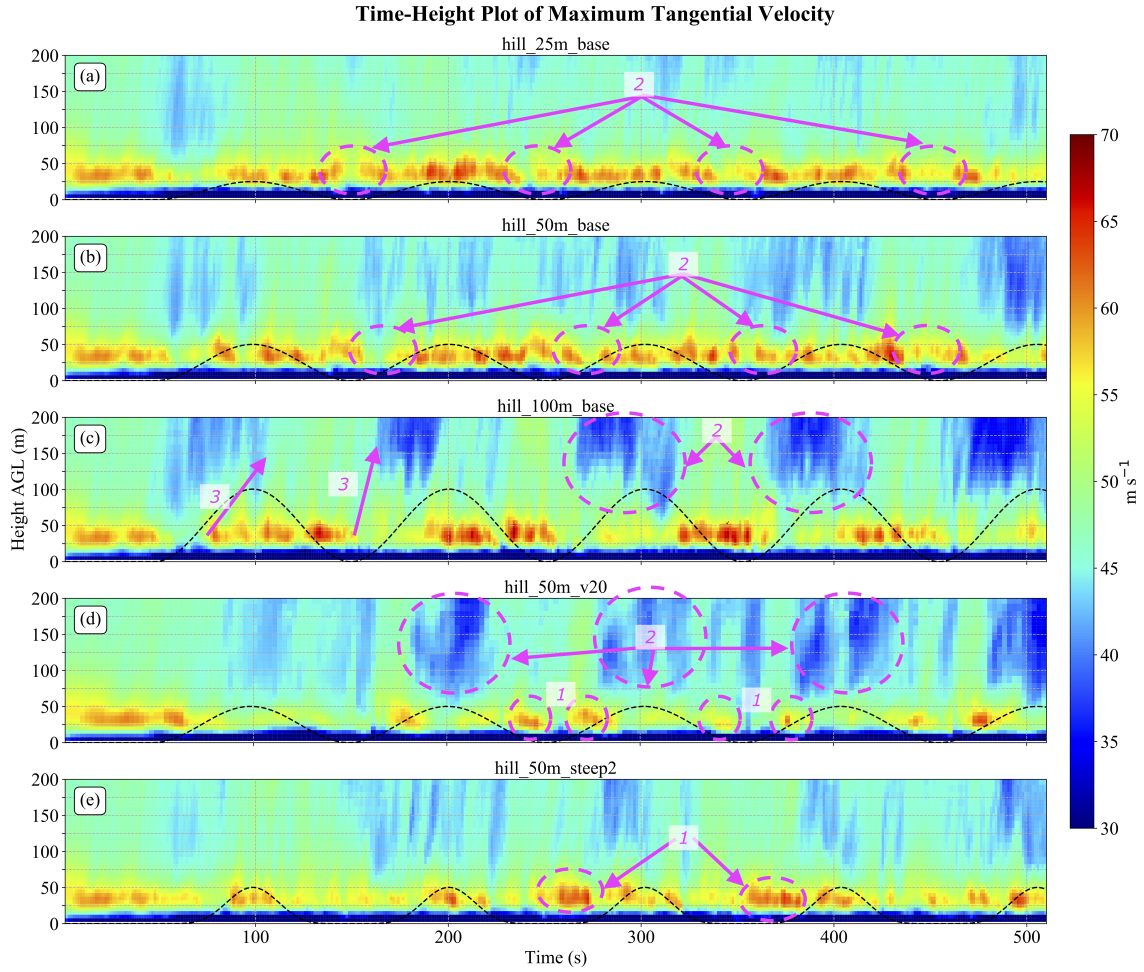
Figure 4.9: Annotated figure of axisymmetric time-height plot of maximum tangential velocity above terrain height for (a) H25, (b) H50, (c) H100, (d) H50V, and (e) H50S. Each grid point is the maximum tangential velocity through all R bins for that particular Z bin and time. The dotted lines represent the terrain height at the center of the domain for that particular time. Annotations are as follows: 1) Stronger v_{max}, 2) weaker v_{max}, and 3) delay in weakening / strengthening of v_{max} aloft compared to near-surface.
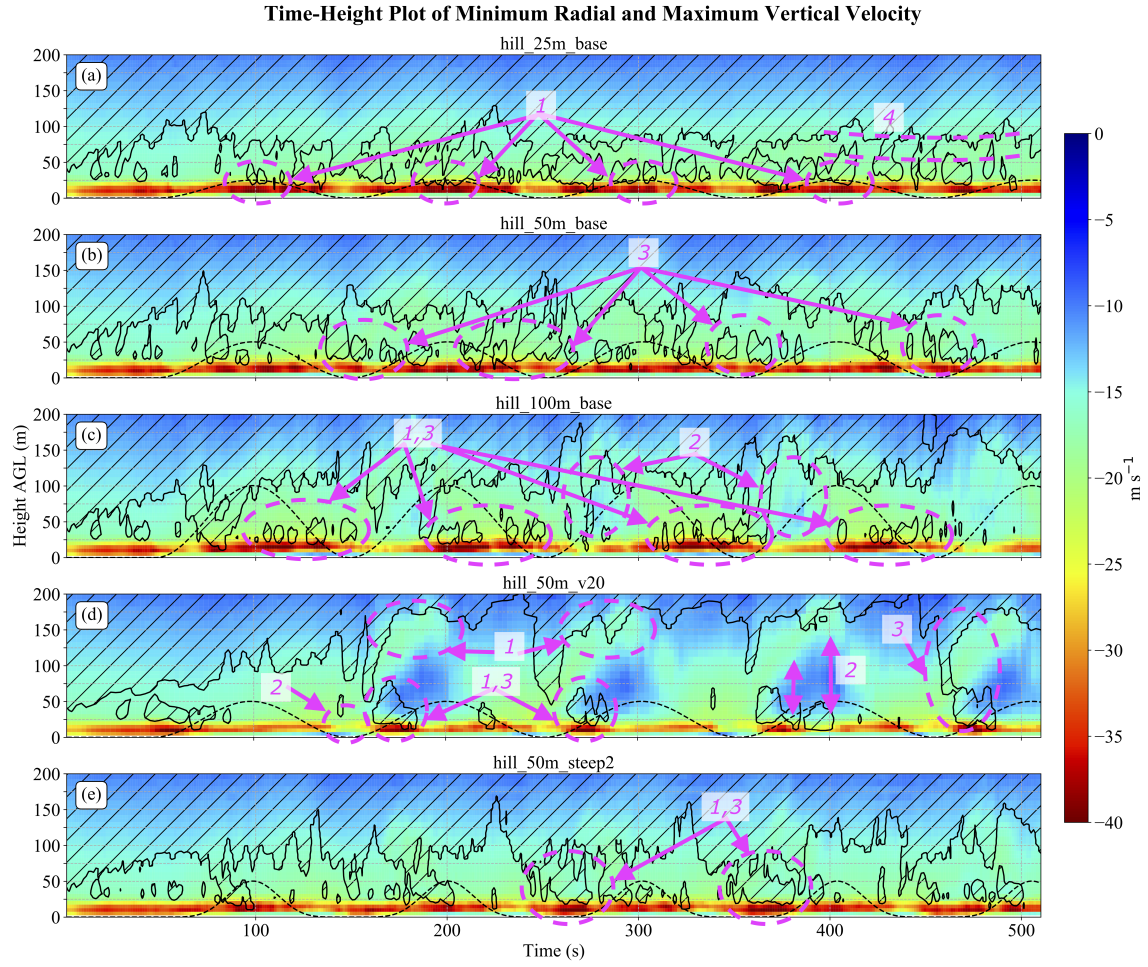
Figure 4.10: Similar to Figure 4.9 except for contoured for minimum radial velocity above terrain height and hatched contour of axisymmetric vertical velocities $> 20 \, \mathrm{m \, s^{-1}}$. Annotations are as follows: 1) Stronger u_{min}, 2) weaker u_{min}, 3) stronger w_{max}, 4) ribbon of weaker w_{max}.

beginning of the uphill segment. There is also a weakening of u_{min} aloft between 25 and 100 m AGL present in the middle of the uphill segment but unlike v_{max}, this weakening is not nearly as substantial, nor does it extend up to 200 m. Lastly, w_{max} shows two layers of enhanced vertical velocities, one where 25 m $< Z <$ 75 m and another where $Z >$ 75 m. These two areas are separated by a thin but distinct layer of weaker w_{max} located at 50 m $<$ $Z <$ 100 m (annotation 4 in Figure 4.10a). This structure of w_{max} is defining feature in all hill simulations. Before influence of terrain ($<$ 50 s into simulation) this ribbon of weaker w_{max} does not exist, thus the ribbon is a direct result of the addition of terrain.

Patterns in v_{max}, u_{min}, and w_{max} are not as obvious as in H25 and H50, i.e. magnitudes of weakening and strengthening is not to the extent of H100. However, there are some patterns that occur with predictability. Minimums in v_{max} for H50 are located when the tornado is in the gap and approaching the uphill segment (Figure 4.9b). Weaker v_{max} in H25 occurs at the end of the downhill and into the gap segment with possible strengthening of v_{max} at the top of the terrain. While patterns in u_{min} for H50 are hard to differentiate fro background variability (Figure 4.10b), strong areas of u_{min} in H25 favor the top of the terrain with weaker u_{min} at the end of the downhill and in the gap segment. Contours of w_{max} in H50 descend when the tornado is on the downhill and gap segment (Figure 4.10b), indicative of stronger w_{max} in this region. H25 shows no distinguishable pattern of w_{max} with respect to terrain, even at maximum terrain height where stronger u_{min} was evident (Figure 4.10a).

Above 100 m AGL, the contour of w_{max} is > 20 m s^{-1} is highest in H100 and lowest in H25, evidence that a larger terrain feature results in weaker w_{max} through a greater depth. Though 10-m track analysis show greater maxW for higher / steeper terrain on the uphill

segment, increased variability and asymmetry in the tornado structure aloft leads to weaker w_{max} for taller terrain. While overall tornado structure at 100 m AGL in H25 remains fairly symmetric, vertical velocities at the core radius in H100 become disorganized. On the downhill segment, w in the left and rear quadrants are consistently > 30 m s^{-1} from forced upslope flow while in the right and front quadrants w is reduced to < 20 m s^{-1}, attributed to forced downslope flow which suppresses upward motion.

The tornado in H50V results in weaker v_{max} relative to the other hill simulations (Figure 4.9d), with v_{max} rarely > 60 m s^{-1}. Overall weaker v_{max} may stem from higher variability of wind speeds in H50V and the inability to establish a solid core radius surrounding the central axis. Regardless, there is weaker v_{max} centered above the maximum terrain height. Closer to the surface, there is one location of stronger v_{max} at the end of the downhill and another at the beginning of the uphill. The former is the result of enhanced downslope flow that works in conjunction with the translational velocity and the latter is consequence of forced convergence between the tornado and terrain from increased translational velocity as discussed previously. Both areas of stronger v_{max} are collocated with stronger u_{min} and w_{max} (Figure 4.10d).

The pattern of u_{min} is especially interesting in H50V. The downhill and beginning of the gap segment have weaker u_{min} near the surface. On the uphill there is a layer of relatively weak u_{min} between 25 and 75 m AGL which grows upwards to 125 m AGL as the tornado ascends the hill which occurs in conjunction with a layer of u_{min} strengthening from 125 m to 200 m. Stronger u_{min}, or strengthening outflow, located just above strengthening inflow collocated with stronger v_{max} and w_{max} is indicative of a more robust corner flow region (CFR) on the uphill segment in H50V. Lastly, w_{max} aloft is relatively weaker except in the

valley where there is a strengthening of w_{max} through the entire column from 50 - 75 m AGL up to 200 m AGL, collocated with the intensification of v_{max} aloft (Figure 4.10d).

Lastly, all hills in H50S are characterized by increased v_{max} near the top of the hill (Figure 4.9e). The valley is also marked by a significant increase in v_{max} (third and fourth hills) collocated with an increase in u_{min} and w_{max} (Figure 4.10e). Aloft, v_{max} is stronger in the valleys and weaker at the top of the hills. Additionally, u_{min} is weakest at the end of the downhill while w_{max} is the strongest in the valley / uphill and weakest on the downhill (Figure 4.10e).

4.2 Sinusoid Set

4.2.1 10-m track

For the sinusoid set, four different simulations were run with increasing maximum terrain height; 10 m (S10), 25 m (S25), 50 m (S50), and 100 m (S100). Axisymmetric variables for S50 are investigated first. The largest area of enhanced maxUV in S50 occurs in gap segment, characterized by a swath of maxUV $> 70\,\mathrm{m\,s^{-1}}$ some regions exceeding $80\,\mathrm{m\,s^{-1}}$. Further analysis reveals enhanced downslope winds $> 70\,\mathrm{m\,s^{-1}}$ at the end of the downhill segment play a role in this area of higher maxUV. However, flow channeling from winds coming from the south, parallel to the long axis of the gap segment, are mainly responsible for the increase of uv. Wind vectors suggest the strongest uv originates from flow off the southern boundary which never encounters significant terrain as it flows northward, parallel to the valley axis.
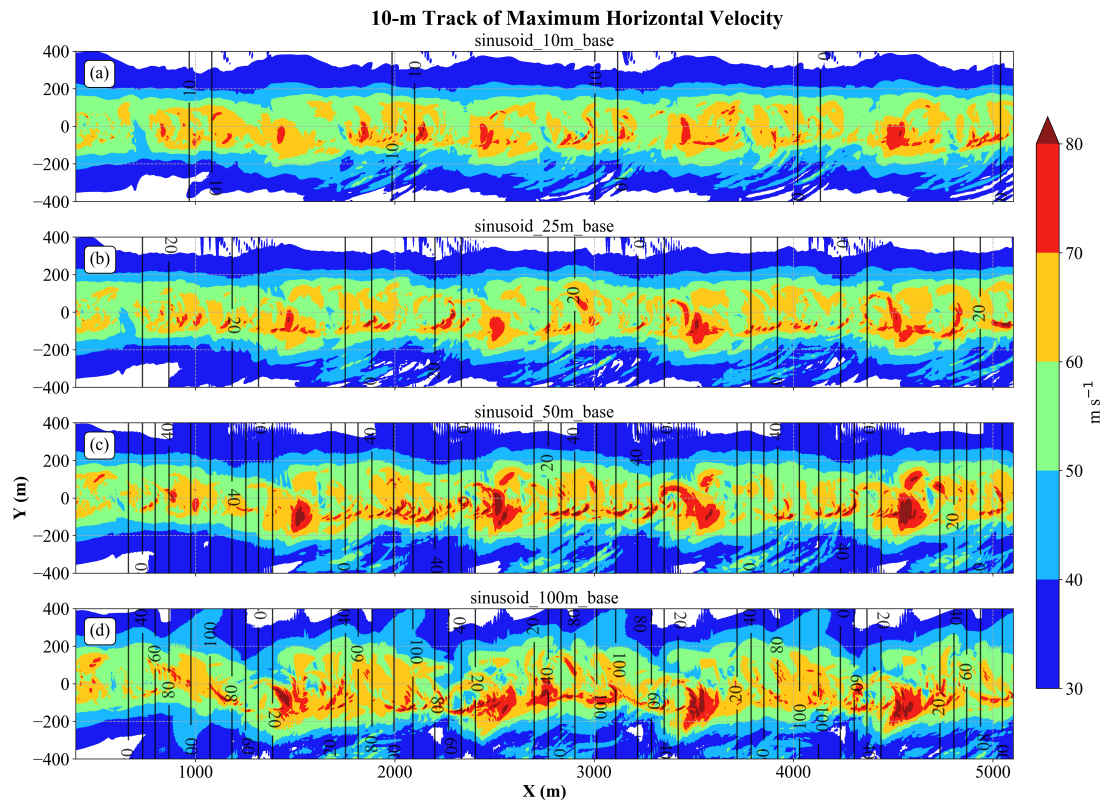
Figure 4.11: Similar to Figure 4.3 except for (a) S10, (b) S25, (c) S50, (d) S100.
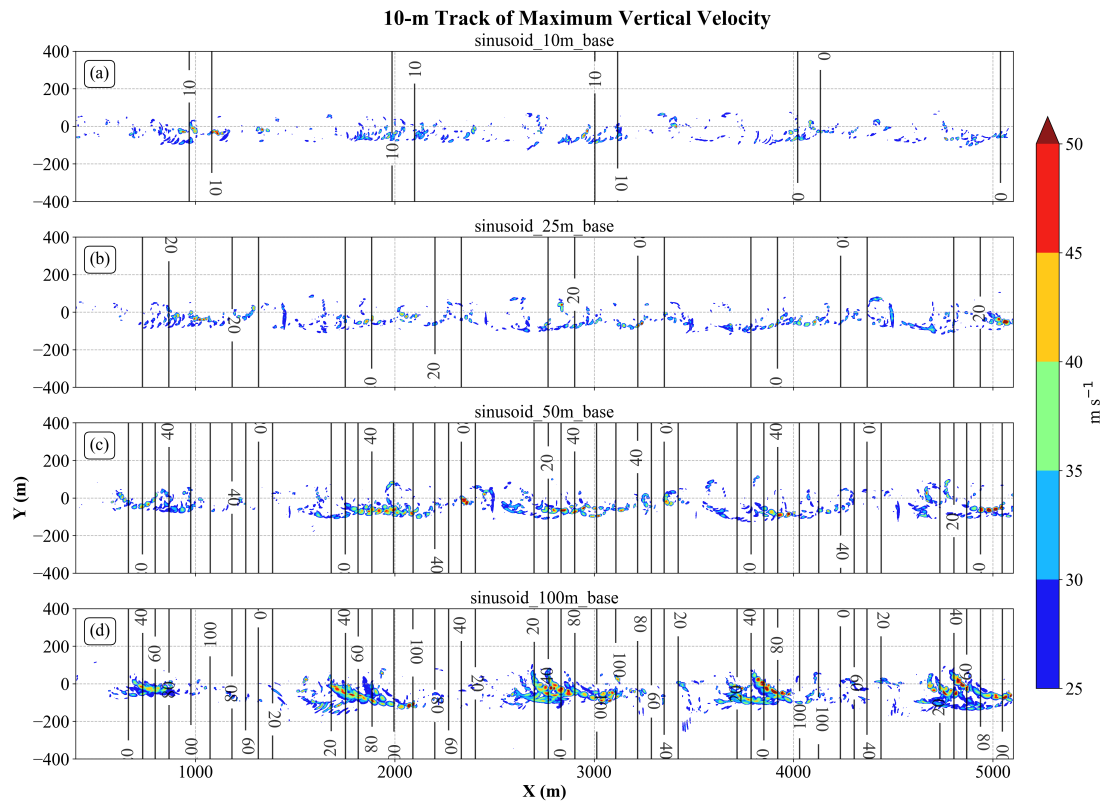
Figure 4.12: Similar to Figure 4.4 except for (a) S10, (b) S25, (c) S50, (d) S100.

10 m Horizontal and Vertical Velocity; sinusoid_50m_base
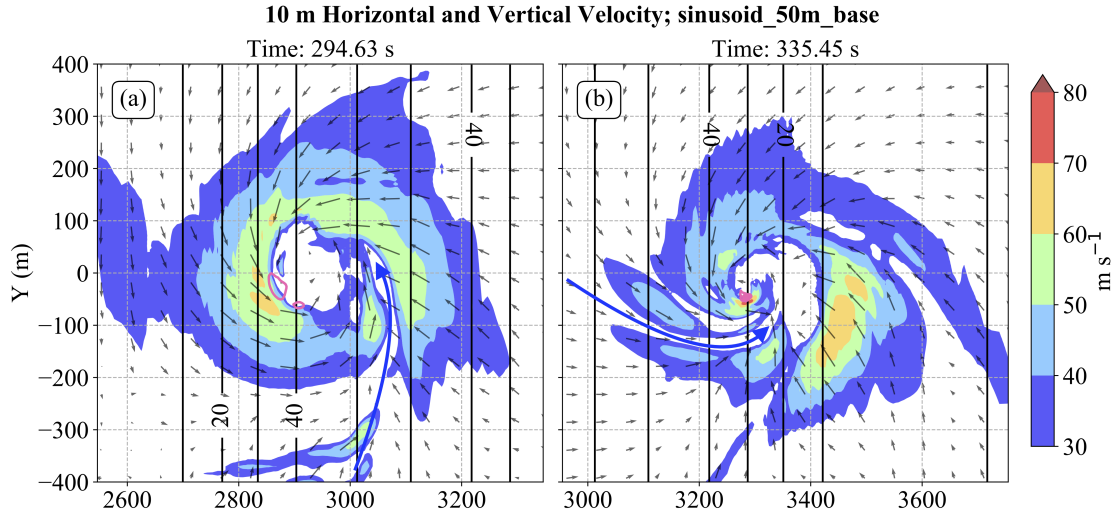
Figure 4.13: Similar to Figure 4.5 except for S50 showing the low *uv* ribbon on both the uphill and downhill segments denoted by blue arrows.

Flow channeling is more significant in S50 than H50, likely due to the increased length of the gap segment in the *y*-direction and increased time for the flow to be constricted. While on the downhill segment, S50 also has the presence of a low *uv* ribbon that develops in the rear quadrant and entrains into the center of the tornado in H50 (Figure 4.13). This ribbon forms from similar mechanisms: upslope flow in the left quadrant encounters enhanced frictional effects, leading to an increased depletion in *M*. This depletion in *M* causes parcels to rotate inward and the tornado takes on an occluded look, allowing for the entrainment of highly frictionally-modified air whose speed has been reduced. S50 also has a smaller low *uv* ribbon that develops on the uphill of S50 in the front quadrant. Though this ribbon is less persistent, the same process may be responsible on the uphill, i.e., flow in the right quadrant tends towards smaller *R* and frictionally-modified air is entrained off the southern boundary.

The second area of enhanced maxUV for S50 occurs on the uphill and downhill segments where $y < 0$ m and has a broken appearance, the result of robust subvortices (Figure 4.11c). Robust subvortices favor the uphill slightly conveyed by stronger maxW on the uphill segment (Figure 4.12c), but not to the extent they did in H50. Stronger maxW on the uphill segment may be resultant from subvortex motion and uv in the right quadrant of the subvortex have a component of ascent from upslope terrain. For the subvortices on the downhill, maxW patterns show the radius about which the subvortices rotate shrinks, evidence the tornado's core radius has contracted. Further investigation reveals that on the downhill segment, the tornado's circulation shifts southward and a new circulation forms to the northeast, similar to processes in H50V. Due to the increased areal extent of the terrain to the southern and northern boundaries, the average parcel that the tornado ingests at the top of the hill has a lower M from increased frictional effects in S50 compared to H50. Thus, the parcels reach a smaller R, leading to a smaller core radius.

The contraction of the tornado is more pronounced in S100 - on the uphill segment the terrain effects result in an elongation of the tornado's appearance. Once the tornado reaches the top of the hill, the core radius is effectively reduced to zero, the tornado fails to maintain any respectable surface pressure deficit, and the areal extent of tornadic wind speeds is reduced (Figure 4.6b-d). The circulation sharply shifts southward until the tornado starts pulling in higher M air from lower terrain, resulting in a widening of the tornado (Figure 4.14e). However, a new circulation develops to the northeast of the old circulation near the center of the domain and becomes the new tornado (Figure 4.14f). Without boundary conditions continuously supplying both high M air and an updraft to drive inflow, the terrain in S100 could be substantial enough to terminate the vortex.
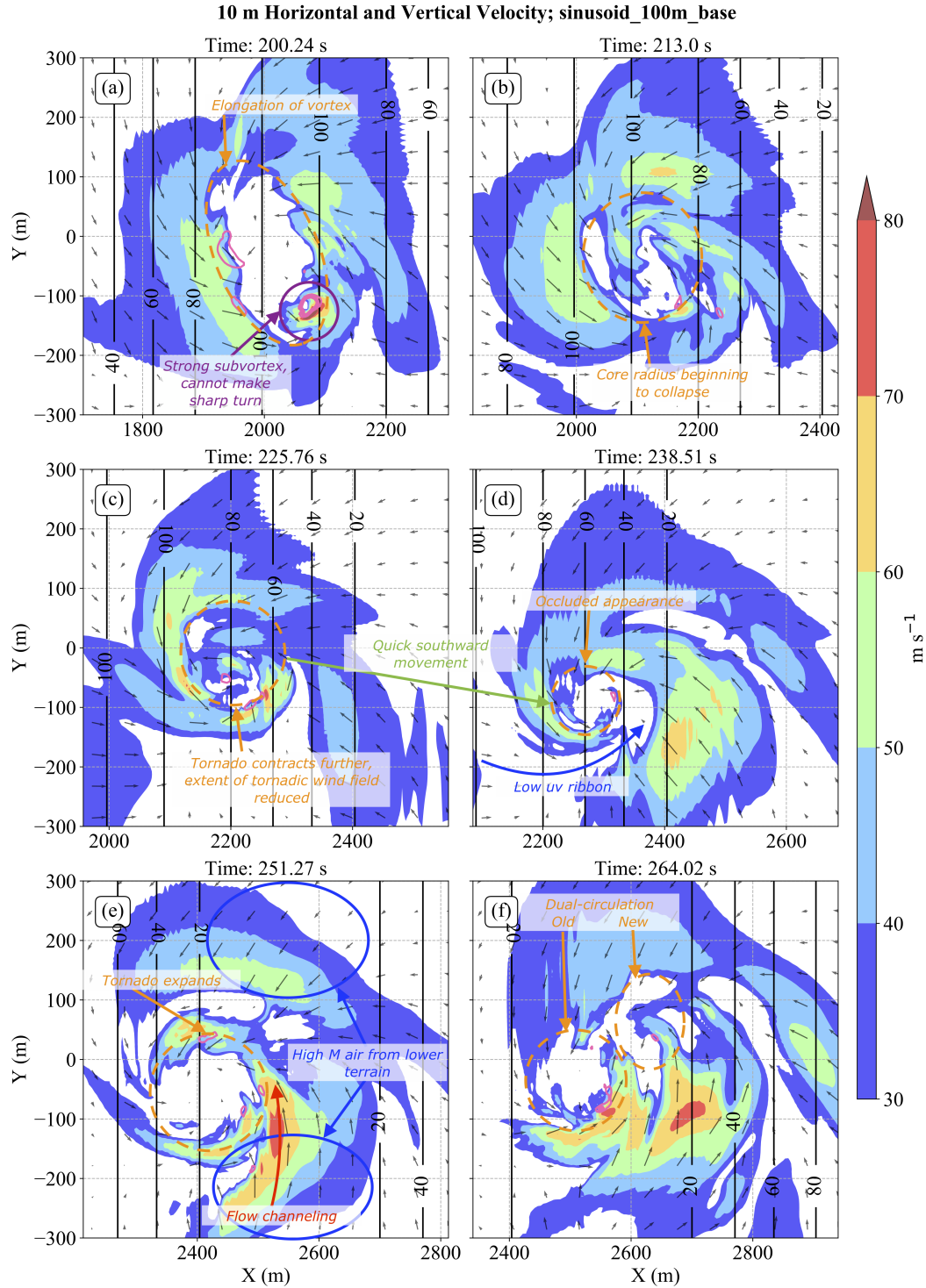
Figure 4.14: Similar to Figure 4.13 for S100 highlighting key processes from the top of the hill to the subsequent gap segment: (a) elongation of the vortex on the uphill and robust subvortex, (b) contraction of vortex, (c) further contraction with reduced wind field, (d) occlusion appearance with low *uv* ribbon from higher terrain, (e) expansion of core radius with higher M air along with faster *uv* from flow channeling and (f) messy attempt at reorganization while in the gap segment.

Despite deviant motion and erratic behavior of the vortex, there is enhanced maxUV in the gap segment where downslope winds and flow channeling leading to stronger uv, the latter being the more significant process (Figure 4.11d). The ribbon of weak uv is still discernible in S100, both on the uphill and downhill. On the uphill segment, the area of maxUV > 25 m s^{-1} is relatively widespread owing to increased convergence in the rear quadrant (Figure 4.12d). Within this area of maxUV > 25 m s^{-1}, there is a broken pattern of maxW > 45 m s^{-1}, the result of intense subvortices that form in the rear quadrant. Interestingly, the subvortices terminate at the intersection of the right and front quadrant, which is quicker termination than seen previously, resulting in a southwest movement of the strongest maxW pattern (Figure 4.12d). Though the subvortices in S100 are the most intense out of any simulation, the elongation of the tornado on the uphill segment makes it difficult for the subvortex to make the sharp turn and remain in a favorable location (Figure 4.6a).

Though less pronounced than S50 and S100, S10 and S25 show areas of increased maxUV in the valley region (Figure 4.11a-b). Due to the relatively small size of the terrain features in S25 and especially in S10, it is possible that there are other dynamical processes in addition to flow channeling that play a role in increased uv. There are a couple of important features associated with these swaths of enhanced uv: 1) the swaths tend to occur in the first half of the gap segment rather than the middle and 2) the swaths are associated with an narrow area of vertical velocities > 20 m s^{-1} at R just less than the swath itself. Nevertheless, in both S10 and S25, the low uv ribbon is still prevalent on the downhill segment. Additionally, subvortices exist on both the uphill and downhill segments with the uphill favoring more robust subvortices. Lastly, the core radius contracts on the
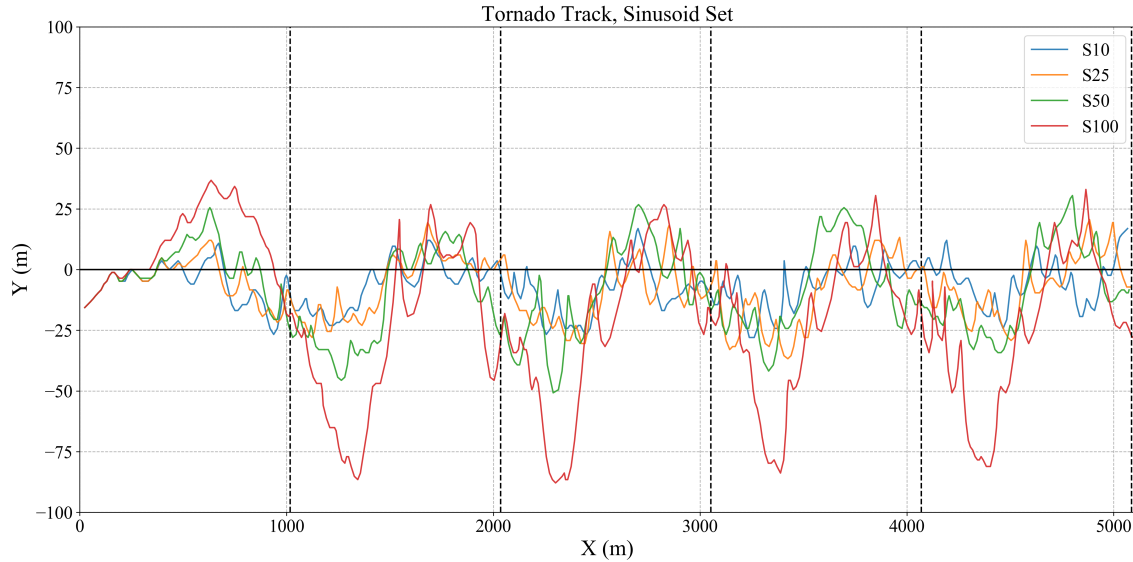
Figure 4.15: Time-series of 10 m center point calculated from averaging pressure deficit fields for the S10, S25, S50, and S100. The vertical black dotted lines represent the top of the hill in each of the simulations.

downhill segment in both S25 and S10. Thus, a relatively small 10 m hill still affects tornado structure and behavior (Figure 4.11a and 4.12a).

The location of the tornado in all of the sinusoid simulations follows the same pattern, regardless of hill height (Figure 4.15). Before the tornado approaches the first uphill segment there is a shift to the north; all simulations reach y > 0 before moving southward during the uphill and downhill segment. Sometime between the midpoint of the downhill and beginning of the gap segment, the tornado slowly starts to shift north and continues so for the majority of the uphill segment. Repeating behavior is then seen with a shift south (north) on the downhill (valley / uphill). The amplitude of the north / south shifts is directly related to maximum hill height; S100 has the strongest response followed by S50 and then S25 and S10. Again, even in S10 there is a clear deviation of the tornado track with respect to terrain. The shift in the S100 simulation to the south far exceeds that of S50, > 30 m
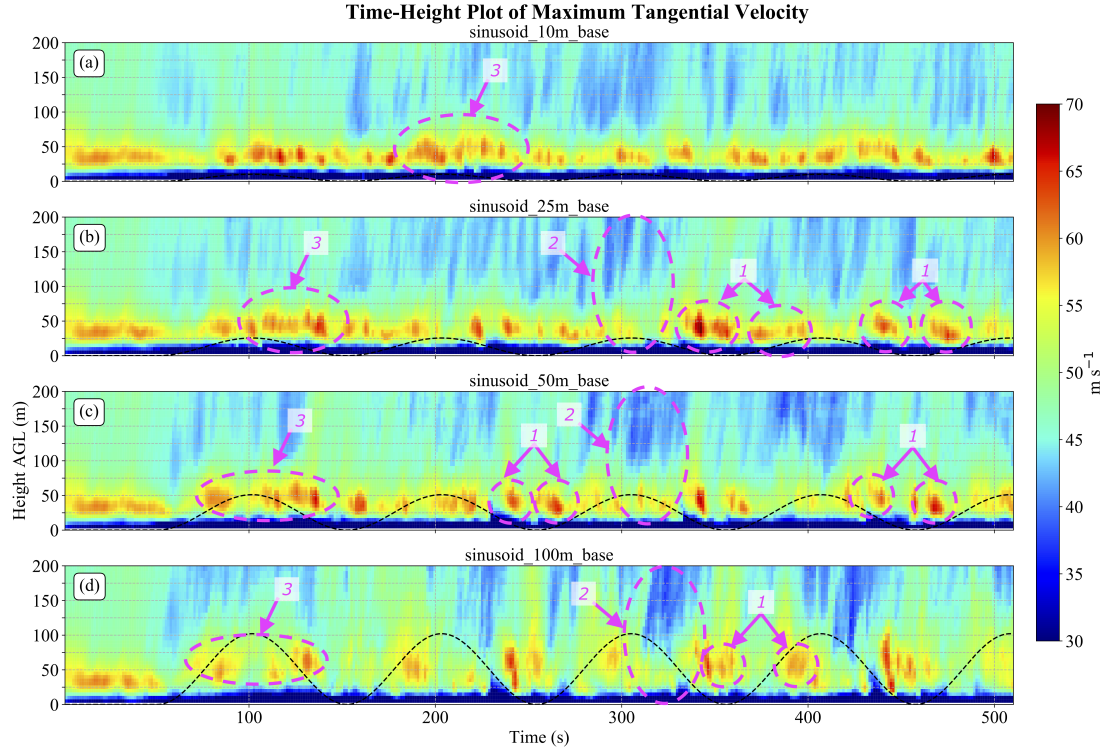
Figure 4.16: Annotated figure of axisymmetric time-height plot of maximum tangential velocity above terrain height for (a) S10, (b) S25, (c) S50, and (d) S100. The dotted lines represent the terrain height at the center of the domain for that particular time. Annotations are as follows: 1) Stronger v_{max}, 2) weaker v_{max}, and 3) elevated CFR

in difference at the southernmost point. Comparing sinusoid and hill sets, the deviations in the sinusoid simulations are larger for a given maximum terrain height. For example, the maximum southern displacement in H50 is about 35 m compared to 50 m in S50, evidence that increased areal extent of terrain and therefore increased averaged residence time of air parcels on higher terrain will lead to a greater deviation.
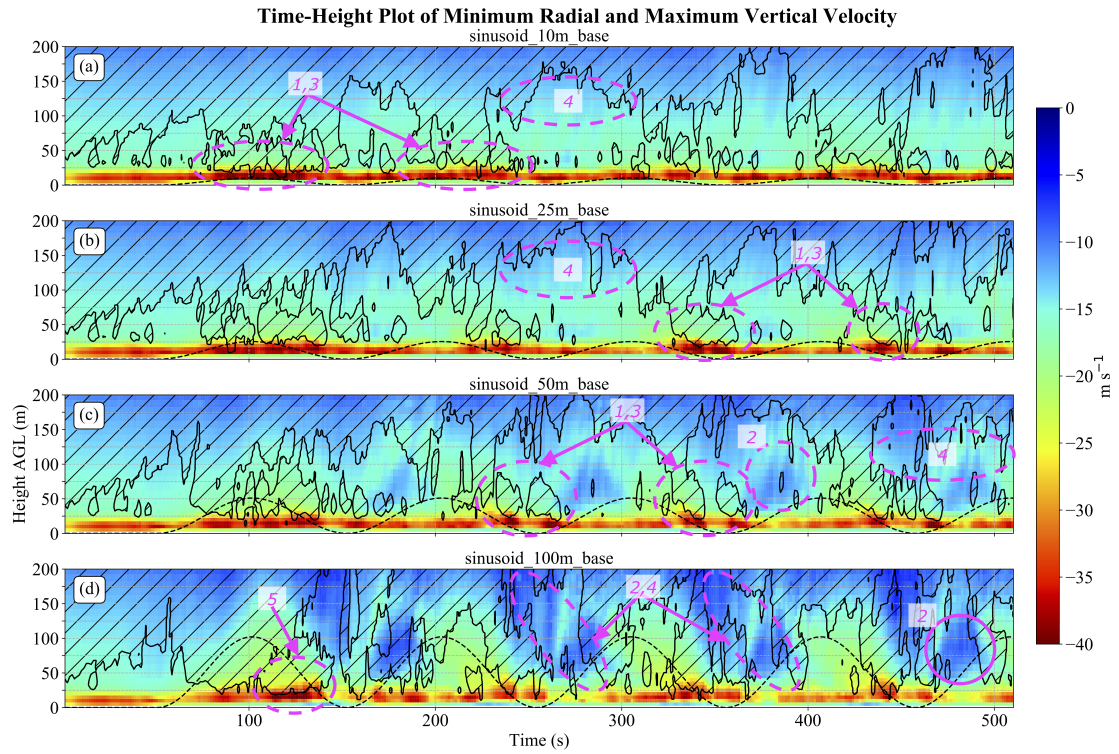
Figure 4.17: Similar to Figure 4.16 except for contoured for minimum radial velocity above terrain height with hatched contour of maximum axisymmetric vertical velocities > 20 m s^{-1}. Annotations are as follows: 1) Stronger u_{min}, 2) weaker u_{min}, 3) stronger w_{max}, 4) weaker w_{max}, and 5) elevated strong u_{min} (and CFR).

4.2.2 Axisymmetric Time-Height Analysis

Axisymmetric calculations show that overall, the sinusoid set has a slightly weaker overall v_{max} than the hill set (Figure 4.9). While maximum values of v_{max} between the hill and sinusoid set are comparable, the occurrences of v_{max} reaching such a magnitude decrease for the sinusoid set. This decrease in local maxima becomes increasingly obvious for increased terrain height; in S100 the areas of $v_{max} > 60 \text{ m s}^{-1}$ are relatively infrequent. Weaker overall v_{max} for the sinusoid set is the result of increased disruption of the vortex compared to hill set, reducing magnitudes of calculations that involve spatial averaging. Additionally, the extent of the overall tornadic wind field is reduced especially on the downhill. Through all simulations, stronger u_{min} is located either on the top of the terrain or in the downhill segment. Most areas of stronger u_{min} are collocated with enhanced w_{max} in a layer just above the surface.

An important difference between the sinusoid and hill set is the height at which the local maxima in v_{max} (Z_{max}) is found. With the hill set, the Z_{max} is located between 25 and 50 m AGL with little change with respect to the terrain (Figure 4.9). Meanwhile Z_{max} in all sinusoid simulations clearly increases during the downhill segment, i.e. the location of v_{max} maxima become elevated. Additionally, the magnitude to which Z_{max} is affected is proportional to the size of the terrain. In S10, the maximum value of Z_{max} is about 50 m AGL, occurring around 225 s (Figure 4.16a). For S25 and S50 maximum Z_{max} is $>$ 50 m and for S100, maximum Z_{max} increases even further to 100 m AGL (Figure 4.16b-d). In addition to an increase in Z_{max}, there is also a layer of weak v_{max} near the ground that becomes more prominent with increasing terrain height, evidence of an increasing

depletion of M. During periods of elevated Z_{max}, the depth of stronger u_{min} also increases. In S100, areas of $u_{min} > 25$ m s^{-1} reaches up to 50 m AGL (Figure 4.17d), much higher than H100 in which $u_{min} > 25$ m s^{-1} is restricted to the lowest 25 m AGL. Once again, these patterns signify that increased spatial extent of terrain causes a larger disruption in the vortex due to increased frictional effects.

The areas where Z_{max} is the highest corresponds to areas of strongest v_{max} (Figure 4.16), excluding S10 where periodic behavior in axisymmetric variables is difficult to discern. In S25 and S50, there is a secondary maximum in v_{max} at the beginning of the uphill segment with a minimum in v_{max} directly in the center of the valley, similar to the pattern noted in H50V. Both the downhill and uphill v_{max} maxima are associated with flow channeling from the south and north, respectively. Although flow channeling only enhances winds occur in the right quadrant, the increase is substantial enough to enhance v_{max} in axisymmetric calculations. Weaker v_{max} in S25 and S50 are centered on the top of the hill and occur through the lowest 200 m, likely a result of the tornado entraining highly frictionally-modified air (Figure 4.16b-c). The weakest v_{max} in S100 occurs on the downhill segment (Figure 4.16d), likely because this is the location in which the original circulation terminates and the tornado must reorganize.

The pattern of near-surface u_{min} for S25 and S50 match up with patterns in v_{max} (Figure 4.17). There is also a dipole maximum in u_{min} located at the end of the downhill and beginning of the uphill segment, most obvious in S50 (Figure 4.17b-c). The u_{min} pattern is also interesting aloft for S50 and S100. On the uphill, there is weakening in u_{min} in an intermediate layer from 25 to 100 m deepens until the tornado reaches the top of the hill (Figure 4.17c-d). Simultaneously, there is a layer above the intermediate layer between
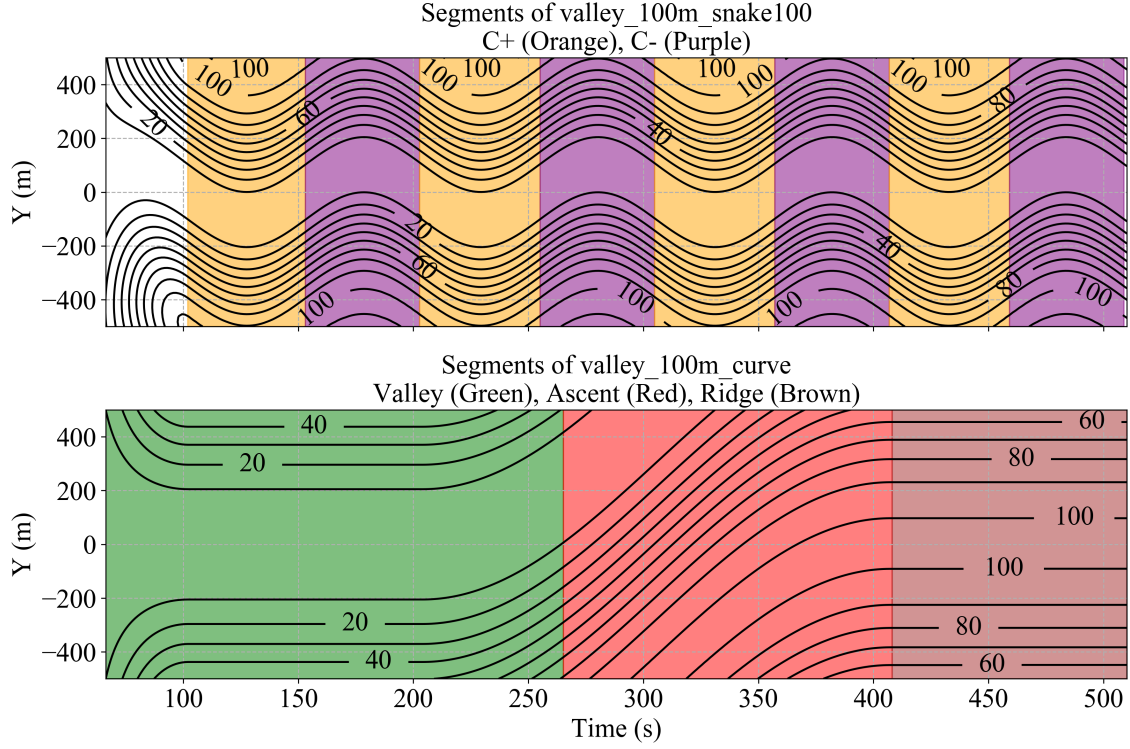
Figure 4.18: Segmentations of V100S (top) and V100C (bottom). The orange and purple shading correspond to concave up (C+) and concave down (C-) regions of V100S, respectively. For V100C, green, red, and brown shading corresponds to valley, ascent, and ridge segments, respectively.

100-150 m characterized by a slight strengthening in u_{min}. This pattern in u_{min} aloft mirrors the pattern in H50V (Figure 4.10d).

4.3 Valley Simulations

For the valley set, the chosen simulations are a straight 50 m valley (valley_50m_base, hereafter V50), a straight 100 m valley (valley_100m_base, V100), a 100 deep m valley that oscillates ± 100 m in the direction of translation (valley_100m_snake100, V100S), and a 100 m valley that curves away approximately at the mid-point of the simulation (valley_100m_curve, V100C). V100S is segmented by concavity of the oscillation, concave
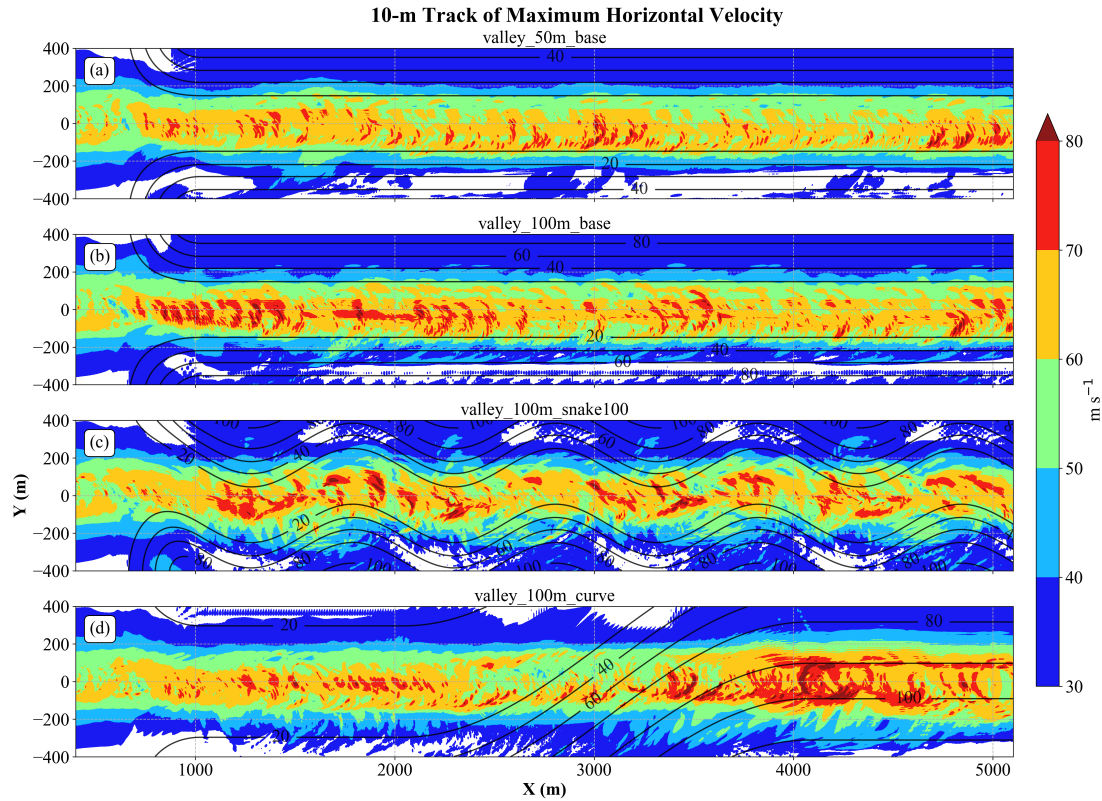
Figure 4.19: Similar to Figure 4.3 except for (a) V50, (b) V100, (c) V100S, and (d) V100C.

up (C+) and concave down (C-). V100C is split into three segments - valley (tornado at the lowest point in the valley), ascent (tornado ascends out of valley), and ridge (tornado completes ascension) (Figure 4.18b).

4.3.1   10-m track

As the tornado enters the valley, there is a general increase in 10-m maxUV for V50 and V100, with the latter having stronger maxUV overall (Fiure 4.19a-b). Because the center of the domain is aligned with the lowest point in the valley, easterly and westerly flow from the tornado (parallel to the valley axis) is offset from the center of the valley. Thus, flow
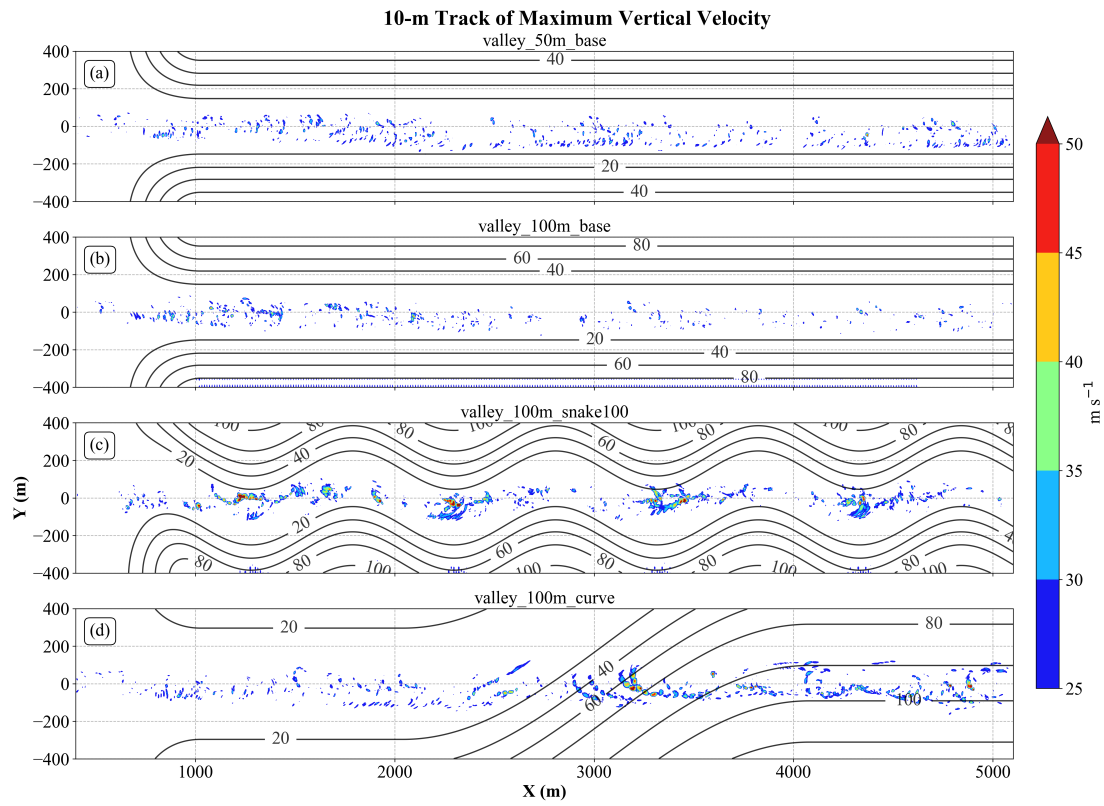
Figure 4.20: Similar to Figure 4.4 except for (a) V50, (b) V100, (c) V100S, and (d) V100C.

channeling from constriction between terrain features that was noted in hill and sinusoid sets in the gap segment plays less of a role in V50 and V100.

Areas of enhanced maxUV in V50 are constricted mostly to the southern half of the valley (Figure 4.19a). Further investigation reveals patterns in maxUV are the result of quite a few processes while the tornado is in the valley. First, enhanced downslope winds in the right quadrant from flow coming off of the side of the valley results in fairly consistent $uv > 60$ m s^{-1} and occasionally > 70 m s^{-1} (Figure 4.21a-b). These maxima in uv are periodically associated with small areas of enhanced w and are possibly the product of short-lived subvortices (Figure 4.21a-b). These show up as speckled areas of maxUV $>$ 25 m s^{-1} (Figure 4.20a), but overall there is a lack of robust subvortices in the valley set, leading to reduced maxW compared to the hill or sinusoid set. This dearth of subvortices can be attributed to ingested flow into the tornado having a downslope component from all directions, suppressing positive w.

In the left quadrant in V50, flow is still subjected to upslope terrain and enhanced frictional effects. The upslope terrain is enough to deplete angular momentum such that flow rotates inwards towards the center axis (Figure 4.21a-b). Once the flow turns inwards, it aligns parallel to the valley axis and flow channeling becomes relevant, leading to fairly consistent $uv > 60$ m s^{-1} in the rear quadrant (Figure 4.21c). In the hill and sinusoid set this turning inward led to the entrainment of a low uv ribbon from higher terrain. However, the ribbon is not a defining feature in V50 since entrained flow originates from low terrain whose speeds have not been greatly reduced (Figure 4.21c). While there is a small low uv ribbon that develops in the right quadrant from upslope flow off the sides of the valley (Figure 4.21d), this ribbon is not nearly as prominent or persistent as the ribbon in the hill

and sinusoid set. The combination of flow that turns inward and the lack of a low *uv* ribbon results in a disorganized appearance with a dual-circulation feature (Figure 4.21d).

Patterns in V100 are an amplification of patterns in V50; overall, maxUV is stronger and maxW is weaker in V100. Enhanced downslope winds in the right quadrant are stronger with consistent $uv > 70$ m s^{-1} reaching values > 80 m s^{-1}. The areal extent of enhanced downslope flow increases into the front quadrant, evident by a northward extension of maxUV > 70 m s^{-1} (Figure 4.19b). The inward turning of flow from flow off of the sides of the valley in the left quadrant is sharper, enhancing flow channeling in the rear quadrant, leading to $uv > 70$ m s^{-1} in this region. Even flow off of higher terrain in the right quadrant exhibits a sharper turn in the right quadrant to align with the valley axis, resulting in increased *uv* from flow channeling to the northeast of the circulation. Increased downslope component of the flow from all directions further suppresses positive *w*, resulting in decreased areas of maxUV > 25 m s^{-1} in V100 (Figure 4.20b).

Oscillating the valley in V100S results in an increased influence of the valley in determining where areas of strongest *uv* occur. Regions of enhanced maxUV appear to favor the lower terrain and oscillate with the valley (Figure 4.19c). Because flow in both the front and rear quadrant turn to align themselves with the valley axis (Figure 4.22a), areas where maxUV > 70 m s^{-1} occur in conjunction with terrain > 10 m are sparse, even in the center of C+ and C- segments where 10 m terrain height is in the center of the domain. While strongest maxUV areas do not favor either the C- or C+ segment, areas of stronger maxW for V100S is biased towards the center of the C- segment where the valley axis is at its southernmost point. Magnitudes of maxW reach > 50 m s^{-1} during the C- segments, far stronger than the maximum maxW values in V50 or V100. On the other hand, maxW

82
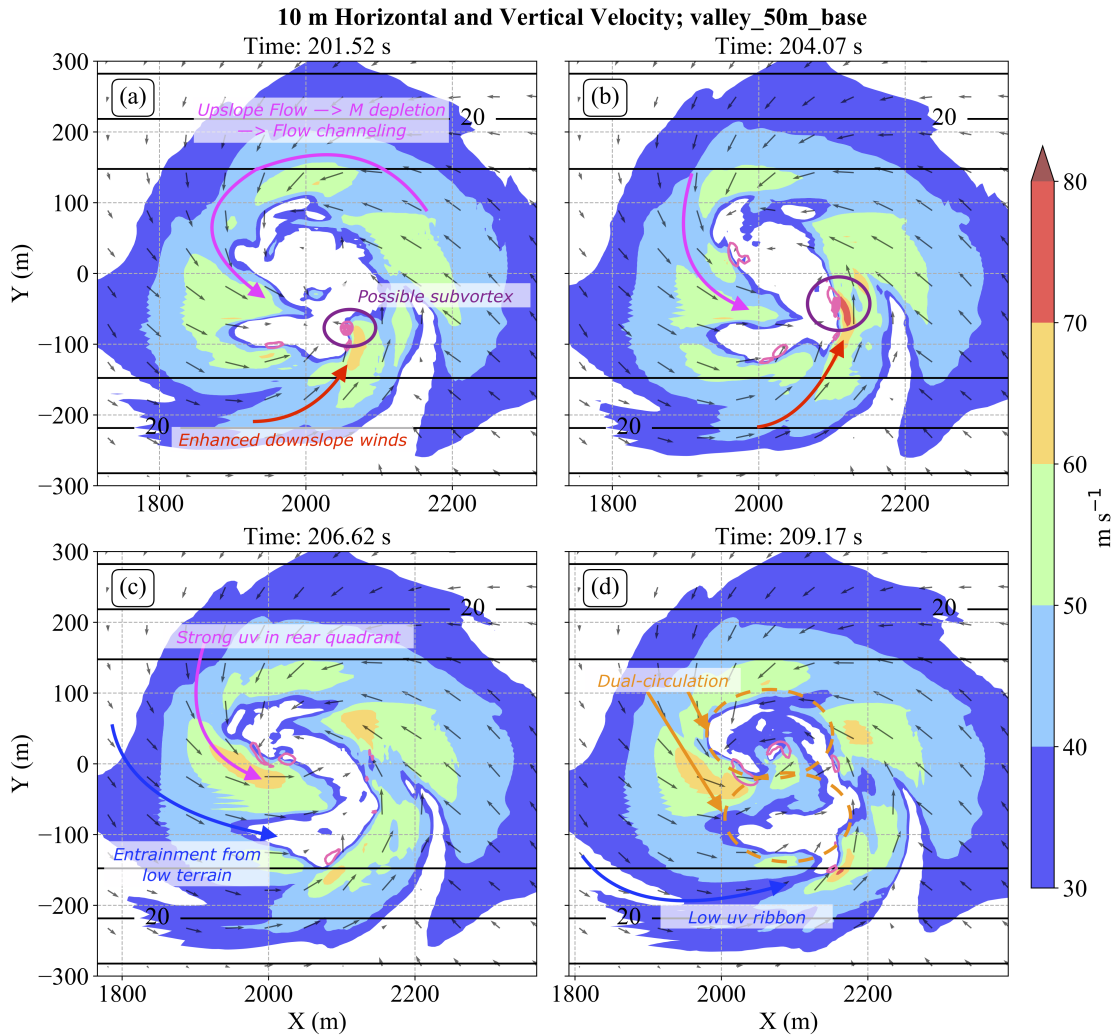
Figure 4.21: Sequence of images of horizontal and vertical velocity similar to Figure 4.14. Important features noted include: (a) upslope flow leading to flow rotating inward with enhanced downslope winds and a possible subvortex in the right quadrant, (b) continuation of previous features and translation of subvortex, (c) strong *uv* in rear quadrant from flow channeling and (d) small low *uv* ribbon in right quadrant from entrainment from slightly higher terrain and disorganization of tornado circulation.

83

10 m Horizontal and Vertical Velocity; valley_100m_snake100
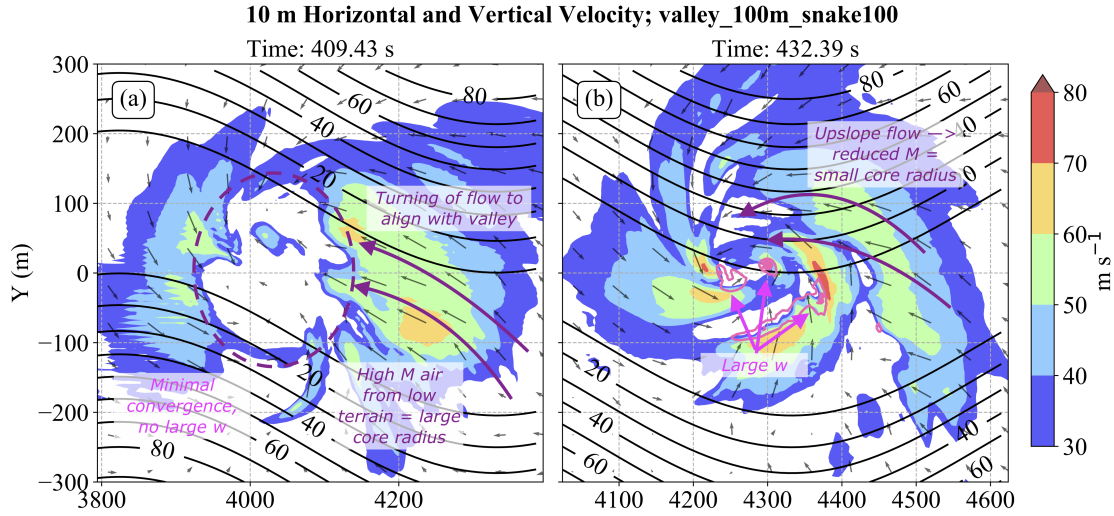
Figure 4.22: Sequence of images of horizontal and vertical velocity similar to Figure 4.21 for V100S showing (a) widening of core radius in C- segment and (b) contraction of core radius in C+ segment.

is weakest during the C+ segments of V100S. During C+ segments of the valley, the core radius of the tornado is at its widest point as flow in the right quadrant is able to ingest high angular momentum air from lower terrain (Figure 4.22a). On the other hand, during C- segments, the tornado is unable to ingest flow that is not significantly depleted in M / highly frictionally-modified. This results in a rapid contraction of the tornado and collapse of the core radius which leads to intense convergence and areas of large w (Figure 4.22b).

The last simulation in the valley set is V100C which was chosen to emulate the physical terrain that the 2018 April 13 Mountainburg, AR EF-2 tornado encountered. The Mountainburg tornado started at an elevation of 200-250 m and weakened when it ascended out of the valley, gaining approximately 200 m in elevation (Figure 4.23). During the beginning of the ascent, there is an increase in the core radius along with an overall weakening in maxUV and maxW (Figure 4.19d and 4.20d). Then about 30 m into ascent, there is an
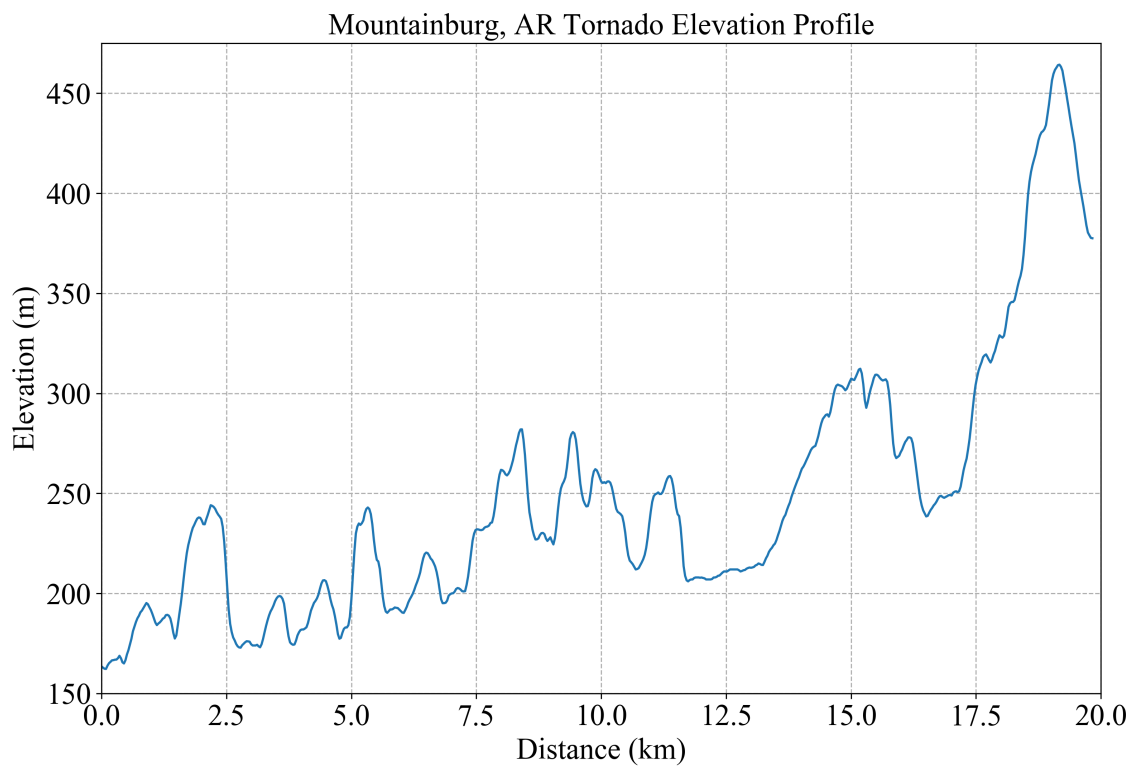
Figure 4.23: Elevation profile of the 2018 April 13, EF-2 Mountainburg, AR tornado

increase in the robustness of subvortices which are generated in the rear quadrant and terminate in the right quadrant, resulting in a southeast movement of enhanced maxW tracks. Subvortices form from enhanced downslope winds stretching vertical vorticity related to radial shears in tangential velocity. Termination in the right quadrant occurs because of the northwest to southeast gradient of terrain height, i.e. once the subvortices begin to traverse downhill (which occurs in the right quadrant), they terminate. During the last third of the ascent segment, the tornado contract and strengthens with maxUV > 70 m s^{-1} on the south side. Once the tornado reaches the ridge segment, the tornado strengthens further with maxUV > 70 m s^{-1} located in all quadrants. Depletion in M may be enough to reduce R but not so much as to reduce tangential velocities, leading to an overall increase in uv. The restrengthening of the tornado on the ridge is different from damage surveys from the Mountainburg, AR case in which the tornado failed to restrengthen after ascent. However, we must be cautious in extending results to an observed supercell case since the boundary conditions in the LES model are forced to remain constant. It is plausible that in an observed case, the initial weakening during the ascent would force modify boundary conditions to the point where the tornado terminates when the ascent is complete. It may be useful to allow variable boundary conditions in the LES model to determine if this would drastically affect results.

For the first 1500 m of the simulation, the tornado at 10 m for V50 and V100 oscillates around $y = 0$ m (Figure 4.24). Then from $x = 1500$ to 2000 m, there is a slight shift northward especially for V50 which reaches $y = 35$ m before a drop south below $y = 0$ m after 2000 m. Beyond $x = 2000$ m, the tornado in both simulations remain below $y = 0$ for the majority of the simulation. This illustrates a preference for the tornado to remain on the
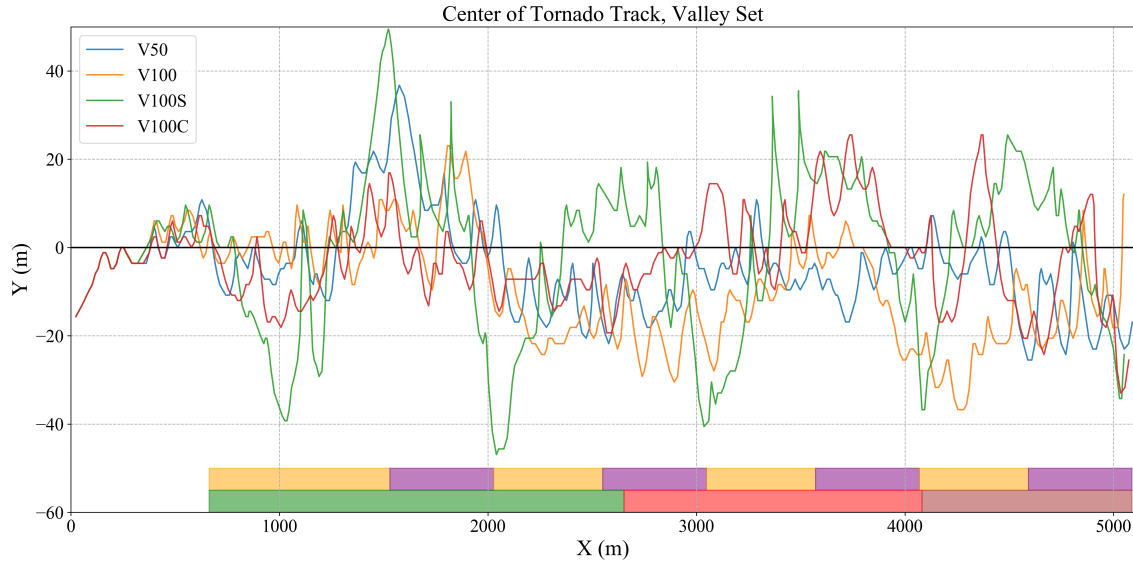
Figure 4.24: Time-series of 10 m center point calculated from averaging pressure deficit fields for the V50, V100, V100S, V100C. The shading at the bottom of the figure represents the segments for V100S and V100C color-coded as in Figure 4.18.

south side of the valley with V100 having more variability in position than V50. There is no distinguishable pattern in the tornado's location in V50C (Figure 4.24, though there is a slight increase in the variability during the ascent and ridge segment past $x = 3000$ m.

In V100S the tornado does in fact tend to follow the valley; during areas when the valley dips the tornado shifts sharply to the south and then lifts back north when the valley curves back. Although the shift of the tornado is not as large as the oscillation of the valley itself (+/- 100 m), there is evidence that the preferred location of the tornado is to follow the valley. On average, the tornado shifts to the south about 40 m and shifts to the north about 20 m. Therefore, even with an oscillating valley, the tornado still attempts to remain on the southern half of the valley, resulting in a larger southern shift.
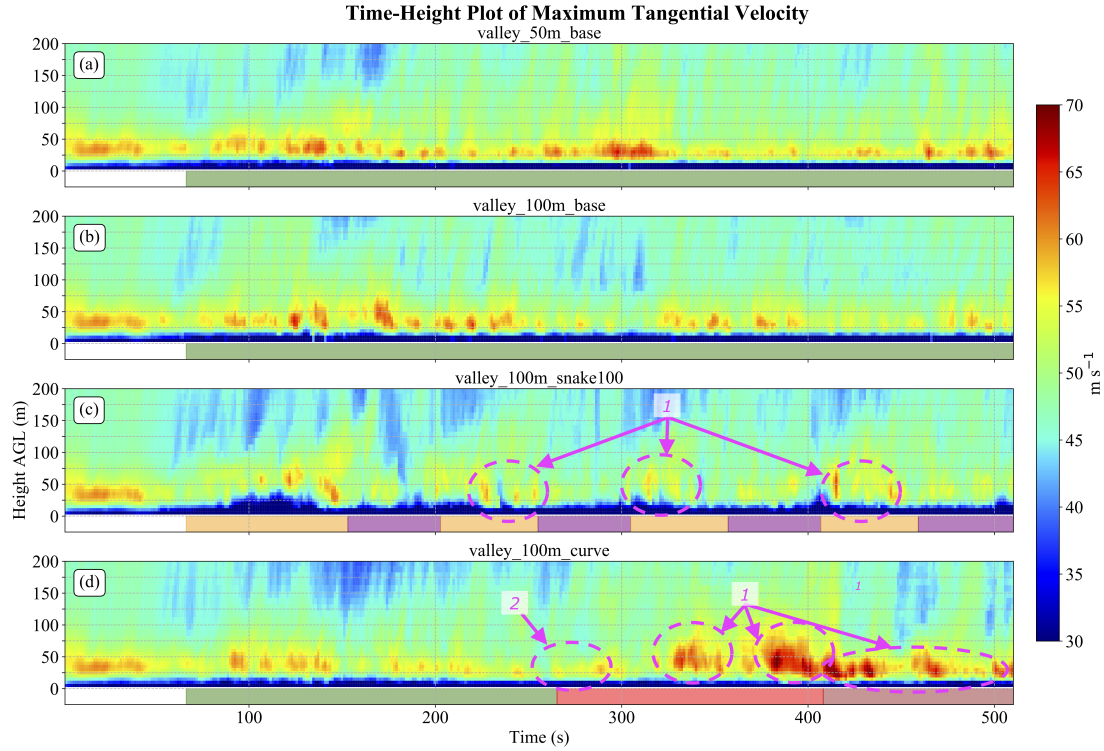
Figure 4.25: Annotated figure of axisymmetric time-height plot of maximum tangential velocity above terrain height for (a) V50, (b) V100, (c) V100S, and (d) V100C. The dotted lines represent the terrain height at the center of the domain for that particular time. Annotations are as follows: 1) stronger v_{max} and 2) weaker v_{max}. Green shading at the bottom of (a) and (b) represent times when the tornado is in the valley while shading in (c) and (d) match with color-coding in Figure 4.18.
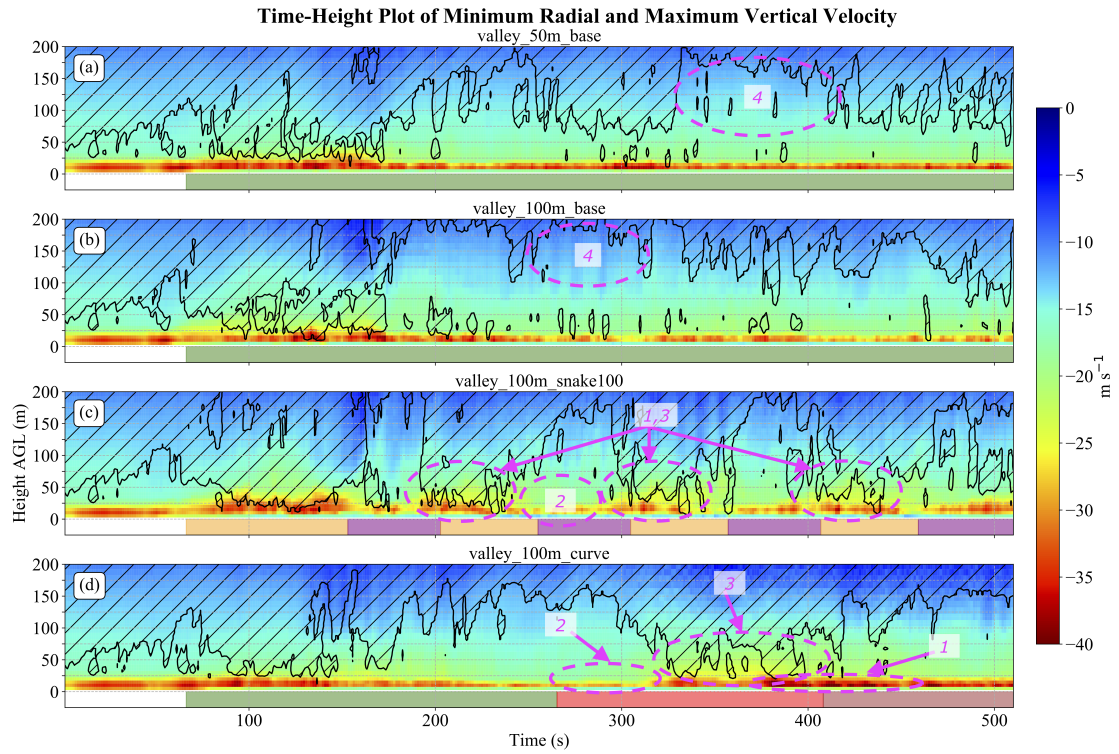
Figure 4.26: Similar to Figure 4.25 except for contoured for minimum radial velocity above terrain height with hatched contour representing maximum axisymmetric vertical velocities $> 20 \, \mathrm{m \, s^{-1}}$. Annotations are as follows: 1) stronger u_{min}, 2) weaker u_{min}, 3) stronger w_{max}, and 4) weaker w_{max}. Shading at the bottom of each figure is the same as Figure 4.25.

4.3.2 Axisymmetric Time-Height Analysis

Patterns of v_{max} between V50 and V100 are fairly similar (Figure 4.25a-b) with localized pulses of stronger v_{max} corresponding to areas of enhanced downslope winds discussed in the previous section. However, v_{max} pulses in V100 are deeper than V50; while most of the v_{max} pulses in V50 extend to about 35 m AGL, the pulses in v_{max} extend to 50 m AGL. There is also a deeper layer of depleted tangential velocities in V100 in the layer closest to the surface. Differences in u_{min} and w_{max} between V50 and V100 are more apparent (Figure 4.26a-b). For both V50 and V100, there is a large increase in w_{max} through the entire column as the tornado enters the valley, collocated with an increase in v_{max}. This initial response could be a result of the entrainment of low-swirl fluid inside of the valley as the tornado enters. After the initial response, there is an overall decrease of w_{max} especially in the intermediate layer between 50 and 150 m; the weakening of w_{max} is more significant in V100. Additionally, u_{min} is weaker in V100 as the inflow has a more difficult time penetrating into the deeper valley.

There is also an initial response of the tornado in V100C to the valley at around 100-150 s. There is an enhancement in v_{max} coincident with an increase in Z_{max} up to 75 m AGL (Figure 4.25), evidence that the tornado initially pulls low swirl fluid from inside the valley. From 100-150s there is also a strengthening of u_{min} and $w_{max} < 50$ m AGL (Figure 4.26). Beyond the initial response, there is an increase in all three axisymmetric variables during the C+ segment, where a drastic decrease in core radius as well as an increase in the vertical velocities was noted in the 10-m track analysis. During C- segments of the valley,

the contour of $w_{max} > 20$ m s^{-1} is not found < 150 m while in the C+ areas, $w_{max} > 20$ m s^{-1} descends to < 50 m AGL.

For V100C, as the tornado begins the ascent, there is a decrease in v_{max} which is collocated with weak and shallow u_{min} and weak w_{max}; the $u_{min} > 30$ m s^{-1} is limited to the lowest 10 m and $w_{max} > 20$ m s^{-1} lifts to 125 m AGL. This continues until the last fourth of the ascent segment when the tornado begins to restrengthen. There is a deep layer of v_{max} > 60 m s^{-1} between 25 and 75 m AGL collocated with $w_{max} > 20$ m s^{-1} extending down to 25 m AGL and u_{min} increasing to > 30 m s^{-1} up to 25 m AGL. During the ridge segment, the layer of strong $v_{max} > 60$ m s^{-1} and $w_{max} > 20$ m s^{-1} remains until about 410 s. After 410 s tornado begins to settle on the top of the ridge and the depth of $v_{max} > 60$ m s^{-1} contracts and is limited to 25-50 m AGL. Additionally, the area of $w_{max} > 20$ m s^{-1} lifts to 150 m AGL. Magnitudes of u_{min} also decrease with areas of $u_{min} > 40$ m s^{-1} occurring less frequently. Nevertheless, the strength of v_{max}, u_{min}, and w_{max} after 410 s remains higher compared to when the tornado was in the valley segment.

Chapter 5

Generalizations

5.1 Tangential Velocity Profile

While the previous chapter contained detailed analysis on specific simulations, this chapter will focus on higher-level analysis. The goal of this chapter is to answer generalized questions about the effects of terrain on tornado structure and dynamics such as how the profile of tangential velocity as a function of height ($v(z)$) and range ($v(r)$) is affected by terrain slope and type, which terrain type has the highest horizontal and vertical winds speeds, etc. To investigate these generalizations, the data have been grouped by terrain category as well as by position over terrain (e.g., uphill, downhill).

The first question that this chapter seeks to address is whether the height of the maximum in $v(z)$ (Z_{max}) or radius of the maximum in $v(r)$ (R_{max}) is a function of terrain. For each simulation, the maximum tangential velocity for every height bin is recorded for each time. The 95th percentile of tangential velocity for all of the times is calculated for each height bin to create a profile of tangential velocity with height, $v(z)$. This process is repeated for range bins to create a profile of the 95th percentile of tangential velocity with range, $v(r)$. The results for the hill set are shown in Figure 5.1 and the sinusoid set in Figure 5.2. Note that the stair-step pattern in the graphs for Z > 75 m AGL for the height profile and for R < 50 m is due to the decreased resolution to 10 m bins in these areas.
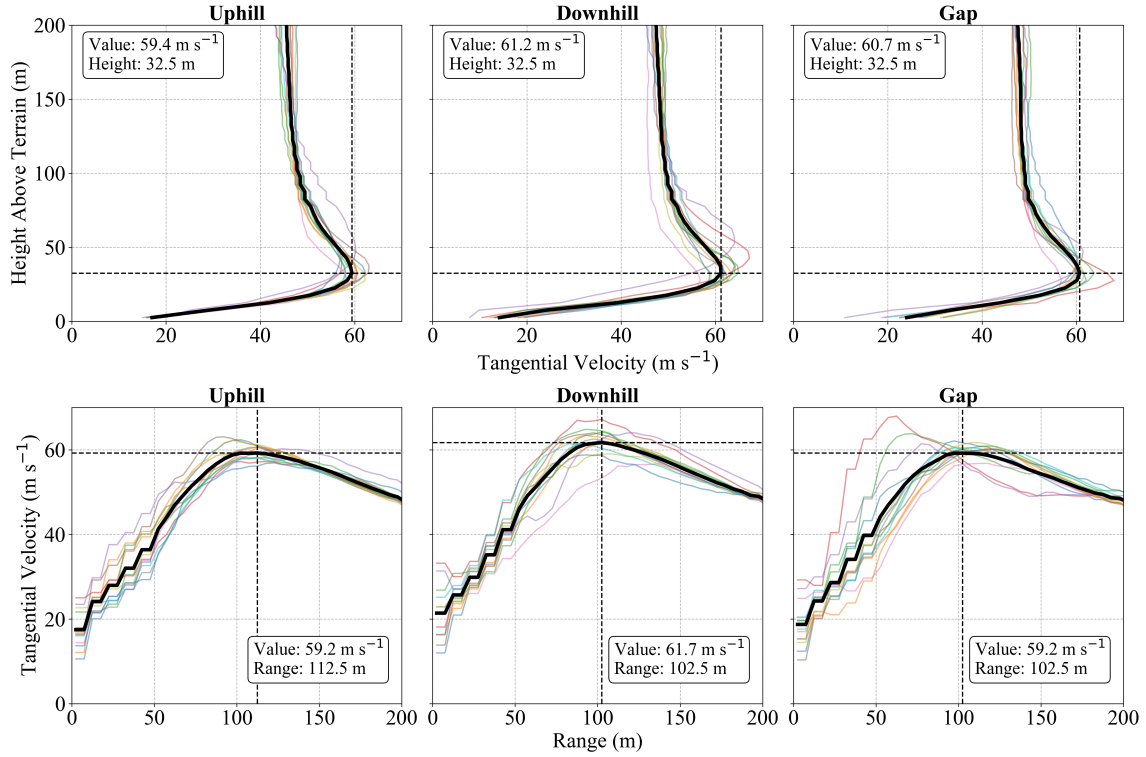
Figure 5.1: The 95th percentile of the tangential velocity profile with height (top row) and range (bottom row) segmented by uphill (left column), downhill (center column) and gap (right column) for all of the 3D hill simulations. The thin colored lines represent each individual simulation while the thick black line is the average of the simulations. The maximum value of the average tangential velocity profile along with the height / range at which this maximum occurs is annotated in each subfigure.
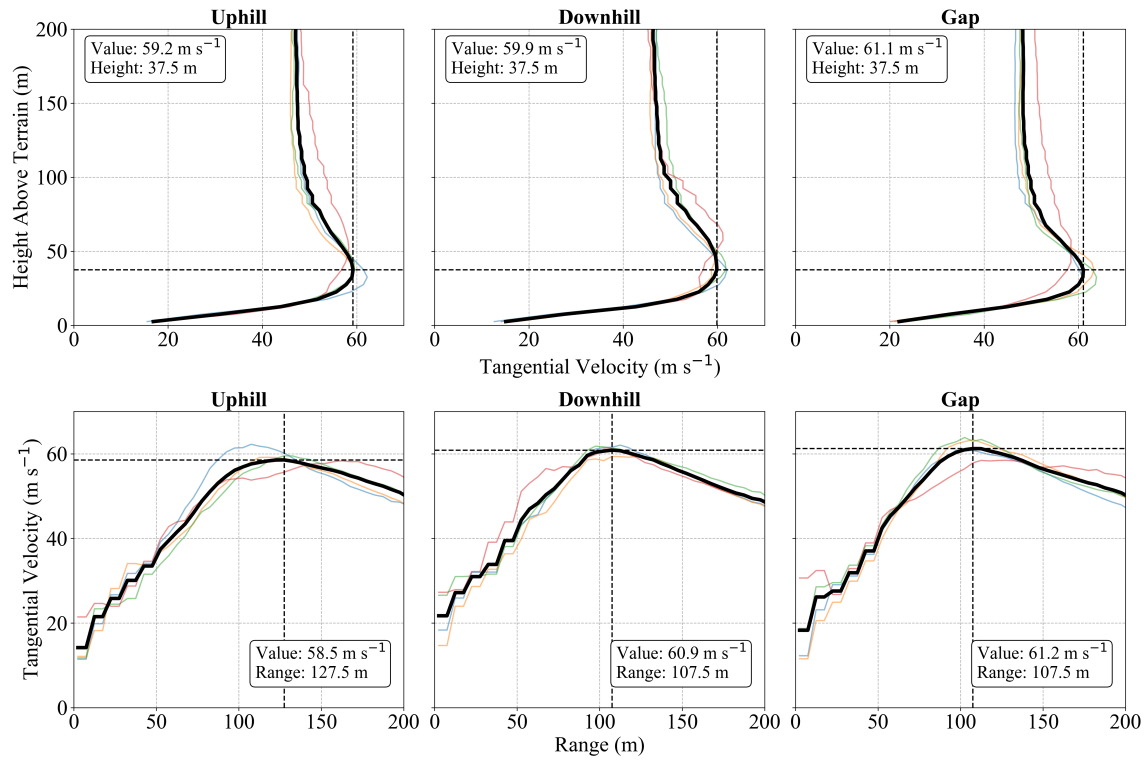
Figure 5.2: Similar to Figure 5.1 except for the 2D / sinusoid hill simulations.

From Figure 5.1, Z_{max} is not a function of terrain and is between 30 - 35 m AGL for all segments. The difference in the maximum of $v(z)$ is not large, $0.5 \, \mathrm{m \, s^{-1}}$ between the down-hill and gap segments. Regardless, the profile between hill simulations on the downhill has the greatest variance while the uphill has the least variance, likely since the downhill is when the lower vortex is disrupted to a greater extent. On the downhill, there are simula-tions whose Z_{max} differs notably from the average profile. Specifically, hill_150m_base has a Z_{max} between 40 - 45 m and hill_200m_base has a Z_{max} between 50 - 55 m. This supports the hypothesis from sinusoid axisymmetric time-height plots (Figure 4.16) that increased terrain height leads to an elevated CFR.

The second row of Figure 5.1 alludes to the contraction (expansion) of the tornado that occurs with respect to the terrain. The tornado is the widest on the uphill with a Z_{max} between 110 - 115 m and contracts on the downhill and gap segment with a Z_{max} of 100-105 m, i.e. the tornado contracts 10 m as the tornado transitions from one side of the hill to the other. The gap segment is the most variable and there are three simulations in the gap segment whose R_{max} differs greatly from the average. While the average R_{max} for the gap segment is 100 - 105 m, R_{max} for hill_200m_base, hill_100m_base, and hill_150m_base is 75 - 80 m, 70 - 75 m, and 60 - 65 m, respectively. It can be concluded that larger hill heights lead to a more contracted tornado in the gap segment.

The same analysis is performed for the sinusoid set (Figure 5.2) and the overall pattern is very similar to that found in the hill set. The profile of $v(z)$ shows that Z_{max} does not change by segment, though in this case there is a larger increase of the maximum of $v(z)$ in the gap segment compared to the downhill segment ($61.1 \, \mathrm{m \, s^{-1}}$ in the gap compared to $59.9 \, \mathrm{m \, s^{-1}}$ on the downhill). Additionally, the Z_{max} is between 35 - 40 m in the sinusoid

case, one bin (5 m) higher than the hill cases, evidence that increased areal extent of terrain while keeping maximum terrain height constant will lead to an increase in Z_{max}. Profiles of $v(r)$ show a contraction of the R_{max} from 125 - 130 m on the uphill segment to 105 - 110 m on the downhill and gap segments. Though contraction (expansion) patterns are the similar, the actual values of R_{max} allude to a couple of things. First, the tornado on average is wider in the sinusoid cases than in the hill cases for a particular segmentation. This is especially obvious on the uphill, where R_{max} for the sinusoid set is 125 - 130 m compared to 110 - 115 m in the hill set. Secondly, the magnitude of contraction from uphill to downhill is larger in the sinusoid cases; the tornado contracts about 20 m in the sinusoid set compared to 10 m in the hill set.

5.2   Inter-comparisons

Tables 5.1 and 5.2 show the 90th, 95th, and 99th percentiles of horizontal wind speed (uv) and vertical velocity (w) for each terrain set at 10 m AGL. The stretched grid for all simulations is interpolated to a regular 2×2 m grid so that each grid point gets equal representation for calculations. The nth percentile for each simulation is calculated from values from all grid points at 10 m AGL with R $<$ 250 m. The average n^{th} percentile from all simulations within a specific terrain set is recorded as the "overall" n^{th} percentile in Tables 5.1 and 5.2. The hill and sinusoid sets are also segmented by uphill, downhill, and gap similar to previous analyses.

Looking at the percentiles of uv for the different terrain sets (Table 5.1), the valley set has the largest uv through the 90th, 95th and 99th percentiles. This is followed by

Table 5.1: Values for the 90th, 95th, and 99th percentile of horizontal wind speeds, *uv*, (10 m AGL and R $<$ 250) for the entire simulation for each of the terrain types. The hill and sinusoid simulations are also segmented by uphill, downhill, and gap.

90th percentile of uv (m s^{-1})

Terrain	Uphill	Downhill	Gap	Overall
Hill	50.2	49.0	51.8	50.8
Sinusoid	53.7	52.1	54.9	53.4
Ridge	-	-	-	52.3
Valley	-	-	-	54.1

95th percentile of uv (m s^{-1})

Terrain	Uphill	Downhill	Gap	Overall
Hill	53.3	52.0	55.9	54.1
Sinusoid	56.9	55.6	59.4	56.8
Ridge	-	-	-	55.4
Valley	-	-	-	57.7

99th percentile of uv (m s^{-1})

Terrain	Uphill	Downhill	Gap	Overall
Hill	59.4	57.1	63.4	60.5
Sinusoid	62.4	61.6	67.7	63.7
Ridge	-	-	-	61.5
Valley	-	-	-	64.6

Table 5.2: Similar to Table 5.1 except for vertical velocity, w.

90th percentile of w (m s^{-1})

Terrain	Uphill	Downhill	Gap	Overall
Hill	11.4	9.5	7.5	9.9
Sinusoid	9.5	8.1	8.1	8.9
Ridge	-	-	-	10.7
Valley	-	-	-	8.3

95th percentile of w (m s^{-1})

Terrain	Uphill	Downhill	Gap	Overall
Hill	14.4	11.9	10.3	12.6
Sinusoid	12.5	10.7	11.3	11.7
Ridge	-	-	-	13.3
Valley	-	-	-	10.9

99th percentile of w (m s^{-1})

Terrain	Uphill	Downhill	Gap	Overall
Hill	21.6	17.2	16.2	18.9
Sinusoid	19.0	15.8	17.7	17.7
Ridge	-	-	-	19.3
Valley	-	-	-	16.6

the sinusoid set, then the ridge set, and lastly the hill set. Studying the hill and sinusoid sets specifically, the sinusoid set has a larger uv overall than the hill set in all three of the segmentations; uphill, downhill, and gap. The difference between uv percentile calculations between the hill and sinusoid sets is around 3 - 4 $\mathrm{m\,s^{-1}}$ for the 95th percentile. Therefore, although the sinusoid set led to a larger disruption in R_{max} and Z_{max}, overall horizontal wind speeds are still stronger in the sinusoid set. Comparing the three segmentations, the gap segment had the strongest horizontal wind speeds while the downhill had the weakest. This is especially apparent in extreme uv (99th percentile) where gap is 4 $\mathrm{m\,s^{-1}}$ stronger than the uphill segment in the hill set and $> 5\,\mathrm{m\,s^{-1}}$ stronger in the sinusoid simulations.

Table 5.2 has the same analysis for all terrain sets except for vertical velocity, w. The ridge has the largest positive w compared to other terrain sets through all three percentile calculations. The ridge is followed by the hill set, then the sinusoid set and lastly the valley set. Weak w for the valley set was already alluded to in 10-m w track analyses (Figure 4.20) with an overall lack of strong w compared to the hill or sinusoid set. Because the tornado roughly follows the valley, flow coming in from all sides of the tornado would be subject to downslope terrain, thus suppressing upward motion. On the other hand, the tornado following the ridge would consist of upslope flow coming in from all sides, enhancing upward motion. Thus, it makes sense that the ridge set show the highest vertical velocities. The hill and sinusoid cases are a middle ground between the two where the tornado brings in air from both upslope and downslope flow depending on the location of the tornado relative to the terrain. However, the hill brings upslope flow to a localized point which would enhance convergence, leading to higher w for the hill compared to the sinusoid cases. The gap is the only segment where w in the sinusoid case is greater than the hill

case, perhaps indicative of more turbulence in the sinusoid. Looking at w by segmentation, the uphill segment for both hill and sinusoid sets have the largest w. On the uphill segment, the direction of translation and the slope of the hill work together to maximize w. While on the downhill the direction of translation and slope of the hill work against each other, there is still forced upslope flow in the left quadrant. This leads to the downhill segment having the second-largest w for the hill set. In the sinusoid set, the gap segment has larger w than the downhill, possible evidence of increased turbulence compared to the hill set.

5.3 Horizontal Velocity

The following analysis focuses on results from specific simulations within the hill and sinusoid sets to analyze how slight modifications in the terrain lead to changes in uv, w, and TKE. For these analysis, the simulations that are not shown in the tables are hill_200m_base, hill_50m_v5, hill_50m_steep1, hill_100m_spread, hill_50m_offset100, and hill_50m_offset200. These simulations are not presented because they either do not show notable differences or there is a simulation that already highlights similar results. Table 5.3 shows the 95th and 99th percentile of horizontal wind speeds, still segmented by uphill, downhill, and gap. The 95th percentile is a good representation of stronger winds found in the tornado while the 99th percentile represents the most extreme winds.

From Table 5.3, the strongest winds for all simulations presented occur in the gap segment with the exception of hill_25m_base and hill_50m_v20. In hill_25m_base, the gap segment is not deep or narrow enough for significant channeling of the winds to take place; in fact, there is very little difference between the uphill, downhill, and gap segments (less

Table 5.3: Values for the 95th and 99th percentile of horizontal wind speeds (10 m AGL and R < 250) for some specific simulations from the hill and sinusoid categories segmented by uphill, downhill, and gap. The maximum value out of the three segmentations are bolded.

95th percentile of uv (m s^{-1})

Simulation	Uphill	Downhill	Gap	Overall
CONTROL	-	-	-	55.5
hill_25m_base	**56.1**	55.4	55.5	55.7
hill_50m_base	54.3	54.7	**55.9**	54.8
hill_100m_base	51.9	53.0	**57.3**	53.2
hill_150m_base	51.0	49.1	**57.3**	51.2
hill_50m_v20	**57.8**	53.6	56.3	56.0
hill_50m_steep2	55.5	52.6	**56.5**	55.4
hill_50m_spread	54.0	53.6	**55.4**	54.8
sinusoid_25m_base	56.2	54.0	**58.5**	56.7
sinusoid_50m_base	56.7	56.3	**60.9**	57.6
sinusoid_100m_base	58.0	55.2	**61.1**	57.5

99th percentile of uv (m s^{-1})

Simulation	Uphill	Downhill	Gap	Overall
CONTROL	-	-	-	60.0
hill_25m_base	**61.7**	60.9	61.3	61.4
hill_50m_base	59.5	59.7	**62.7**	60.5
hill_100m_base	57.9	57.8	**66.4**	60.0
hill_150m_base	57.9	54.5	**66.3**	58.9
hill_50m_v20	**65.4**	58.6	63.8	63.4
hill_50m_steep2	60.8	57.1	**64.2**	62.2
hill_50m_spread	59.5	58.3	**61.6**	60.7
sinusoid_25m_base	61.6	59.3	**65.3**	63.0
sinusoid_50m_base	62.4	63.4	**71.2**	65.6
sinusoid_100m_base	63.9	61.6	**71.0**	65.0

than $1\,\mathrm{m\,s^{-1}}$), leading to the conclusion that the terrain in hill_25m_base is not large enough to cause major differences in *uv* strength with respect to terrain. In hill_50m_v20, the speed of the tornado causes forced mass convergence when the tornado ascends the slope, leading to faster flow and larger *uv*. Additionally, flow channeling is decreased as a result of reduced residence time in the gap segment. Both phenomena were noted in the 10-m track analysis in Figure 4.3. In nearly all simulations, the downhill is the weakest segment in terms of *uv*.

Studying effects of increased terrain height on *uv*, as the hill height increases from 25 m to 150 m for the hill set, there are a couple of patterns to note. Firstly, *uv* on the uphill and downhill segments weaken with increasing terrain height while *uv* in the gap segment increases with terrain height until the hill height reaches 100 m. In other words, for increasing terrain height, the tornado becomes more intense in the gap segment and less intense on uphill and downhill slopes. However when increasing hill height further to 150 m, there are two things that occur: 1) *uv* on the downhill drops significantly and 2) *uv* in the gap no longer increases and plateaus. Further increase in hill height to 200 m (not shown) leads to a decrease of *uv* in the gap segment. This pattern is also evident in the sinusoid set; when increasing terrain height from 25 to 50 m, there is an increase of *uv* in the gap segment. Increasing terrain height from 50 m to 100 m corresponds to a drop in *uv* on the downhill and a plateau of *uv* in the gap. This paints a conceptual picture that while flow channeling from terrain or other mechanisms can enhance tornado intensity, there is a critical height for which the terrain can become disruptive through enhanced friction, leading to a greater displacement from the "mesocyclone". Because of enhanced spatial extent of the terrain in the sinusoid set compared to hill set, this critical point occurs at a

lower terrain height for the sinusoid set (somewhere between 50 m and 100 m for sinusoid and between 100 m and 150 m for the hill).

Other variations lead to interesting results in Table 5.3. Firstly, the strongest *uv* in hill_50m_spread still occurs in the gap segment even though flow channeling is reduced since the distance between hills increases by a factor of two. Thus the gap segment has the strongest *uv* even when the hills are not directly adjacent to each other. However, overall *uv* in hill_50m_spread is slightly reduced compare to hill_50m_base. Therefore all else being equal, hills that are closer together do lead to more intense horizontal winds. Lastly, steepening the hill in the x-direction (hill_50m_steep2) amplifies the terrain effects leading to a stronger uphill / gap segment and a weaker downhill segment.

If the 95th percentile of *uv* for the control simulation is compared against the overall column for the simulations in Table 5.3, the control simulation value of 55.5 $\mathrm{m\,s^{-1}}$ falls somewhere in between the other simulations. However, if we compare the 99th percentile value of 60.0 $\mathrm{m\,s^{-1}}$, or compare either percentile value to the gap region in the simulations, it is found that the control simulation is one of the weakest. This is evidence that flow channeling associated with terrain features is leading to an increase in the most extreme wind speeds compared to no terrain.

Table 5.4 shows the percentage among all grid points whose horizontal wind is greater than the thresholds for EF-1 (38.44 $\mathrm{m\,s^{-1}}$) , EF-2 (49.62 $\mathrm{m\,s^{-1}}$), and EF-3 (60.79 $\mathrm{m\,s^{-1}}$) as given by the EF-scale, aiming to directly address the change in risk factor associated with variations in the terrain. The results for area $>$ EF-3 fit close to what was presented in Table 5.3, which is expected since the 95th and 99th percentile represented the strong / extreme winds of the tornado. All simulations had the largest area of EF-3+ winds in the

Table 5.4: Area of winds > EF-1, EF-2, and EF-3 strength represented as a percentage of the area of the domain where R < 250 m for some specific simulations from the hill and sinusoid categories segmented by uphill, downhill, and gap.

% Area of > EF-1

Simulation	Uphill	Downhill	Gap	Overall
CONTROL	-	-	-	66.7
hill_25m_base	52.7	**52.8**	52.2	52.5
hill_50m_base	**54.9**	50.0	48.5	51.6
hill_100m_base	**50.4**	40.3	45.0	45.8
hill_150m_base	**38.1**	27.0	31.6	33.0
hill_50m_v20	**60.6**	57.9	46.0	55.7
hill_50m_steep2	53.7	50.9	**56.1**	54.4
hill_50m_spread	57.8	49.7	**59.3**	57.4
sinusoid_25m_base	60.0	50.9	**64.3**	59.3
sinusoid_50m_base	61.2	52.5	**62.4**	58.8
sinusoid_100m_base	**59.7**	48.0	49.1	53.6

% Area of > EF-2

Simulation	Uphill	Downhill	Gap	Overall
CONTROL	-	-	-	20.1
hill_25m_base	**16.4**	15.8	14.4	15.4
hill_50m_base	14.5	**14.7**	13.1	14.2
hill_100m_base	8.8	10.3	**14.3**	10.4
hill_150m_base	6.6	4.4	**12.2**	6.6
hill_50m_v20	**19.5**	14.0	13.9	16.1
hill_50m_steep2	**16.7**	10.9	16.1	15.1
hill_50m_spread	14.2	12.6	**16.6**	15.3
sinusoid_25m_base	18.2	12.5	**22.0**	18.2
sinusoid_50m_base	19.8	16.0	**21.2**	19.0
sinusoid_100m_base	**21.5**	13.4	18.7	18.1

% Area of > EF-3

Simulation	Uphill	Downhill	Gap	Overall
CONTROL	-	-	-	0.7
hill_25m_base	**1.4**	1.0	1.2	1.2
hill_50m_base	0.7	0.7	**1.7**	0.9
hill_100m_base	0.5	0.3	**2.9**	0.8
hill_150m_base	0.5	0.1	**2.8**	0.7
hill_50m_v20	**2.7**	0.5	2.1	1.8
hill_50m_steep2	1.0	0.3	**2.1**	1.4
hill_50m_spread	0.6	0.4	**1.3**	1.0
sinusoid_25m_base	1.3	0.6	**3.1**	1.8
sinusoid_50m_base	1.6	1.9	**5.1**	2.6
sinusoid_100m_base	2.5	1.2	**5.2**	2.5

gap segment with the exception of hill_25m_base and hill_50m_v20 which has the largest area of EF-3+ on the uphill segment. As terrain height increases, the area of EF-3+ winds in the gap segment increases up to a certain point until it plateaus (still 100 m for the hill and 50 m for the sinusoid). The hill_50m_spread simulation still has the largest area of EF3+ in the gap segment and hill_50m_steep2 looks to have the same results of hill_50m_base, just amplified. Overall, the sinusoid set have a larger area of EF3+ winds on the downhill, uphill, and gap segments for a given maximum terrain height than the hill set.

The area of EF-1+ and EF-2+ winds differs from the results of Table 5.3. For base hill simulations (except hill_25m_base which is nearly constant with terrain), the uphill segment has the largest area of EF-1+ winds, followed by the gap segment and then the downhill. The EF-1+ area on the uphill decreases with increasing terrain height, including a drop from 50.4% to 38.1% when increasing the maximum terrain height from 100 m to 150 m. Therefore for base hill simulations, while the gap segment has the highest risk in terms of EF-3+ winds, from an areal perspective the uphill segment has the highest risk with the largest area of EF-1+ winds. Additionally, while EF-3+ wind risk in the gap increases with terrain height, the areal risk of EF-1+ winds on the uphill decreases with increasing terrain height. For the sinusoid simulations, a different pattern of EF-1+ winds are present. For the 25 m and 50 m sinusoidal hill, the segment with the largest area EF-1+ winds remains in the gap segment, though the difference in percentage between the gap and the uphill is not very large, especially for sinusoid_50m_base. Increasing the terrain height further in sinusoid_100m_base however leads to the most area of EF-1+ winds present on the uphill. The variations of the 50 m hill, namely hill_50m_v20, hill_50m_steep2, and hill_50m_spread also show similar patterns to that of the EF-3+ winds with the maximum area present in

the uphill, gap, and gap segment again, respectively (though latter two do not show much difference between uphill and gap). The downhill segment has the smallest area for most simulations.

For EF-2+ winds, all sinusoid cases as well as hill_50m_v20 and hill_50m_spread show the same pattern as EF-1+ winds. The segment with the maximum area of EF-2+ winds for hill_100m_base and hill_150m_base shifts to the gap segment which matches EF-3+ winds. Meanwhile hill_25m_base still does not show a significant pattern (uphill has the most area but only by 2%) and surprisingly, hill_50m_base also does not show much variation between the segments. This is most likely because the area of EF-2+ winds are a transition between where the overall tornadic winds (EF-1+) are found (uphill) and where the strongest tornadic winds (EF-3+) are located (downhill). For most simulations, the smallest area of EF-2+ winds is still found in the downhill segment, similar to EF-1+ and EF-3+ areas.

This table illustrates that the "highest risk" area changes depending on whether it is defined as the region with the strongest wind speeds or the largest areal extent of tornadic wind speeds. For example for the base hill simulations, the former (latter) definition would mean the highest risk area is found in the gap (uphill) segment. This is demonstrated well when looking at the control simulation. If the former definition is used, the control simulation would be one of the "lowest" risk simulations with an EF-3+ area of only 0.7% while the latter definition would rank the control as the "highest" risk simulations with a EF-1+ area of 66.7%. The high EF-1+ area is due to the vortex being relatively undisturbed at 10 m AGL with a steady area of EF-1+ winds.

106

5.4   Vertical Velocity

Table 5.5 shows the statistics for w for the same simulations within the hill and sinusoid sets. Looking first at the 95th percentile of w segmented by uphill, downhill, and gap segments, all of the simulations have the strongest vertical velocities on the uphill except for sinusoid_25m_base. This makes sense as the uphill has the largest component of upslope flow out of the three segments. As alluded to earlier, the translation component would enhance the upslope wind component on the uphill segment and work against it on the downhill segment. However, the downhill segment still forces upslope flow in the left quadrant, resulting in higher w compared to the gap segment for larger hill heights.

For increasing terrain height for both the hill and sinusoid cases, both the 95th percentile of w as well as the area of $w > 10\,\mathrm{m\,s}^{-1}$ also increases. Although the downhill has weaker w than the uphill segment overall, w on the downhill also increases with terrain height since there is still upslope flow in the left quadrant of the tornado as it descends the hill. The gap segment stays approximately the same in both percentile and areal coverage of w through all simulations in the table, likely because there is minimal influence of terrain on vertical velocities. Additionally, hill_50m_v20 and hill_50m_steep2 show increases in w on the uphill portion with the latter having the larger increase. Both increased steepness and translational velocity increase the component of upslope flow leading to stronger w on the uphill. However, on the downhill a faster translational velocity actually decreases the upslope flow associated with the left quadrant of the tornado, thus w on the downhill is weaker compared to hill_50m_base. The control simulation has a relatively small area of w

Table 5.5: Table showing the 95th percentile of w, percent area of $w > 10 \text{ m s}^{-1}$ and $w < 0 \text{ m s}^{-1}$ for specific simulations from the hill and sinusoid categories.

95th percentile of w

Simulation	Uphill	Downhill	Gap	Overall
hill_25m_base	**11.0**	10.5	10.7	10.8
hill_50m_base	**11.9**	10.5	10.7	11.1
hill_100m_base	**16.1**	13.4	9.8	14.4
hill_150m_base	**20.5**	16.2	10.1	18.0
hill_50m_v20	**13.7**	9.5	9.3	11.3
hill_50m_steep2	**14.7**	11.8	10.6	12.2
hill_50m_spread	**12.2**	10.4	10.3	10.8
sinusoid_25m_base	10.6	9.6	**11.4**	10.7
sinusoid_50m_base	**11.9**	10.4	11.5	11.3
sinusoid_100m_base	**17.0**	12.3	11.1	14.6

% Area of $w > 10 \text{m s}^{-1}$

Simulation	Uphill	Downhill	Gap	Overall
CONTROL	-	-	-	5.1
hill_25m_base	**6.3**	5.6	5.9	5.9
hill_50m_base	**7.8**	5.7	5.8	6.6
hill_100m_base	**22.3**	14.4	4.7	16.2
hill_150m_base	**40.0**	30.4	5.1	31.2
hill_50m_v20	**11.1**	4.3	4.1	6.9
hill_50m_steep2	**13.6**	8.8	5.7	8.5
hill_50m_spread	**8.1**	5.5	5.5	6.2
sinusoid_25m_base	5.8	4.4	**6.9**	5.9
sinusoid_50m_base	**8.2**	5.6	6.8	7.0
sinusoid_100m_base	**23.7**	12.0	6.6	16.3

% Area of $w < 0 \text{ m s}^{-1}$

Simulation	Uphill	Downhill	Gap	Overall
CONTROL	-	-	-	8.3
hill_25m_base	15.9	14.2	**39.4**	24.9
hill_50m_base	15.7	14.4	**46.6**	23.5
hill_100m_base	16.0	15.6	**46.2**	21.4
hill_150m_base	15.2	14.0	**38.6**	18.2
hill_50m_v20	21.0	16.5	**41.9**	25.3
hill_50m_steep2	14.2	13.8	**35.7**	25.2
hill_50m_spread	13.3	11.9	**23.9**	19.3
sinusoid_25m_base	28.4	22.6	**45.3**	33.6
sinusoid_50m_base	27.0	23.7	**45.9**	31.0
sinusoid_100m_base	24.1	19.7	**46.2**	26.6

$> 10 \text{ m s}^{-1}$ since there is no terrain to influence the vertical component of motion, similar to the gap region.

Looking at the bottom table at Figure 5.5, the gap region contains the most area of negative vertical velocities. In many of the simulations, the area of $w < 0 \text{ m s}^{-1}$ in the gap segment is 2-3 times the area found on the uphill or downhill. While the vortex is in the gap segment, flow from the front and rear quadrants are coming down the terrain, and therefore as some downslope component leading to large areas of $w < 0 \text{ m s}^{-1}$. The sinusoid cases have a larger area of negative w on the uphill and downhill compared to the hill simulations (gap segment has comparable numbers). Additionally, hill_50m_v20, hill_50m_steep2, and hill_50m_spread all result in a decrease of $w < 0 \text{ m s}^{-1}$ area in the gap segment. The decrease of $w < 0 \text{ m s}^{-1}$ area in the last two, especially hill_50m_spread, is the result of increased distance between two adjacent hills (less downslope flow in the front and rear quadrants). Lack of terrain also leads the control simulation to have much less area of $w < 0 \text{ m s}^{-1}$ than the presented simulations.

5.5   Turbulent Kinetic Energy

Lastly, Table 5.6 shows the 99th percentile of TKE values which gives a good representation of the most intense regions of turbulence within the tornado. For all simulations, TKE values are largest in the gap segment. The 99th percentile of TKE in the gap segment also increases with increasing terrain height for both hill and sinusoid simulations. Unlike uv calculations which plateaued after a certain hill height (Table 5.3), TKE values continue to increase even for hill_200m_base (not shown). Additionally, for a given maximum terrain

Table 5.6: Similar to Table 5.3 but for the 99th percentile of TKE.

99th percentile of TKE

Simulation	Uphill	Downhill	Gap	Overall
CONTROL	-	-	-	321.7
hill_25m_base	115.4	140.1	**143.8**	132.9
hill_50m_base	115.8	129.2	**154.0**	131.5
hill_100m_base	126.4	118.6	**165.5**	132.0
hill_150m_base	137.1	144.2	**177.0**	147.4
hill_50m_v20	206.3	163.3	**212.6**	194.5
hill_50m_steep2	132.9	123.8	**165.1**	146.5
hill_50m_spread	109.8	125.8	**241.9**	191.0
sinusoid_25m_base	149.7	149.4	**170.4**	157.6
sinusoid_50m_base	171.6	171.9	**220.9**	186.2
sinusoid_100m_base	202.5	207.5	**277.2**	222.9

height, the sinusoid simulations have a much larger value than the hill simulations for all 3 segments, evidence that increased areal extent of terrain and thus a larger influence of friction will lead a more turbulent tornado. Increased translational velocity also leads to significantly higher values of TKE which is consistent with what Lewellen et al. (1997) found for increased translational velocity with no terrain. Interestingly, hill_50m_spread also has a notable increase in the 99th percentile of TKE in the gap segment. This may be related to the ability of subvortices, which have large values of TKE, to maintain themselves during long gap segments with little influence of larger terrain. This is supported by the large 99th percentile TKE value of the control simulations (321.7), which is representative of the quasi-steady subvortices that rarely dissipate in that simulation.

Chapter 6

Conclusions and Recommendations for Future Work

The objective of this study is to examine effects of different types of terrain on tornado structure. To date, numerous observational studies have hypothesized various effects of terrain, however, these studies were unable to examine the physical processes responsible for the proposed effects and were primarily indirect observations of tornado intensity changes (e.g., from damage surveys). In this study, a comprehensive modeling effort is conducted to elucidate the physical processes and variability in tornado dynamics across a spectrum of terrain types. An LES model with high spatiotemporal resolution is utilized to simulate a vortex. Implementation of terrain features within the model is done through the immersed boundary method which relaxes flow at the terrain boundary to zero. Specific simulations for the hill, sinusoid, and valley sets were analyzed to highlight detailed changes and important features within tornado structure. The analysis was presented mostly through 10-m track analysis of uv and w as well as time-height plots showing axisymmetric calculations of radial, tangential, and vertical winds. Inter-comparisons between the different terrain types and generalized conclusions on the impact of uphill, downhill, and gap regions on the vortex were presented through statistical calculations.

The present study confirms that terrain does in fact have an effect on vortex flow. For the hill set, 10-m track analysis reveals that there are two distinct areas of enhanced uv in the 50 m 3D hill (H50), 100 m 3D hill (H100), and the 50 m steeper hill (H50S), one in

the gap segment and one in the uphill. The region of high uv in the gap segment the result of both flow channeling and enhanced downslope winds, separated by a ribbon of weak uv that is entrained from air originating from the maximum terrain height as low M air from the left quadrant turns inward. This ribbon of low uv is a defining feature in all of the hill simulations, including in the 25 m hill (H25) and the sinusoid simulations.

The region of enhanced uv on the uphill segment in H50, H100, and H50S are collocated with areas of strongest w. This area of larger uv and w stems from robust subvortices that form in the rear quadrant, resultant from enhanced downslope winds and convergence in the rear quadrant, leading to the stretching of pre-existing vertical vorticity from radial shears in tangential velocity. The majority of these subvortices are short-lived; as they traverse uphill, they encounter larger frictional depletion of M causing an inward rotation and displacement from their initial radius where vertical vorticity is highest and the radial shear of tangential and vertical velocity are favorable for subvortex maintenance. Increasing translational velocity to $20 \, \mathrm{m \, s^{-1}}$ in H50V also leads to strong uv and w on the uphill. In this case, however, there is greater mass convergence between the tornado and approaching hill as a result of faster forward motion. Additionally, the disruption of the circulation in the gap segment in H50V is terminate the old circulation, creating a new circulation to the northeast of the old one.

The track of the tornado is also affected by terrain. Overall, there is a northward shift from the end of the downhill to the end of the uphill, followed by a steep southward shift at the beginning of the downhill. The magnitude of the southward shift is greater for larger hill heights, while the steeper hill in H50S results in the southward shift occurring more rapidly. The tornado in H100 remains below y = 0 m for almost the entire simulation.

Because the terrain extends to the southern and northern boundaries in the sinusoid set, flow channeling plays a larger role leading to larger uv in the gap segment. Robust subvortices on the uphill also form in the rear quadrant from stretching of pre-existing vertical vorticity. The low uv ribbon still exists on the downhill and also forms on the uphill from enhanced frictional effects from increased areal extent of terrain. Additionally, the magnitude of disruption of the vortex on the downhill is greater than for the sinusoid set, especially in S100. The downhill segment in S100 results in a significant decrease of the core radius as the areal extent of tornadic winds begins to decrease. The tornado takes on an occluded look from the low uv ribbon and drops very quickly to the south. Eventually the core radius widens as the vortex pulls in higher M air from lower terrain, and a new circulation begins to form to the northeast of the old circulation. In all sinusoid simulations there is a shift to the south from the middle of the uphill to the end of the downhill and a northward shift from the gap segment to the middle of the uphill. The magnitude of the shifts is also dependent on maximum terrain height, similar to the hill set.

Time-height plots of axisymmetric calculations also allude to an increased disruption in the sinusoid set for a given maximum terrain height. While differences v_{max}, u_{min}, and w_{max} between hill and sinusoid sets are not obvious, the height of local maxima in v_{max} is higher in the sinusoid cases, especially obvious when looking at S100 versus H100. While maxima in v_{max} for H100 remain mostly between 25 and 50 m AGL (same as other simulation within the hill set), this height increases up to 75 m AGL for S100 and even $>$ 50 m AGL for S50, increased frictional effects from larger areal extent of terrain lead to a deepening of the corner flow region and a larger layer of low m air near the surface.

For the valley set, V50 and V100 clearly show increased uv and decreased w while in the valley. Regions of stronger uv are resultant from enhanced downslope winds off the side of the valley in the right / front quadrant and flow channeling from lower M air rotating inwards and aligning with the valley axis in the rear quadrant. Additionally, w is weaker in valley simulations as flow coming in from all directions has a downslope component. Enhanced areas of uv in the oscillating valley (V100S) follow the valley axis while larger w is restricted to positively concave (C+) segments of the valley. Further investigations reveal that during C- segments, air being pulled in originates from lower terrain leading to a wider core and weak w while during C+ segments, air being pulled in is forced upslope, reducing M and resulting in a collapse of the core radius and larger magnitudes of w. Lastly, a valley that curves out of the domain (V100C; chosen to emulate the Mountainburg, AR tornado) shows a decrease in both uv and w during the first half of ascent followed by a strengthening during the last third of ascent. Though the initial weakening is consistent with the Mountainburg tornado, the strengthening is not; however, it is possible that variable boundary conditions would be more representative of an observed case leading to different results (i.e., these simulations do not account for a possible weakening at the mesocyclone-scale).

Next, the findings from the composite study are described. Height of maxima in tangential velocity profiles does not change much between the uphill, downhill, and gap segment for either the hill and sinusoid sets. However, the range in the maximum of the tangential velocity profile is a function terrain height / slope. Specifically, the tornado is the widest during the uphill and contracts during the downhill and gap segments. Additionally, the magnitude of contraction is greater for the sinusoid simulations ($\sim$20 m) compared to the hill simulations ($\sim$10 m).

Inter-comparisons between the 4 types of terrain show that the valley has the greatest 10-m horizontal wind speeds overall followed by the sinusoid set, then ridge, then hill. In terms of vertical velocities, the ridge simulations has the highest magnitudes overall followed by the hill set, sinusoid set, and lastly the valley. Again, this is expected since flow from all directions coming into the vortex for the ridge (valley) set has a component upslope (downslope) leading to enhanced upward (downward) motion. For the hill and sinusoid set, the percentiles of *uv* and *w* split by uphill, downhill, and gap segments also affirm that the gap has the fastest *uv* and the uphill has the largest *w* overall.

The strongest 10-m AGL horizontal wind speeds were typically found in the gap regions except hill_25m_base using 95th and 99th percentiles of *uv*. As terrain height increases, *uv* in the gap increases with increasing terrain height up to a certain height (50 m for sinusoid and 100 m for hill) at which point there is a plateau in maximum *uv*. This critical height is likely the result of a balance between increased flow channeling which would act to increase *uv* and a greater disruption of the vortex which acts to decrease *uv*. Other variations also show interesting results. Steepening of the hill amplifies effects seen in hill_50m_base with a stronger uphill and gap segment and a weaker downhill. Increasing the gap segment width by a factor of two in hill_50m_spread decreases *uv*. Nevertheless, the gap segment still has the highest *uv*, illustrating this region still has the most extreme wind winds even with reduced flow channeling.

Tables showing the percentage area greater than EF-1, EF-2, and EF-3 winds give an idea of changes in risk factor with varying terrain. EF-3+ winds follow the same pattern as described above, and were most common in the gap regions. On the other hand, EF-1+ and EF-2+ winds show a different pattern; all of the base hill simulations with a maximum

terrain height ≥ 50 m show the largest area of EF-1+ winds on the uphill, demonstrating that the highest risk area for strongest tornadic winds and overall tornadic winds are not necessarily the same. Overall, the downhill segment is the lowest risk area for nearly all simulations, regardless of EF-rating.

Nearly all simulations have the strongest w on the uphill since the direction of translation of the tornado works in conjunction with the upslope terrain to produce enhanced upward motion. Vertical velocities at 10 m increase with increasing terrain height, even on the downhill since the left quadrant is still subjected to forced upslope flow. Increased steepness of the hill in the x-direction as well as increased translational velocity also lead to stronger w on the uphill since both of those factors increase the upslope component of the flow. The latter, however, does decrease component of upslope flow on the downhill, resulting in lower w on the downhill for hill_50m_v20 compared to hill_50m_base. Values of positive w within the gap segment do not change much from simulation to simulation since terrain effects are the smallest here but contain the largest area of downdraft ($w < 0$ m s^{-1}), possibly because the tornado makes a transition to a two-celled vortex here. Lastly, TKE values are largest in the gap segment for all simulations; increasing terrain height, increased translational velocity, and increased areal extent of terrain (sinusoid vs hill) also result in higher TKE. In general, the terrain is acting to create more variability in tornado dynamics along the track, intertangled with a variety of other factors (e.g., storm-scale influences).

While many different terrain types were presented here, additional simulations with more variations in terrain could be run. Additional terrain features could include buildings to study vortex flow around urban environments. It would also be helpful to implement real terrain features such the surface terrain surrounding the track of the Mountainburg,

AR tornado in order to make more direct comparisons between observed cases and LES results. Allowing for variable boundary conditions, e.g., nesting the boundary conditions from a numerical supercell, would also aid in making the vortex more realistic. It would also allow for thermodynamics to be implicitly defined within the LES.

In terms of the axisymmetric analyses, different center points could be chosen for every model height so that 1) the magnitude of vortex tilt can be analyzed and quantified and 2) axisymmetric calculations are improved especially in times of extreme vortex tilt. It may also be helpful to rerun some of the terrain simulations using a different swirl ratio, e.g., a one-celled vortex, to address whether the magnitude of disruption from surface terrain is a function of vortex size.

The findings of this study could be verified using observations. Recent work using tree fall patterns to examine tornadic flow near the surface, such as in Karstens et al. (2013), could be used to verify some of the key patterns identified in the study such as enhanced horizontal winds from flow channeling through adjacent terrain features, or more robust subvortices when a tornado traverses uphill. If in the correct place at the right time, rapid-scan radars could also measure storm-scale / mesocyclone processes and behavior as the tornado traverses terrain. With further improvement in spatial and temporal resolution, documenting tornado-scale features and even subvortex behavior could be possible through radar observations. Numerically, terrain features could be added in simulations if spatial resolution is high enough. Although terrain features and tornado structure would have to be of much less detail than presented here, it would allow for direct analysis of terrain effects on the supercell which would effect mesocyclone / tornado dynamics.

Bibliography

Agee, E., and E. Jones, 2009: Proposed conceptual taxonomy for proper identification and classification of tornado events. *Wea. Forecasting*, **24**, 609–617.

Bluestein, H. B., and T. M. Crawford, 1997: Mesoscale dynamics of the near-dryline environment: Analysis of data from COPS-91. *Mon. Wea. Rev.*, **121**, 1354–1372.

Bluestein, H. B., W. P. Unruh, D. C. Dowell, T. A. Hutchinson, T. M. Crawford, A. C. Wood, and H. Stein, 1997: Doppler radara analysis of the Northfield, Texas, tornado of 25 May 1994. *Mon. Wea. Rev.*, **125**, 212–230.

Bodine, D. J., T. Maruyama, R. D. Palmer, C. J. Fulton, H. B. Bluestein, and D. C. Lewellen, 2016: Sensitivity of tornado dynamics to soil debris loading. *J. Atmos. Sci.*, **73**, 2783–2801.

Bosart, L. F., A. Seimon, K. D. LaPenta, and M. J. Dickinson, 2006: Supercell tornadogenesis over complex terrain: The Great Barrington, Massachusetts, tornado on 29 May 1995. *Wea. Forecasting*, **21**, 897–922.

Brown, R. A., L. R. Lemon, and D. W. Burgess, 1978: Tornado detection by pulsed doppler radar. *Mon. Wea. Rev.*, **106**, 29–38.

Brown, R. A., and V. T. Wood, 1997: The tornadic vortex signature: An update. *Wea. Forecasting*, **27**, 525–530.

Buban, M. S., C. L. Ziegler, E. N. Rasmussen, and Y. P. Richardson, 2007: The dryline on 22 May 2002 during IHOP: Ground-radar and in situ data analyses of the dryline and boundary layer evolution. *Mon. Wea. Rev.*, **135**, 2473–2505.

Church, C. R., and J. T. Snow, 1993: Laboratory models of tornadoes. *The Tornado: Its Structure, Dynamics, Prediction and Hazards*, No. 79, Amer. Geophys Union, 19–39.

Church, C. R., J. T. Snow, and E. M. Agee, 1977: Tornado vortex simulation at purdue university. *Bull. Amer. Meteor. Soc.*, **58**, 900–909.

Church, C. R., J. T. Snow, G. L. Baker, and E. M. Agee, 1979: Characteristics of tornado-like vortices as a function of swirl ratio: A laboratory investigation. *J. Atmos. Sci.*, **36**, 1755–1776.

Crum, T. D., and R. L. Alberty, 1993: The wsr-88d and the wsr-88d operational support facility. *Bull. Amer. Meteor. Soc.*, **74**, 1669–1688.

Davies-Jones, R., R. J. Trapp, and H. B. Bluestein, 2001: Tornadoes and tornadic storms. *Severe Convective Storms*, C. A. Doswell, Ed., Amer. Meteor. Soc., 167–222.

Davies-Jones, R. P., 1973: The dependence of core radius on swirl ratio in a tornado simulator. *J. Atmos. Sci.*, **30**, 1427–1430.

Davies-Jones, R. P., 1986: Tornado dynamics. *Thunderstorm Morphology and Dynamics*, E. Kessler, Ed., 2nd ed., University of Oklahoma Press, 197–236.

Davies-Jones, R. P., and E. Kessler, 1974: *Weather and Climate Modification*, chap. Tornadoes, 552–595. John Wiley and Sons, New York.

Demoz, B., and Coauthors, 2006: The dryline on 22 May 2002 during IHOP: Convective-scale measurements at the profiling site. *Mon. Wea. Rev.*, **134**, 294–310.

Fiedler, B. H., 1994: The thermodynamic speed limit and its violation in axisymmetric numerical simulations of tornadolike vortices. *Atmos.-Ocean*, **32 (2)**, 335–359.

Fiedler, B. H., 1995: On modelling tornadoes in isolation from the parent storm. *Atmos.-Ocean*, **33**, 501–512.

Fiedler, B. H., 1998: Wind-speed limits in numerically simulated tornadoes with suction vortices. *Quart. J. Roy. Meteor. Soc.*, **124**, 2377–2392.

Fiedler, B. H., and R. Rotunno, 1986: A theory for the maximum windspeeds in tornado-like vortices. *J. Atmos. Sci.*, **43**, 2328–2340.

Fujita, T. T., 1971: Proposed characterization of tornadoes and hurricanes by area and intensity. Tech. rep., University of Chicago, Chicago, IL.

Fujita, T. T., 1989: The Teton-Yellowstone tornado of 21 July 1987. *Mon. Wea. Rev.*, **117**, 1913–1940.

Glickman, T. S., 2000: *Glossary of Meteorology*. Amer. Meteor. Soc., 2nd ed.

Golden, J. H., 1971: A structural comparison between a waterspout active cloud line and non-waterspout cloud line. *7th Conf. Hurricanes and Tropical Meteorology*, Amer. Meteor. Soc., Ed., Barbados, WI.

Golden, J. H., 1973: Some statistical aspects of waterspout formation. *Weatherwise*, **26**, 108–117.

Golden, J. H., 1974a: On the life cycle of Florida Keys' waterspouts, i. *J. Atmos. Sci.*, **31**, 676–692.

Golden, J. H., 1974b: Scale-interaction implications for the waterspout life cycle, ii. *J. Appl. Meteor.*, **13**, 693–709.

Goldstein, D., R. Handler, and L. Sirovich, 1993: Modeling a no-slip flow boundary with an external foce field. *Journal of Computational physics*, **105**, 354–366.

Griffin, C. B., D. J. Bodine, J. M. Kurdzo, A. Mahre, and R. D. Palmer, 2019: High-temporal resolution observations of the 27 May 2015 Canadian, Texas tornado using the Atmospheric Imaging Radar. *Mon. Wea. Rev.*, **147**, 873–891.

Hane, C. E., R. M. Rabin, T. M. Crawford, H. B. Bluestein, and M. E. Baldwin, 2002: A case study of severe storm development along a dryline within a synoptically active environment. part ii: Multiple boundaries and convective initiation. *Mon. Wea. Rev.*, **130**, 900–920.

Houser, J. L., H. B. Bluestein, and J. C. Snyder, 2015: Rapid-scan, polarimetric, doppler radar observations of tornadogenesis and tornado dissipation in a tornadic supercell: The "El Reno, Oklahoma" storm of 24 May 2011. *Mon. Wea. Rev.*, **143**, 2685–2710.

Isom, B., and Coauthors, 2013: The Atmospheric Imaging Radar: Simultaneous volumetric observations using a Phased Array Weather Radar. *J. Atmos. Oceanic Technol.*, **30**, 655 – 675.

Karstens, C. D., W. A. Gallus, B. D. Lee, and C. A. Finley, 2013: Analysis of tornado-induced tree fall using aerial photography from the Joplin, Missouri, and Tuscaloosa-Birmingham, Alabama, tornadoes of 2011. *J. Appl. Meteor. Climatol.*, **52**, 1049–1068.

Kosiba, K., and J. Wurman, 2010: The three-dimensional axisymmetric wind field structure of the Spencer, South Dakota, 1998 tornado. *J. Atmos. Sci.*, **67**, 3074–3083.

Kurdzo, J. M., D. J. Bodine, B. L. Cheong, and R. D. Palmer, 2015: High-temporal resolution polarimetric X-band Doppler radar observations of the 20 May 2013 Moore, Oklahoma tornado. *Mon. Wea. Rev., in press*.

Kurdzo, J. M., and Coauthors, 2017: Observations of severe local storms and tornados with the Atmospheric Imaging Radar. *Bull. Amer. Meteor. Soc.*, **98**, 915–935.

Lee, W.-C., and J. Wurman, 2005: Diagnosed three-dimensional axisymmetric structure of the Mulhall tornado on 3 May 1999. *J. Atmos. Sci.*, **62**, 2373–2393.

Lemon, L. R., and C. A. Doswell, 1979: Severe thunderstorm evolution and mesocyclone structure as related to tornadogenesis. *Mon. Wea. Rev.*, **107**, 1184–1197.

Leverson, V. H., P. C. Sinclair, and J. H. Golden, 1977: Waterspout wind, temperature and pressure structure deduced from aircraft measurements. *Mon. Wea. Rev.*, **105**, 725–733.

Lewellen, D. C., 2012: Effects of topography on tornado dynamics: A simulation study. *26th Conf. on Severe Local Storms*, Amer. Meteor. Soc., Ed., Nashville, TN.

Lewellen, D. C., W. S. Lewellen, and J. Xia, 2000: The influence of a local swirl ratio on tornado intensification near the surface. *J. Atmos. Sci.*, **57**, 527–544.

Lewellen, W. S., 1976: Theoretical models of the tornado vortex. *Proc. Symp. on Tornadoes: Assesment of Knowledge and Implications for Man*, T. T. University, Ed., Lubbock, TX, 107-143.

Lewellen, W. S., C. Church, D. Burgess, C. Doswell, and R. Davies-Jones, 1993: Tornado vortex theory. *The Tornado: Its Structure, Dynamics, Prediction and Hazards*, No. 79, Amer. Geophys Union, 19–39.

Lewellen, W. S., D. C. Lewellen, and R. I. Sykes, 1997: Large-eddy simulation of a tornado's interaction with the surface. *J. Atmos. Sci.*, **54**, 581–605.

Mahre, A., J. M. Kurdzo, D. J. Bodine, C. B. Griffin, R. D. Palmer, and T. Yu, 2018: Analysis of the 16 May 2015 Tipton, Oklahoma EF-3 tornado at high spatiotemporal resolution using the Atmospheric Imaging Radar. *Mon. Wea. Rev.*, **146**, 2103–2124.

Markowski, P., and N. Dotzek, 2011: A numerical study of the effects of orography on supercells. *Atmos. Research*, **100**, 457–478.

Maruyama, T., 2011: Simulation of flying debris using a numerically generated tornado-like vortex. *J. Wind Eng. Ind. Aerodynamics*, **99**, 249–256.

Maxworthy, T., 1982: The laboratory modelling of atmopsheric vortices: A critical review. *Intense atmospheric vortices*, L. Bengtson, and J. Lighthill, Eds., Springer-Verlag, 229–246.

McDonald, J. R., G. S. Forbes, and T. P. Marshall, 2004: The Enhanced Fujita (EF) scale. *22nd Conf. on Severe Local Storms*, Amer. Meteor. Soc., Ed., 3B.2.

Mitchell, E. D., S. V. Vasiloff, G. J. Stumpf, A. Witt, M. D. Eilts, J. T. Johnson, and K. W. Thomas, 1998: he national severe storms laboratory tornado detection algorithm. *Wea. Forecasting*, **13**, 352–366.

Mulen, J. B., and T. Maxworthy, 1977: A laboratory model of dust devil vortices. *Dynamics of Atmospheres and Oceans*, **1**, 181–214.

NOAA National Centers for Environmental Information, 2010: U.S. tornado climatology, https://www.ncdc.noaa.gov/climate-information/extreme-events/us-tornado-climatology. URL `https://www.ncdc.noaa.gov/climate-information/extreme-events/us-tornado-climatology.`

Nolan, D. S., 2005: A new scaling for tornado-like vortices. *J. Atmos. Sci.*, **62**, 2639–2645.

Nolan, D. S., and B. F. Farrell, 1999: The structure and dynamics of tornado-like vortices. *J. Atmos. Sci.*, **56**, 2908–2936.

Pazmany, A. L., J. B. Mead, H. B. Bluestein, J. C. Snyder, and J. B. Houser, 2013: A mobile rapid-scanning X-band polarimetric (RaXPol) Doppler radar system. *J. Atmos. Oceanic Technol.*, **30 (7)**, 1398–1413.

Property Claim Services, 2019: Facts and statistics: U.S. catastrophes.

Rhea, J. O., 1966: A study of thunderstorm formation along dry lines. *J. Appl. Meteorol.*, **5**, 59–63.

Roberts, R. D., and J. W. Wilson, 1995: The genesis of three nonsupercell tornadoes observed with Dual-Doppler radar. *Mon. Wea. Rev.*, **123**, 3408–3436.

Rotunno, R., 1979: A study in tornado-like vortex dynamics. *J. Atmos. Sci.*, **36**, 140–155.

Rotunno, R., 2013: The fluid dynamics of tornadoes. *Annu. Rev. Fluid Mech.*, **45**, 59–84.

Ryzhkov, A. V., T. J. Schuur, D. W. Burgess, and D. S. Zrnić, 2005: Polarimetric tornado detection. *J. Appl. Meteor.*, **44**, 557–570.

Saiki, E. M., and S. Biringen, 1996: Numerical simulation of a cylinder in uniform flow: application of a virtual boundary method. *Journal of computational physics*, **123 (36)**, 450–465.

Schneider, D. G., 2009: The impact of terrain on three cases of tornadogenesis in the Great Tennessee Valley. *Electronic J. Operational Meteor.*, **10**, 1–33.

Simpson, J., G. Roff, B. R. Morton, K. Labas, G. Dietachmayer, M. McCumber, and R. Penc, 1991: A Great Salt Lake waterspout. *Mon. Wea. Rev.*, **119**, 2741–2770.

Smagorinsky, J., 1963: General circulation experiments with the primitive equations I: The basic experiment. *Mon. Wea. Rev.*, **91**, 99–162.

Smith, D. R., 1987: Effect of boundary conditions on numerically simulated vortices. *J. Atmos. Sci.*, **44**, 648–656.

Snow, J., 2019: Tornado. Encyclopædia Britannica, inc., URL https://www.britannica.com/science/tornado.

Snyder, J. C., and H. B. Bluestein, 2014: Some considerations for the use of high-resolution mobile radar data in tornado intensity determination. *Wea. Forecasting*, **29**, 799 – 827.

SPC, 2016: Storm prediction center wcm page. URL https://www.spc.noaa.gov/wcm/.

Stull, R. B., 1988: *An Introduction to Boundary Layer Meteorology*. Kluwer Academic, 666 pp.

Sun, W.-Y., 1987: Mesoscale convection along the dryline. *J. Atmos. Sci.*, **44**, 1394–1403.

Szoke, E. J., M. L. Weisman, J. M. Brown, F. Caracena, and T. W. Schlatter, 1984: A subsynoptic analysis of the Denver tornadoes of 3 June 1981. *Mon. Wea. Rev.*, **112**, 790–808.

Tang, B., M. Vaughan, R. Lazear, K. Corbosiero, L. Bosart, T. Wasula, I. Lee, and K. Lipton, 2016: Topographic and boundary influences on the 22 May 2014 Duanesburg, New York, tornadic supercell. *Wea. Forecasting*, **31**, 107–127.

Torres, S. M., and C. D. Curtis, 2007: Initial implementation of super-resolution data on the NEXRAD network. *Preprints, 23rd Conf. on International Interactive Information and Processing Systems (IIPS) for Meteorology, Oceanography, and Hydrology*, Amer. Meteor. Soc., Ed., San Antonio, TX, 5B.10.

Trapp, R. J., G. J. Stumpf, and K. L. Manross, 2005: A reassessment of the percentage of tornadic mesocyclones. *Wea. Forecasting*, **20**, 680–687.

Uchida, T., and Y. Ohya, 2003: Large-eddy simulation of turbulent airflow over complex terrain. *J. Wind Eng. Ind. Aerodynamics*, **91 (1–2)**, 219–229.

Wakimoto, R. M., N. T. Atkins, and J. Wurman, 2011: The LaGrange tornado during VORTEX2. Part I: Photogrammetric analysis of the tornado combined with single-doppler radar data. *Mon. Wea. Rev.*, **139**, 2233–2258.

Wakimoto, R. M., and J. K. Lew, 1993: Observations of a Florida waterspout during CaPE. *Wea. Forecasting*, **8**, 412–423.

Wakimoto, R. M., and B. E. Martner, 1992: Observations of a Colorado tornado. Part II: Combined photogrammetric and Doppler radar analysis. *Mon. Wea. Rev.*, **120**, 522–543.

Wakimoto, R. M., and H. V. Murphey, 2009: Analysis of a dryline during IHOP: Implications for convection initiation. *Mon. Wea. Rev.*, **137**, 912–936.

Wakimoto, R. M., P. Stauffer, W. C. Lee, N. T. Atkins, and J. Wurman, 2012: Finescale structure of the LaGrange, Wyoming tornado during VORTEX2: GBVTD and photogrammetric analyses. *Mon. Wea. Rev.*, **140**, 3397–3418.

Wakimoto, R. M., and J. W. Wilson, 1989: Non-supercell tornadoes. *Mon. Wea. Rev.*, **117**, 1113–1140.

Ward, N. B., 1972: The exploration of certain features of tornado dynamics using a laboratory model. *J. Atmos. Sci.*, **29**, 1194–1204.

Wilczak, J. M., D. E. Wolfe, R. J. Zamora, B. Stankob, and T. W. Christian, 1992: Observations of a Colorado tornado. Part I: Mesoscale environment and tornadogenesis. *Mon. Wea. Rev.*, **120**, 497–521.

Wilson, J. W., 1986: Tornadogenesis by nonprecipitation induced wind shear lines. *Mon. Wea. Rev.*, **114**, 270–284.

WSEC, 2006: A recommendation for an enhanced Fujita scale (EF-scale). Tech. rep., Wind Science and Engineering Center, Texas Tech University, [Available online at http://www.depts.ttu.edu/weweb/EFScale.pdf].

Wurman, J., D. Dowell, Y. Richardson, P. Markowski, E. Rasmussen, D. Burgess, L. Wicker, and H. B. Bluestein, 2012: The Second Verification of the Origins of Rotation in Tornadoes Experiment: VORTEX2. *Bull. Amer. Meteor. Soc.*, **93**, 1147 – 1170.

Wurman, J., K. Kosiba, and P. Robinson, 2013: In situ, Doppler radar, and video observations of the interior structure of a tornado and the wind-damage relationship. *Bull. Amer. Meteor. Soc.*, **94**, 835–846.

Ziegler, C. L., T. J. Lee, and R. A. Pielke, 1997: Convective initiation at the dryline: A modeling study. *Mon. Wea. Rev.*, **125**, 1001–1026.

Ziegler, C. L., E. N. Rasmussen, T. R. Shepherd, A. I. Watson, and J. M. Straka, 2001: The evolution of low-level rotation in the 29 May 1994 Newcastle–Graham, Texas, storm complex during VORTEX. *Mon. Wea. Rev.*, **129**, 1339–1368.